

ABSTRACT

Convection from Ice Roughness Surfaces Using Scaled Reynolds Numbers for Larger NACA 0012 Airfoils

Zachary Alan Williams, M.S.M.E.

Mentor: Stephen T. McClain, Ph.D.

Ice accretions that develop on aircraft surfaces during flight adversely impact performance by increasing weight and drag, while also decreasing lift and stall margin. Previous studies at Baylor University characterized the convective heat transfer for roughness surfaces exposed to accelerating flow similar to that experienced by a 21-in. NACA 0012 airfoil. The current study characterizes the convective heat transfer using the same roughness surfaces but exposed to flow scaled to that of a larger NACA 0012 airfoil by increasing wind tunnel velocity and thus scaling the Reynolds number. This scaling is appropriate based on previous studies performed in the Icing Research Tunnel (IRT) at the NASA Glenn Research Center that determined relative roughness in the collection region of a 21-in. and a 72-in. NACA 0012 airfoil, with similar collection efficiencies, scales geometrically with airfoil chord. The convective heat transfer coefficients on rough surfaces under scaled Reynolds number conditions were measured.

Convection from Ice Roughness Surfaces Using Scaled Reynolds Numbers
for Larger NACA 0012 Airfoils

by

Zachary Alan Williams, B.S.M.E

A Thesis

Approved by the Department of Mechanical Engineering

Kenneth Van Treuren, Ph.D., Chairperson

Submitted to the Graduate Faculty of
Baylor University in Partial Fulfillment of the
Requirements for the Degree
of
Master of Science in Mechanical Engineering

Approved by the Thesis Committee

Stephen T. McClain, Ph.D., Chairperson

Jill Klentzman, Ph.D.

Randall Jean, Ph.D.

Accepted by the Graduate School

May 2018

J. Larry Lyon, Ph.D., Dean

Copyright © 2018 by Zachary Alan Williams

All rights reserved

TABLE OF CONTENTS

LIST OF FIGURES	vii
LIST OF TABLES	xi
NOMENCLATURE	xii
ACKNOWLEDGMENTS	xvii
DEDICATION	xviii
CHAPTER ONE	1
Introduction.....	1
Motivation.....	1
Objectives	4
Presentation Outline.....	5
CHAPTER TWO	6
Technical Background	6
Fluid Mechanics and Heat Transfer	6
Boundary Layers.....	6
Airfoils	11
Surface Roughness.....	13
Aircraft Icing.....	17
Important Icing Terms	17
Ice Accretion Process.....	21
Ice Accretion Modeling	22

Historical Ice Roughness Investigations	25
Recent Ice Roughness Investigations and Surface Creation.....	29
Smooth Starting Length (SSL) Surface Patterns	29
IRT Surface Patterns.....	30
Real Ice Roughness Surfaces	33
Unwrapping Laser Scan Data	35
Autocorrelation Surface Creation	39
Roughness Scaling.....	42
Reynolds Number Scaling	43
Scaled Ice Roughness Investigation.....	43
CHAPTER THREE	53
Materials and Methodology	53
Roughness Surface Manufacturing.....	53
Instrumented Test Plate.....	55
Plexiglas Sub-Plate	56
Instrumentation and Wiring	56
Mylar Film Heaters.....	57
Aerodynamic Features	58
Ceiling Insert for Flow Acceleration	59
Ceiling Insert Design	59
Ceiling Insert Construction	61
Experimental Setup and Procedure.....	62
Convection Measurements.....	64

Velocity Validation Measurements.....	69
Data Reduction and Uncertainty.....	70
Convection Data Reduction Equation.....	70
Air Properties.....	73
Thermocouple Calibration.....	73
Smooth Surface Heat Transfer Validation.....	74
Uncertainty Analysis.....	74
Probe Calibration and Data Reduction.....	75
CHAPTER FOUR.....	78
Results and Discussion.....	78
Smooth Surface Flow Measurements and Validation.....	78
Convective Heat Transfer Results.....	80
SSL and IRT Surface Results.....	80
Real Ice Convection Results.....	82
Autocorrelation Analog Surface Results.....	86
CHAPTER FIVE.....	95
Conclusions.....	95
Summary of Work.....	95
Future Work.....	97
APPENDIX.....	98
REFERENCES.....	117

LIST OF FIGURES

Figure 1.1	An ice profile prediction created by LEWICE and an experimental ice profile comparison [5].....	3
Figure 2.1:	Viscous boundary layer development over a flat plate (not to scale).....	7
Figure 2.2:	Thermal boundary layer development on a flat plate (not to scale)	9
Figure 2.3:	Airfoil surface pressure distribution	12
Figure 2.4:	Flow separation process on an airfoil surface.....	12
Figure 2.5:	Dirling’s effective sand-grain roughness correlation [26].....	15
Figure 2.6:	Ice accretion on an airfoil stagnation region [41]	22
Figure 2.7:	Modes of energy transfer for an unheated airfoil in icing conditions [42]	23
Figure 2.8	Comparison of measured roughness height with the predicted sand-grain roughness height [45].....	24
Figure 2.9:	Ordered roughness distributions used by Poinsatte et al. [46].....	25
Figure 2.10:	Heat transfer enhancement with varying freestream turbulence [47].....	26
Figure 2.11:	Aluminum cast of if roughness on a NACA 0012 airfoil [48]	27
Figure 2.12:	Solid model of realistic ice roughness surface [51]	28
Figure 2.13:	Heated Section SSL Panels: (a) 052996.04_x10_SSL_Hemispheres, (b) 052996.04_x10_SSL_Cones [53]	30
Figure 2.14	Roughness height measurements in Appendix O conditions [29].....	31
Figure 2.15:	99%-Gaussian RMH values for the 113012.04 Case with the IRT Scaling Function [8].....	32
Figure 2.16:	Heated Section IRT Panels: (a) 113012.04 IRT Hemispheres, (b) 113012.04 IRT Cones [53]	33

Figure 2.17:	Laser Scanned Roughness Data (a) 113012.05, (b) 112912.02, (c) 113012.04, (d) 112912.06 [11]	35
Figure 2.18:	SOM Coordinate System Example [54]	36
Figure 2.19:	Surface Height Distribution of Laser Scanned Ice Roughness [10]	37
Figure 2.20:	(a) Leveled Point Cloud Surface Height Map, (b) Resampled Point Cloud Height Map [10].....	38
Figure 2.21:	Solid models of the real ice roughness surfaces: (a) 113012.05, (b) 112912.02, (c) 113012.04, (d) 112912.06 [11].....	38
Figure 2.22	Peak Roughness Area Analyzed for Surface Characteristics [12].....	39
Figure 2.23:	Autocorrelation comparison of (a) real ice surface and (b) ellipsoid surface, and c) elliptical cone surface [12]	41
Figure 2.24:	Solid models of the heated section of (a) 113012.04 Surface, (b) Ellipsoidal Surface, and (c) Elliptical Cone Surface [12].....	42
Figure 2.25:	Comparison of 041514.01 and 032814.05 point clouds [55].....	45
Figure 2.26:	Measured RMS roughness heights along the surface of airfoils (a) reference conditions with 72-in chord and (b) scaled conditions with 21-in chord [55]	46
Figure 2.27:	Measured ice thickness along the surface of airfoils (a) reference conditions with 72-in chord and (b) scaled conditions with 21-in chord [55]	47
Figure 2.28:	Roughness verses surface distance scaled by airfoil chord grouped by collection efficiency [55]	47
Figure 2.29:	Ice thickness versus surface distance scaled by airfoil chord grouped by collection efficiency [55]	48
Figure 2.30:	Geometric evaluation of local collection efficiency [55]	49
Figure 2.31:	Scaled ice thickness against local collection efficiency (β_s) [55]	50
Figure 2.32:	Scaling parameters used for experimentation	51
Figure 3.1	Unpainted aluminum heated section for 113012.04 Case [10].....	54
Figure 3.2	Full Plastic Manufactured Unwrapped Surface for 113012.04 Case [10].	54

Figure 3.3	Solid Model of the Test Plate [6]	55
Figure 3.4:	Side view of test plate showing thermocouple locations relative to the leading edge (dimensions in inches, flow direction is left to right) [6]	57
Figure 3.5:	Top view of Plexiglas sub-plate showing heated sections (dimensions in inches, flow direction is left to right) [6]	58
Figure 3.6:	Pressure coefficient variation along a low speed NACA 0012 airfoil [8]	60
Figure 3.7:	Scaled airfoil velocity variation and design velocity variation.....	61
Figure 3.8:	Solid model of the ceiling insert [8]	62
Figure 3.9	Side view of experimental setups for (a) the convection tests and (b) velocity boundary layer tests (not to scale) [8].....	63
Figure 3.10	Side view of test section during convective heat transfer testing [8]	64
Figure 3.11	Modified wood cart with equipment used in experimentation [8].....	66
Figure 3.12	Wiring diagram for each heated section [8].....	67
Figure 3.13:	Heated section heat transfer schematic (not to scale) [6]	70
Figure 3.14:	Hot-film probe calibration plot	76
Figure 4.1:	Smooth surface velocity boundary layers	79
Figure 4.2:	Design airfoil velocity variation plotted with measured freestream velocities along a smooth surface	79
Figure 4.3:	Convective heat transfer coefficient contour plot for (a) SSL Plastic Hemisphere, (b) SSL Plastic Cone, and (c) SSL Aluminum Cone.....	83
Figure 4.4:	Convective heat transfer coefficient contour plot for (a) IRT Plastic Hemisphere, (b) IRT Plastic Cone, and (c) IRT Aluminum Cone.....	84
Figure 4.5:	Local Stanton number measurements for (a) SSL Surfaces and (b) IRT Surfaces.....	85
Figure 4.6	Convective heat transfer coefficient contour plot for plastic surfaces (a) 113012.05, (b) 112912.02, (c) 113012.04, (d) 112912.06.....	88

Figure 4.7:	Convective heat transfer coefficient contour plot for aluminum surfaces (a) 113012.05, (b) 112912.02, (c) 113012.04, (d) 112912.06	89
Figure 4.8:	Local Stanton number measurements for (a) plastic and (b) aluminum real ice roughness surface	90
Figure 4.9:	Convective heat transfer coefficient contour plot for plastic surfaces (a) 113012.04, (b) Ellipsoids, (c) Elliptical Cones.....	92
Figure 4.10:	Convective heat transfer coefficient contour plot for aluminum surfaces (a) 113012.04, (b) Ellipsoids, (c) Elliptical Cones	93
Figure 4.11:	Local Stanton number measurements for (a) plastic surfaces (b) aluminum surfaces	94

LIST OF TABLES

Table 2.1:	Comparison of measured Appendix C icing roughness condition and SSL parameters [53]	29
Table 2.2:	Conditions of the Four SLD Studied Surfaces [11]	34
Table 2.3:	Summary of test parameters for roughness scaling parameters [55]	44
Table 3.1:	Conduction parameter values, C_k [7]	73
Table 3.2:	Convective Heat Transfer Coefficient Measurement Uncertainty [8]	75

NOMENCLATURE

A_c	Accumulation parameter
A_t	Total area of heated section
b_n	Winning codebook vector
C_f	Skin friction coefficient
C_k	Conduction parameter for the k^{th} heated section (0.9, 0.9, 1.05, 1.1, 1.05)
c_p	Specific heat of fluid
C_p	Pressure coefficient
E	Voltage across heater
h	Convective heat transfer coefficient
I	Current through heater
J	Number of points on a surface for which b_n is the closest vector
K	Droplet inertial parameter
K_0	Modified inertial parameter
k_f	Thermal conductivity of fluid
k_p	Thermal conductivity of Plexiglas
L	Length scale of Stokes number
m'_w	Mass flux
n	Freezing fraction
N	Sample size
$N_{f,\text{stag}}$	Freezing fraction

$\bar{N}_{0,R}$	Stagnation point fully-dense rime ice stagnation thickness
N_x^j	Orthogonal distance from an ice surface point to the mean ice shape
p	Pressure
Pr	Prandtl number
\dot{Q}_{CONV}	Convected heat
\dot{Q}_{GEN}	Energy supplied
\dot{Q}_{HL}	Heat loss
\dot{Q}_{RAD}	Radiated heat
q_w''	Wall heat flux
Re	Reynolds number
Re_δ	Droplet Reynolds number
R_q	Root-mean-square roughness height (also called RMS)
r_0	Leading edge radius
S	Standard deviation
St	Stanton number
Sk	Stokes Number
T_{BL}	Thermal boundary layer temperature
T_{FSi}	Average freestream temperature over i^{th} surface panel
T_{IR}	Infrared camera temperature reading
T_s	Surface temperature
T_{SS}	Steady state temperature
T_{total}	Total temperature
T_{UP}	Temperature under plate

T_∞	Freestream temperature
t_p	Plexiglas sub-plate thickness
t	Student's t-value
u	Streamwise velocity
U_e	Edge velocity
U_{random}	Random uncertainty
U_∞	Freestream velocity
V	IRT tunnel velocity
V_{eff}	Effective velocity measured by hot-film wire(s)
V_{meas}	Measured velocity by pitot-static probe
V_N	Normal velocity component
V_T	Tangential velocity component
x	Streamwise location on plate
x_{cr}	Critical distance for flow transition
x_k	Sand grain equivalent roughness height
w	Wall-normal velocity
z	Wall-normal distance from plate surface
<i>Greek</i>	
α	Thermal diffusivity OR angle of x-array probe
β_0	Stagnation point collection efficiency
β_s	Local cloud collection efficiency
γ_s	Angle of surface relative to airfoil design flow coordinates
δ	Velocity boundary layer thickness

δ_T	Thermal boundary layer thickness
Δt_s	Exposure time
ε	Emissivity (0.95)
ζ	Dummy variable representing x in Stanton number correlations
κ	Tangential velocity attenuation factor (0.115)
μ	Fluid dynamic viscosity
μ_{air}	Dynamic viscosity of air
ν	Fluid kinematic viscosity
ξ	Unheated starting length (1.7285")
ρ	Fluid density
ρ_{ice}	Ice density at freestream temperature
ρ_w	Droplet density
σ	Stefan-Boltzmann constant (5.67E-8 W/m ² K ⁴)
τ_w	Wall shear stress

Subscripts

TC, cal	Thermocouple temperature measurement during calibration
TC, test	Thermocouple temperature measurement during test
IR, cal	Infrared temperature measurement during calibration

Abbreviations

ARES	Airfoil Roughness Evaluation System
BUSWT	Baylor University Subsonic Wind Tunnel
FAA	Federal Aviation Administration
IRT	Icing Research Tunnel

LEWICE	Lewis Ice Accretion Code
LWC	Liquid water content
MVD	Median volumetric Diameter
NACA	National Advisory Committee of Aeronautics
NASA	National Aeronautics and Space Administration
RMH	Roughness maximum height
RMS	Root-mean-square roughness height
SLD	Supercooled large droplets
SOM	Self-organizing map
VIST	Vertical Icing Studies Tunnel

ACKNOWLEDGMENTS

I offer many thanks to my advisor Dr. Stephen T. McClain for giving countless hours to provide academic knowledge and show professionalism in leadership while also always leaving room for humor and random movie references. I would also like to thank Dr. Randall Jean and Dr. Jill Klentzman for serving on my thesis committee, their time during busy schedules is greatly appreciated.

Next I thank my predecessors in the Baylor Icing Group, Logan Tecson, Chris Walker, Tim Shannon, and Matt Hawkins, without their ground work, this paper would not be possible. I offer my sincerest thanks to Mr. Ashley Orr for offering his time and expertise to create the complex roughness surfaces used for experimentation. To my fellow graduate students, Jaime McCarrell, John-Mark Clemenson, Taber Miyauchi, Nic Mosser, and Berkley Bonjonia, thank you for your help in the classroom, on this project, and most importantly your friendship throughout the graduate program.

I would also like to thank my family and friends for their constant love and support which has gotten me to where I am today. Mom and Dad, thank you for continually instilling the importance of academics and learning in me and, of course, your sacrifices to ensure I was provided everything I needed (and more) to have an outstanding education.

The efforts reported in this work were supported as part of NASA Collaborative Agreement No. NNX16AN32A. Any opinions presented in this work are those of the author and do not reflect the views of NASA or the United States government.

DEDICATION

To my parents, Rich and Kimmy

CHAPTER ONE

Introduction

Motivation

Ice accretions that develop on aircraft surfaces during flight have been proven to adversely impact aerodynamic performance. Ice accretions cause reduced lift and stall margins, while also increasing weight and experienced drag [1]. The degradation of performance can lead to unsafe flight conditions, and thus greatly increase the risk of an accident. Ideally aircraft avoid flying through ice conditions altogether, but with the increase in flight traffic, totally avoiding these conditions is not practical and in some cases impossible. The ability for all aircraft to operate safely in these conditions is therefore necessary.

An aircraft can operate safely by using anti-icing and de-icing techniques. Anti-icing techniques focus on ways prevent or slow down the ice accretions by electric heaters or the use of rerouted warm air from the engine onto the aircraft surface. De-icing removes ice that has already formed on the aircraft surface using methods such as using a glycol spray or knocking off the ice with a pneumatic boot.

In the interest of safe flight through icing conditions, the Federal Aviation Administration (FAA) began implementing design requirements which allow for safe flight with a given amount of in-flight ice accretion. Historically these FAA requirements were based on Appendix C conditions of the U.S. Code of Federal Regulations [2]. However, as ice accretion understanding progressed, the design specifications were

updated in 2014 to include Appendix O conditions [3]. Under these design specifications, the ability for manufacturers to predict aircraft icing on new designs became necessary. Full scale testing on new designs is timely and costly. An alternative to full scale testing is the use of a prediction code that simulates ice accretion on an aircraft surface.

The Lewis Ice Accretion Code (LEWICE), developed at NASA Glenn Research Center, is an ice accretion code distributed to aircraft manufacturers for the design implementation of de-icing systems. As the physics of ice accretions are better understood, LEWICE can be improved. A specific area for LEWICE improvement is the characterization and prediction of the convective enhancement caused by the initial layer of ice roughness [4]. Currently, the LEWICE convection enhancement predictions use sand-grain equivalent roughness, which consists of regular and ordered geometries exposed to constant flow. A real airfoil, however, experiences accelerating flow and real ice roughness has a random distribution of roughness elements with varying heights.

Properly predicting the way ice initially forms in the first few minutes of an icing event is important. If the initial roughness model is inaccurate, the larger ice protrusions at longer exposure times will also be inaccurate. Figure 1.1 compares an ice profile prediction created by LEWICE and an experimental ice profile created in the Icing Research Tunnel (IRT) at NASA Glenn. The results of this particular comparison shows the protrusion, and thus the convective enhancement, is over estimated by LEWICE. It is important to note that this over prediction occurs consistently as the ice shape grows.

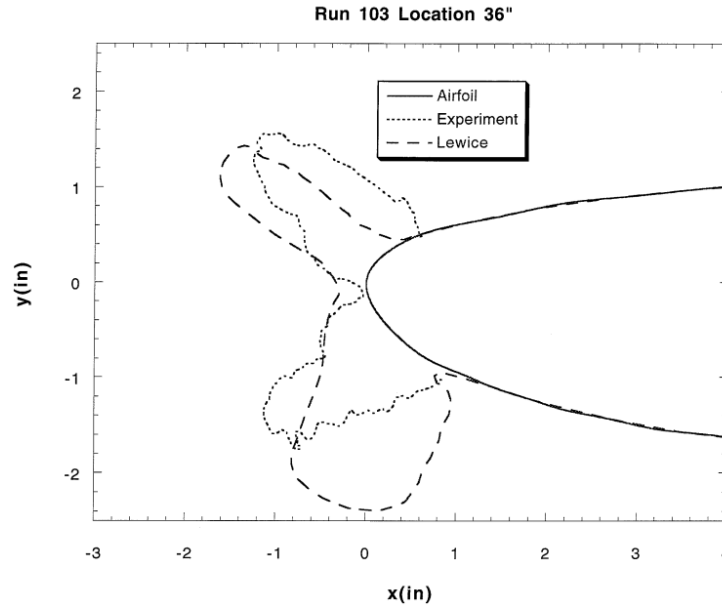


Figure 1.1: An ice profile prediction created by LEWICE and an experimental ice profile comparison [5]

In attempts to improve on the characterization of convective enhancement by LEWICE, many previous studies were performed at Baylor University. Tecson [6] investigated convective enhancement on realistic ice roughness surfaces. Expanding on Tecson [6], Walker [7] imposed varying thermal boundary conditions. The surfaces studied by Tecson [6] and Walker [7], based on the old Appendix C conditions, exhibited an abrupt smooth-to-rough transition and constant roughness properties in the downstream direction. Shannon [8] improved on this work by updating the roughness height variations in the downstream direction to match data from real ice laser scans. Shannon [8] also included an accelerating profile along the test surface to match that of an actual 21-in NACA 0012 airfoil. To investigate roughness in the stagnation region (the leading 2%), Hughes [9] ran heat transfer experiments in the Vertical Icing Studies Tunnel (VIST) at NASA Glenn Research Center. Hawkins [10] then created a real ice roughness surface using laser scan data to compare convective enhancement to the results

of the simulated roughness surface created by Shannon [8]. McCarrell [11] created three more real ice roughness surfaces to add to Hawkins' [10] surface in order to characterize the heat transfer on a progression of four surfaces exposed to increasing exposure times. Clemenson [12] created two new simulated roughness surfaces using autocorrelation analyses to properly match the heat transfer enhancement of the real ice surface studied by Hawkins [10]. All of the previous surfaces were exposed to, created, and tested under flows experienced by a 21-in NACA 0012 airfoil.

Objectives

The objective of this study is to expand on the works of Tecson [6], Walker [7] Shannon [8], Hughes [9], Hawkins [10], McCarrell [11], and Clemenson [12] by characterizing the heat transfer enhancement of real and simulated roughness surfaces experiencing flows similar to those of a 72-in NACA 0012 airfoil. The roughness surfaces from the previous studies are used, but the wind tunnel velocity was increased. Thus, the Reynolds number of the flow over the surface was scaled up from that of a 21-in NACA 0012 airfoil to that of larger NACA 0012 airfoils. The same roughness surfaces can be used because a previous study performed in the IRT at NASA Glenn demonstrated that relative roughness in the collection region of a 21-in and a 72-in NACA 0012 airfoil, with similar accumulation parameters, scales geometrically.

Ultimately this study's objective is to improve on the heat transfer characterization and prediction of LEWICE. With the inclusion of experimental convection measurements on different size airfoils, a better correlation for the prediction of convective enhancement due to ice roughness can be created.

Presentation Outline

Chapter Two provides a technical background of fluid mechanics, heat transfer, airfoils, surface roughness, aircraft icing, unwrapped roughness surface creation, and roughness scaling. Chapter Three outlines the materials and methodology used to perform the experiments in this study and also the data reduction and uncertainty calculations. Chapter Four is a detailed account of the experimental results and discussion. Chapter Five provides the conclusions made based on the results presented and also discusses future work.

CHAPTER TWO

Technical Background

This chapter discusses important background information relative to the current study. A discussion of viscous and thermal boundary layers along with information on airfoils is given. Next is a brief account of historical surface roughness investigations followed by historical aircraft ice roughness experiments. Last, descriptions of recent ice roughness investigations relevant to this study and roughness scaling background are presented.

Fluid Mechanics and Heat Transfer

Boundary Layers

In 1904, a major advancement in the practicality of fluid mechanics engineering was conceived by Ludwig Prandtl. Prandtl created the idea of a velocity, or viscous, boundary layer, which is a thin layer near the surfaces of a submerged object in which viscous effects are of great importance, and outside this layer the flow can be treated as if it were inviscid [13].

Figure 2.1 is an example of a velocity boundary layer developing over a flat plate. The freestream velocity flow field (U_∞) flows across the flat plate and the boundary layer begins to form at the leading edge. The velocity boundary layer thickness (δ_x) grows in the flow direction along the plate and is a function of horizontal distance along the plate (x) and is the vertical distance from the flat plate surface. The region of flow directly

following the leading edge of the flat plate can be considered the laminar region where the flow is uniform as the fluid particles follow in stream lines. As the flow reaches the critical point (x_{cr}), it reaches a transition region in which the flow eventually reaches the turbulent regime where the fluid particles behave in a chaotic nature. Also forming in the turbulent regime is a viscous sublayer very close to the plate where viscous effects dominate the turbulent fluctuations and the flow is essentially laminar. For a particular point along the plate, the velocity profile of the flow inside the boundary layer ($u(z)$) varies with the vertical distance away from the flat plate surface.

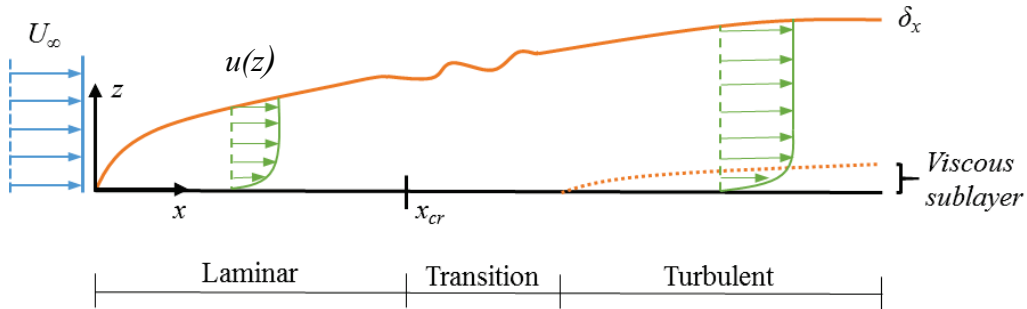


Figure 2.1: Viscous boundary layer development over a flat plate (not to scale)

The velocity of the fluid at the surface of the plate is zero due to the no-slip condition, which states that the friction between the fluid and surface of a body is large enough that the velocities between the surface and the fluid are equal (zero). This interaction between the fluid and surface causes a wall shear stress (τ_w). Eq (2.1) shows the calculation of wall shear stress for a Newtonian fluid which is the product of fluid dynamic viscosity and the velocity gradient at the wall.

$$\tau_w = \mu \left. \frac{\partial u}{\partial z} \right|_{z=0} \quad (2.1)$$

The skin friction coefficient (c_f) is a non-dimensional representation of wall shear stress and can be calculated using Eq. (2.2) where ρ is the density of the fluid and U_∞ is the freestream velocity.

$$c_f = \frac{\tau_w}{1/2 \rho U_\infty^2} \quad (2.2)$$

The skin friction coefficient is significant as it is used to characterize skin friction drag between surfaces under similar flow conditions.

Another non-dimensional parameter that is important when relating flows over different surfaces is the Reynolds number. The Reynolds number is a flow comparison parameter in fluid experiments because flows with similar Reynolds number are expected to behave in similar ways. Using a scaling argument, a Reynolds number can be defined as a geometric ratio, or slenderness ratio, which describes the thickness of the boundary layer related to the length of the flow domain. Given in Eq. (2.3) is the calculation for a Reynolds number for flow over a flat plate where ρ is the fluid density, U_∞ is the freestream velocity, x is the horizontal location along the plate from the leading edge, and μ is the fluid dynamic viscosity.

$$\text{Re}_x = \frac{\rho U_\infty x}{\mu} \quad (2.3)$$

It is important to note that flows with a Reynolds number from 0 to 5×10^5 in standard conditions are generally considered laminar, while flows above are considered turbulent [13].

If there is a temperature difference between a fluid in motion and a surface, similar to the velocity boundary layer, a thermal boundary layer will develop. Figure 2.2 depicts the thermal boundary layer development on a flat plate if the temperature of the

surface (T_s) is greater than the temperature of the moving fluid (T_∞). The temperature difference between the fluid and the plate creates a temperature gradient within the fluid which creates a temperature profile (T) that is a function of the vertical distance (z) from the flat plate surface. The thermal boundary layer thickness (δ_T) is a measured vertical distance from the flat plate surface to the height where the fluid temperature is essentially equal the freestream temperature. The thermal boundary layer thickness is a function of the horizontal downstream distance along the plate (x).

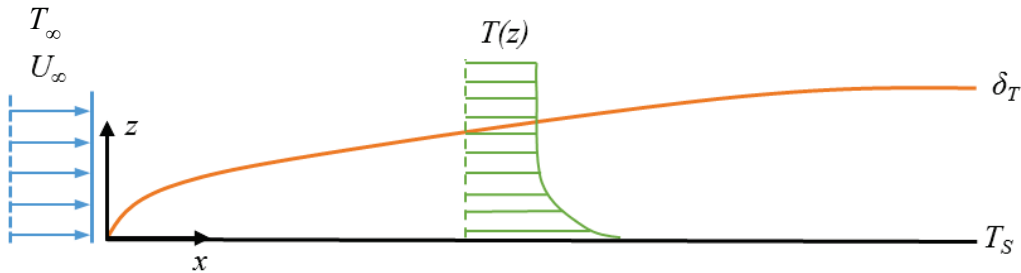


Figure 2.2: Thermal boundary layer development on a flat plate (not to scale)

The Prandtl number is a non-dimensional parameter that is used to relate the viscous and thermal boundary layers. Eq. (2.4) shows the Prandtl number calculation. In this equation c_p is the specific heat of the fluid, k_f is the thermal conductivity of the fluid, ν is the kinematic viscosity of the fluid, and α is the thermal diffusivity of the fluid.

$$Pr = \frac{c_p \mu}{k_f} = \frac{\nu}{\alpha} \quad (2.4)$$

The value of the Prandtl compares the thickness of the viscous and thermal boundary layer thicknesses, and represents the ratio of momentum diffusivity to thermal diffusivity. A calculation of the Prandtl number much greater than one ($Pr \gg 1$) means the viscous boundary layer thickness is larger than the thermal boundary layer. A Prandtl

number much less than one ($Pr \ll 1$) means the thermal boundary layer thickness is larger than the viscous boundary layer [14].

Analogous to the wall shear stress experienced due to viscous forces in the velocity boundary layer, the temperature gradient in the thermal boundary layer causes a heat flux between the moving fluid and the surface. Eq (2.5) defines the surface heat flux as the product of the fluid thermal conductivity and temperature gradient at the surface.

$$q_w'' = -k_f \left. \frac{\partial T}{\partial z} \right|_{z=0} \quad (2.5)$$

The surface heat flux is converted to a non-dimensional Stanton number for comparison between multiple experiments with differing fluid properties and flow conditions. The local Stanton number is represented in Eq. (2.6) where h is the convective heat transfer coefficient at a given location x .

$$St_x = \frac{q_w''}{\rho U_\infty c_p (T_s - T_\infty)} = \frac{h}{\rho U_\infty c_p} \quad (2.6)$$

Just as the wall shear stress and wall heat flux are analogous, so are the Stanton number and skin friction coefficient on smooth flat plates.

Eq. (2.7) and (2.8) are theoretical Stanton number correlations for laminar and turbulent flow over a smooth flat plate with a constant heat flux boundary condition. The correlations include corrections for an unheated starting length (ξ) [15].

$$St_{x,\text{laminar}} = \left[1 - (\xi/x)^{3/4} \right]^{-1/3} 0.453 Re_x^{-1/2} Pr^{-2/3} \quad (2.7)$$

$$St_{x,\text{turbulent}} = \left[1 - (\xi/x)^{9/10} \right]^{-1/9} 0.0308 Re_x^{-1/5} Pr^{-2/3} \quad (2.8)$$

Although these correlations provide insight into how the Stanton number varies on a smooth flat plate, they fall short for flows in a freestream acceleration. Shannon [9]

presented new correlations using the correction of Smith and Spalding [16] and correction of Ambrok [17] for laminar and turbulent flows, respectively. These updated theoretical Stanton number correlations are shown in Eq. (2.9) and (2.10).

$$St_{x,\text{laminar},x_{\text{cel}}} = \left[1 - (\xi/x)^{3/4} \right]^{-1/3} \frac{0.453 Re_x^{-1/2} Pr^{-2/3}}{\left[\int_0^\xi \left(\frac{U_e(\zeta)}{U_e(x)} \right)^{(2.95 Pr^{0.07})-1} \frac{d\zeta}{x} \right]^{\frac{1}{2}}} \quad (2.9)$$

$$St_{x,\text{turbulent},x_{\text{cel}}} = \left[1 - (\xi/x)^{9/10} \right]^{-1/9} \frac{0.0308 Re_x^{-1/5} Pr^{-2/3}}{\left[\int_0^\xi \left(\frac{U_e(\zeta)}{U_e(x)} \right) \frac{d\zeta}{x} \right]^{\frac{1}{5}}} \quad (2.10)$$

Airfoils

The primary purpose of an airfoil is to accelerate the flow around its top surface which, according to Bernoulli's equation, causes a decrease in pressure and the creation of lift. This area where the pressure decreases in the flow direction is known as the favorable pressure gradient. The pressure gradient will eventually reach a minimum and begin to increase in the region labeled the adverse pressure gradient. Figure 2.3 illustrates an example of a surface pressure distribution on an airfoil in which the favorable and adverse pressure gradient regions are labeled. Under certain conditions, the flow over an airfoil can separate in the adverse pressure gradient region. At the point of separation, the boundary layer lifts off the surface and a wake region forms in which the flow begins to reverse direction and greatly increases the pressure drag. Shown in Figure 2.4 is flow separating from an airfoil surface where the pressure gradient at the airfoil reaches zero.

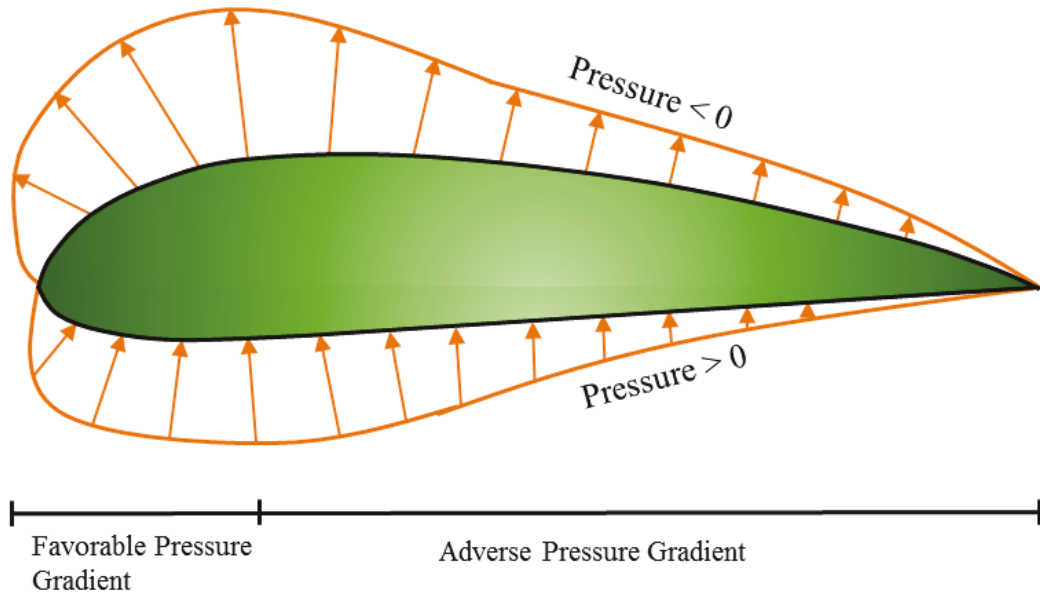


Figure 2.3: Airfoil surface pressure distribution

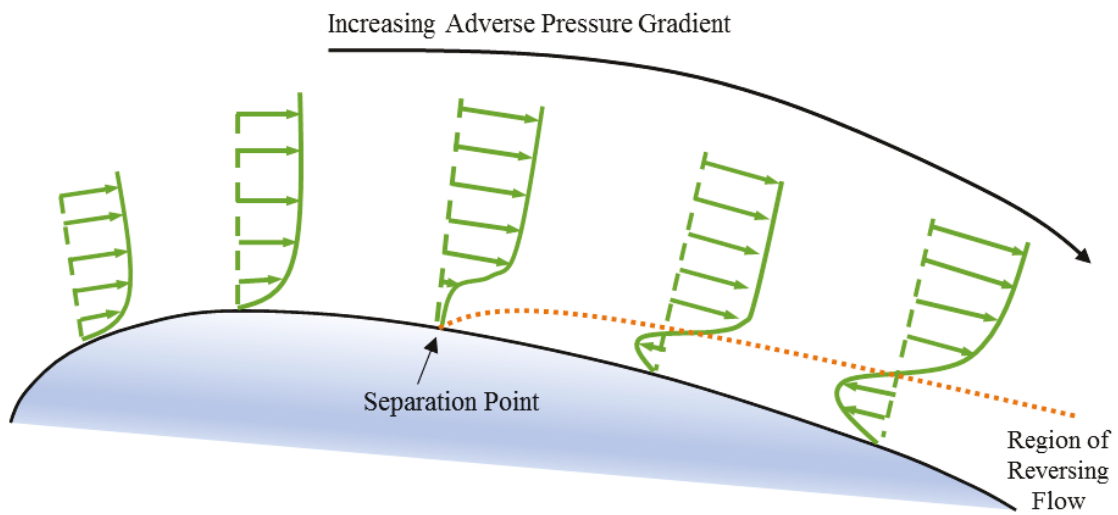


Figure 2.4: Flow separation process on an airfoil surface

To better understand the flow characteristics within a flow field, the pressure distribution is commonly represented as the non-dimensional pressure coefficient. The calculation of the pressure coefficient is shown in Eq. (2.11) where p is the local pressure and p_∞ is the pressure of the freestream.

$$C_p = \frac{p - p_\infty}{1/2 \rho U_\infty^2} \quad (2.11)$$

The pressure coefficient found in Eq. (2.11) is quite useful in scale modeling as it is independent of Reynolds number. Using the Eq. (2.11) and applying Bernoulli's equation, the local velocity (U_e) in a flow field can be found using Eq. (2.12).

$$U_e = U_\infty (1 - C_p)^{1/2} \quad (2.12)$$

There is inherent difficulty when trying to collect convective heat transfer coefficient data for complex surfaces like an airfoil. This extra complexity can be avoided by testing on an unwrapped flat plate test surface and using an insert above the surface that matches the calculated pressure coefficients and velocities found on a NACA 0012 airfoil. Not only is the instrumentation set up simplified by the flat plate set-up, but also flat plate data for heat transfer experiments is plentiful and can be used for validations and comparisons.

Surface Roughness

Surface roughness has continually been an area of experimentation and research in engineering since the early 1900's because it's known to affect flow fields and heat transfer enhancement. Early on, Nikuradse [18] performed experiments that used sand grains cemented onto walls of pipes and channels to create a roughness that could be measured. The effects of sand grain roughness on turbulent boundary layers was recorded

and correlations were created for large Reynolds number flows. Building on the experiments of Nikuradse, Schlichting [19] also studied the effects of roughness on channels. Unlike Nikuradse, Schlichting used geometric shapes (hemispheres, cones, and short and long angles) and related his work to Nikuradse's by deriving correlations that are known as "sand-grain roughness equivalent" and matching the resistance of the geometric shapes to the size of the cemented sand grains. The relationship made by Schlichting has proven useful in cataloging the effect of different surface geometries in terms of a mutual factor.

Experimental studies on roughness since have focused on skin friction and heat transfer enhancement. Hama [20], Clauser [21], and Rotta [22] derived a skin friction law that is dependent on the downward shift found in the roughness geometry, the inner variable velocity, and the density of the roughness. This skin friction law was only applicable to flows with a zero-pressure gradient. Dvorak [23] then used this skin friction law combined with the momentum integral equation and an auxiliary equation to expand previous works to describe shape factors on flows including a non-zero pressure gradient. Dvorak's rough surface law was able to correlate a predictive method to find the shape factor for various geometries.

Shortly after the new turbulent boundary layer correlations were presented by Dvorak [23] and Betterman [24], Simpson [25] realized that the skin-friction law and roughness density correlations previously found were only applicable to small roughness heights (in relation to boundary layer height) and the area close to the wall in the region of constant shear stress. So, Simpson used similar roughness geometries but applied larger roughness intensities. Simpson was able to explain that the stress on the wall is

partially due to the form drag which is created by the pressure distribution on the roughness elements. From this investigation, Simpson provided a more appropriate parameter for roughness density and his hypothesis proved true.

During the investigations of Dorvak and Simpson, Dirling [26] investigated heat transfer on rough surfaces on reentry nose tips. Dirling took into consideration both shape and spacing of roughness elements and was able to provide his own effective sand grain roughness correlation for arbitrary rough surfaces. Dirling was able to unify a correlation for two and three-dimensional roughness investigations. Figure 2.5 is a plot of the experimental data from Dirling's investigation that led to a correlation between roughness density and equivalent sand grain roughness.

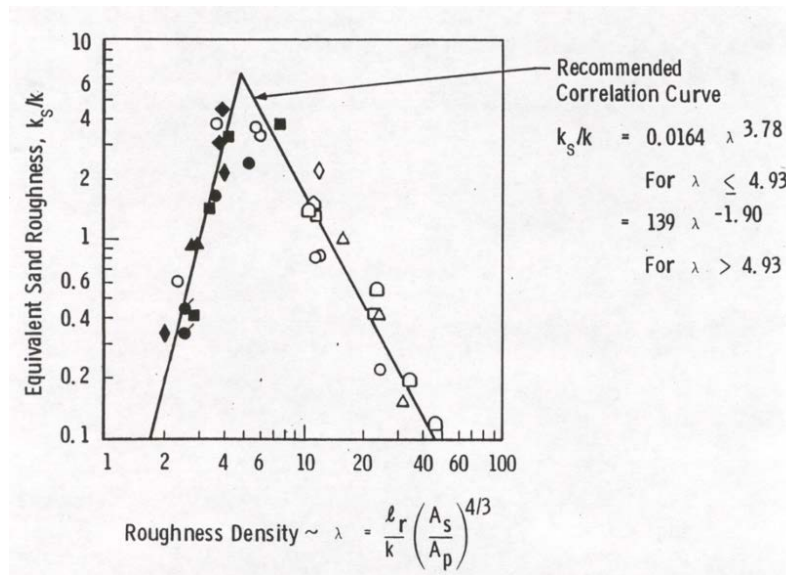


Figure 2.5: Dirling's effective sand-grain roughness correlation [26]

As more empirical data was gathered it became clear to Coleman et al. [27] that several of the assumptions made by Schlichting [19] were questionable. A resampling of the original data lead to the conclusion that skin friction coefficients first reported were

up to 73 percent higher than the corrected values. The sand-grain equivalent roughness values originally presented were also revisited and found to be significantly higher than the new data suggested by 26 to 500 percent. After gathering this information, Coleman et al. [27] offered a new correlation and corrected sand-grain roughness equivalent values for a range of several different geometric shapes. Based on the corrected values, Sigal and Danberg [28] updated the work of Simpson. The new density parameter enabled a better understanding of turbulent boundary layers over a wide range of roughness densities because of its ability to calculate the displacement of the logarithmic-wall profile for both two and three-dimensional roughness.

Alongside his studies of the equivalent sand-grain roughness, Schlichting [19] introduced the discrete element method (DEM), an alternate model used to characterize surface roughness. The DEM finds the total drag on a rough flat plate surface by combining the skin friction drag and the form drag on each individual roughness element. The DEM has proven more effective than the sand-grain roughness model when predicting heat transfer enhancement.

The DEM falls short when evaluating surfaces with roughness elements that are random in shape, spacing, and size. To account for random distributions McClain et al. [29] offered a modified DEM that predicts skin friction and heat transfer for flow over a surface with random roughness surfaces. McClain et al. [30] then used the mean height of random roughness surfaces as the computational location of the no-slip surface. This turned out to agree with experimental skin friction data. McClain et al. [31] furthered the advancement of DEM by the use of Extended Surface – Discrete Element Method (ES-DEM) which treats individual roughness elements as fins from the surface. The model

integrates the change in temperature along the height of the roughness elements for the better characterization of heat transfer.

Lastly, through grid-resolved computational simulations have been used to understand the interactions between rough surfaces and flow. Although this method, when validated, could potentially evaluate roughness effects for a wide range of parameters and reduce experimentation time, the enormous amount of grid points can prove quite costly in time and memory. Bons et al. [32] showed the grid-resolved simulations show superior agreement to empirical data when compared to DEM but require two to three times increase in computation time.

Aircraft Icing

Important Icing Terms

Ice accretion is a term for the collection and evolution of ice on a surface over time. This particular study focuses on ice accretion on an in-flight airfoil. Some important parameters associated with the ice accretion process are liquid water content (LWC) and mean volumetric diameter (MVD). LWC is the amount of water (mass) per unit volume of air. A high LWC can describe a flow containing a large quantity of droplets within the unit volume or a flow in which the droplets are of very large size. MVD is the diameter of the median droplet in the flow. That is, half of the droplets will have a diameter larger than the MVD and the other half have diameters smaller than MVD [33]. The LWC provides information on the rate at which ice will accrete on the aircraft surface while the MVD is related to the extent of the ice accretion.

Safe flight through icing conditions is defined and controlled by the FAA. These safe conditions depend mostly on the LWC and MVD but also take into account altitude,

temperature, and extent of the cloud [33]. Historically the FAA has used what is called Appendix C conditions to characterize icing conditions in its determination of safe flight. Appendix C conditions consist of having partially frozen or super-cooled droplets with an MVD of 1- μm to 50- μm and thought of as “freezing cloud” conditions [2]. More recently, however, the FAA has updated its focus to Appendix O conditions for ice protection system certification. Appendix O conditions are commonly referred to as super-cooled large droplet (SLD) conditions, or “freezing drizzle and rain” [3]. SLD conditions are characterized as having partially frozen or super-cooled droplets with an MVD larger than 50- μm .

During the ice accretion process, the formation and evolution can be categorized into two regimes: rime ice and glaze ice. In the rime ice regime, 100% of the water droplets that impinge on the aircraft surface freeze on impact. Rime ice occurs at freestream temperatures well below freezing (usually close to 0°F). Small pockets of air form between the freezing droplets which create a white opaque brittle ice shape with significant roughness. In the glaze ice regime, not all of the impinging droplets freeze on impact, this causes a layer of liquid water runback on the surface. Glaze ice occurs closer to the freezing point (32°F), and creates a clear dense ice shape. If the cloud conditions contain droplets that vary significantly in size, mixed icing can occur. Mixed ice is a combination of glaze and rime ice and is usually a hard and rough ice shape [34].

A non-dimensional representation of the mass flux equation is given in Eq. (2.13) and is used to determine the accumulation parameter. V is the freestream velocity, β is the cloud collection efficiency (discussed in detail below), and Δt_s is the exposure time.

$$m'_w = LWC \cdot V \cdot \beta \cdot \Delta t_s \quad (2.13)$$

The accumulation parameter is used to describe the extent of ice growth, in terms of the radius of the leading edge of an airfoil, on a flat plate perpendicular to freestream flow for a particular exposure time [35]. In ice accretion studies the accumulation parameter characterizes the roughness accumulation on a surface. Eq. (2.14) is used to calculate the accumulation parameter, A_c . For a particular airfoil, r_a is the leading-edge radius of curvature and ρ_{ice} is the density of ice at the temperature of the freestream.

$$A_c = \frac{LWC \cdot V \cdot \Delta t_s}{2 \cdot r_a \cdot \rho_{ice}} \quad (2.14)$$

The accumulation parameter is proportional to the icing time and the rate at which droplets impinge on the surface. Also, the accumulation parameter has the ability to account for exposure time, meaning a high accumulation parameter designates a high accretion rate [35,36].

During an icing event, not all of the droplets in the flow impinge on the airfoil as a portion of the smaller droplets follow the path of flow around the airfoil. The number of droplets that impinge on the airfoil is dependent on the MVD of the droplets in the flow. To describe the fraction of the total number of droplets that will impinge on the surface, Ruff [37] derived a term known as the collection efficiency. This derivation is dependent on the droplet inertial parameter, K . This parameter was first developed from Tsao and Lee [38] and was created by applying a length scale to the Stokes number. Eq. (2.15) and (2.16) shows the Stokes number, Sk , and the inertial parameter.

$$Sk = \frac{\rho_w \cdot V \cdot MVD^2}{18 \cdot \mu_{air} \cdot L} \quad (2.15)$$

$$K = \frac{\rho_w \cdot V \cdot MVD^2}{18 \cdot \mu_{air} \cdot r_a} \quad (2.16)$$

Langmuir and Blodgett [39] offered a stagnation point collection efficiency term using a modified version of the droplet inertial parameter (K_0) based on the droplet range parameter ($\frac{\lambda}{\lambda_{sk}}$) given by Eq. (2.17).

$$\frac{\lambda}{\lambda_{sk}} = \frac{I}{0.8388 + 0.001483Re_\delta + 0.01847\sqrt{Re_\delta}} \quad (2.17)$$

Where the Re_δ term is the droplet Reynolds number shown in Eq. (2.18).

$$Re_\delta = \frac{\rho V MVD}{\mu} \quad (2.18)$$

Eq. (2.19) and (2.20) present the modified version of the droplet inertial parameter and the stagnation point collection efficiency term of Langmuir and Blodgett, respectively.

$$K_0 = \frac{I}{8} + \frac{\lambda}{\lambda_{sk}} \left(K - \frac{I}{8} \right) \quad (2.19)$$

$$\beta_0 = \frac{1.4 \left(K_0 - \frac{I}{8} \right)}{1 + 1.4 \left(K_0 - \frac{I}{8} \right)} \quad (2.20)$$

Using the stagnation point collection efficiency, the local cloud collection efficiency (β_s) at a location along an airfoil may be estimated using Eq. (2.21).

$$\beta_s \approx \beta_0 \cos(\gamma_s + \alpha) \quad (2.21)$$

In the local cloud collection efficiency, γ_s is the surface angle relative to airfoil design coordinates and α is the angle of attack of the airfoil [40]. A flow with a large collection efficiency is the result of a higher percentage of impinging droplets which is directly related to a high cloud MVD.

The theoretical, leading edge, fully dense rime ice thickness ($N_{0,R}$), directly proportional to the cloud collection efficiency and the accumulation parameter, is presented in Eq. (2.22).

$$N_{0,R} = 2r_0 A_c \beta_0 \quad (2.22)$$

This thickness calculation is important when scaling roughness and thickness geometries discussed later in this chapter.

Ice Accretion Process

The first experiment which captured the icing process was performed by Olsen and Walker [41] in 1986. A high-speed camera was placed in the Icing Research Tunnel (IRT) at NASA Glenn Research Center to photograph and film ice accretion forming on an airfoil. A symmetric airfoil mounted at a zero angle of attack was exposed to flows ranging from 50 to 320 km/hr with a freestream temperature ranging from just above freezing down to -25°C . Observed was the impingement of super-cooled droplets on the test airfoil. The droplets coalesced and grew to form a thin film. Once the droplets grew large enough and the aerodynamic drag overcame the surface tension, the film moved downstream along the airfoil. The film continued to the trailing edge until it froze to the surface and became ice roughness. As super-cooled droplets continued to impinge on the surface and got pulled downstream, an ice plateau at the stagnation region formed, which is a thick layer of ice with negligible roughness. Figure 2.6 depicts the distinct regions thought to be present when ice forms on a symmetrical airfoil at zero angle of attack.

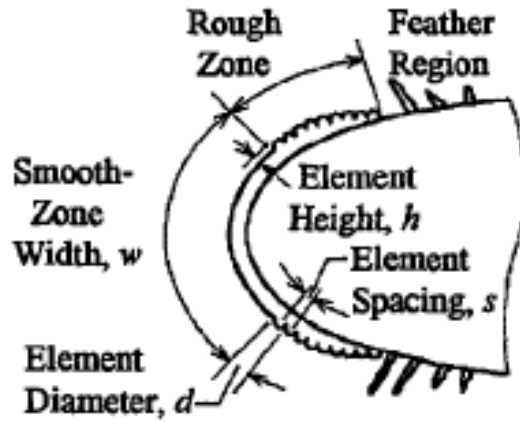


Figure 2.6 Ice accretion on an airfoil stagnation region [41]

Ice Accretion Modeling

The first model for airfoil icing was produced by Messinger [42] in 1953. The Messinger model was based on conditions governing the equilibrium temperature of an insulated, unheated airfoil exposed to icing through a one-dimensional energy balance. This energy balance considers gains associated with viscous heat from friction at the boundary layer, kinetic energy from droplet impingement, and the latent heat of fusion. Energy losses are considered from convection, sensible cooling by absorption of impinging droplets, and evaporation or sublimation. Messinger's model of an iced airfoil and the heat transfer gains and losses associated with it is shown in Figure 2.7.

Messinger [42] also reported that under conditions where the surface equilibrium temperature is 32°F that not all of the impinging droplets will freeze on impact. Messinger quantifies the amount of freezing droplets as a non-dimensional “freezing fraction” which is a number between zero and one. At a freezing fraction equal to one, all of the impinging droplets freeze on impact (rime ice). When the freezing fraction is less

than one, not all droplets are freezing on impact and cause water runback (glaze ice) beginning at the stagnation point.

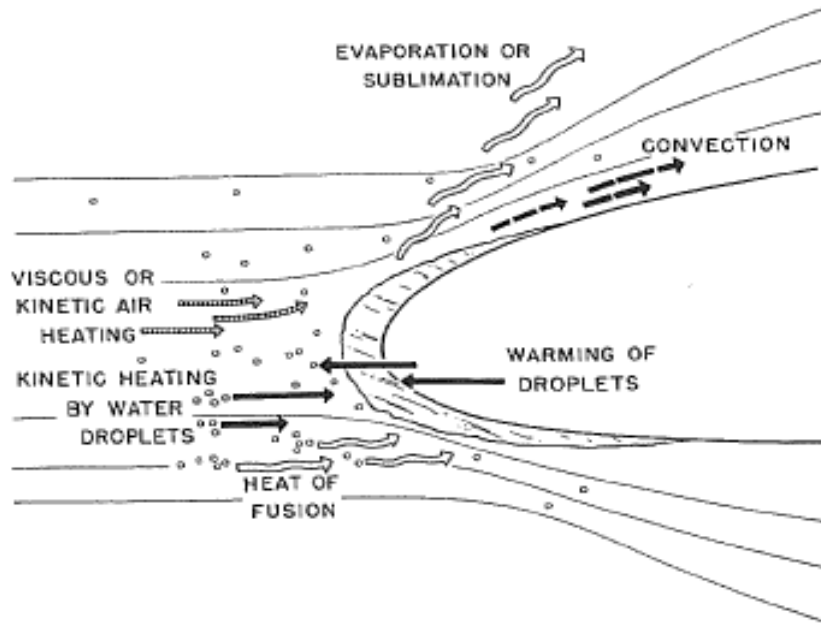


Figure 2.7: Modes of energy transfer for an unheated airfoil in icing conditions [42]

The model of Messinger proved useful in the fundamental understandings of ice accretion, and modified versions are still used today. One version is used in the NASA ice accretion code LEWICE which implements the equivalent sand-grain roughness model developed by Nikuradse and Schlichting based on the freezing fraction of Messinger. The height of the ice roughness calculated by LEWICE is given by Eq. (2.23).

$$x_k = \frac{1}{2} \sqrt{0.15 + \frac{0.3}{N_{f,stag}}} \quad (2.23)$$

$N_{f,stag}$ is the freezing fraction at the stagnation point and is calculated separately.

LEWICE then employs a semi-empirical integral boundary layer solver based on turbulent momentum thickness and the equivalent sand grain roughness height to calculate convective heat transfer coefficients.

Using equivalent sand-grain roughness for ice roughness calculations has been criticized because ice roughness is different in both size and distribution density [42]. Studies have also proved that the use of ordered arrays of roughness elements consisting of regular and consistent geometries cannot correctly model heat transfer enhancement of a real ice roughness surface [43,44]. Shin [45] performed research in the IRT to compare the roughness heights of an iced airfoil to the predictions of LEWICE's sand-grain roughness model. He determined that LEWICE poorly predicted trends in magnitude of roughness heights when certain icing conditions (LWC, flow velocity, temperature) were changed. LEWICE is over simplified by only using a single parameter ($N_{f,stag}$) to predict roughness heights over a range of icing conditions. Figure 2.8 shows an example of a result from Shin's experiments comparing measured roughness heights and predicted sand-grain roughness heights as a function of different set values of LWC.

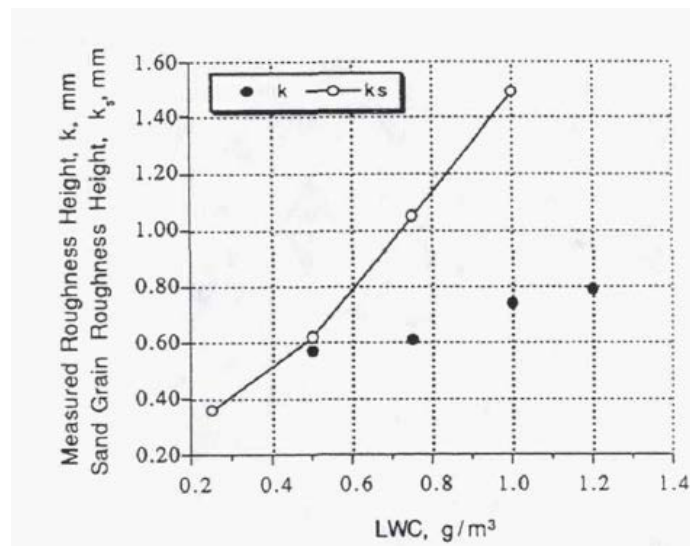


Figure 2.8: Comparison of measured roughness height with the predicted sand-grain roughness height [45]

Historical Ice Roughness Investigations

Many studies have been performed to better understand the effect initial ice roughness on an airfoil has on the development of ice accretions. Poinatte et al. [46] investigated the effect ice roughness had on the convective enhancement for an airfoil. Hemispherical elements of identical diameter were fastened in four different ordered patterns to a NACA 0012 airfoil. The patterns are shown in Figure 2.9. As hypothesized, the addition of roughness elements to an airfoil greatly increased the convective enhancement when compared to a clean, smooth airfoil. Also observed was the increase in roughness element density yielded an increase in in heat transfer up to 54%.

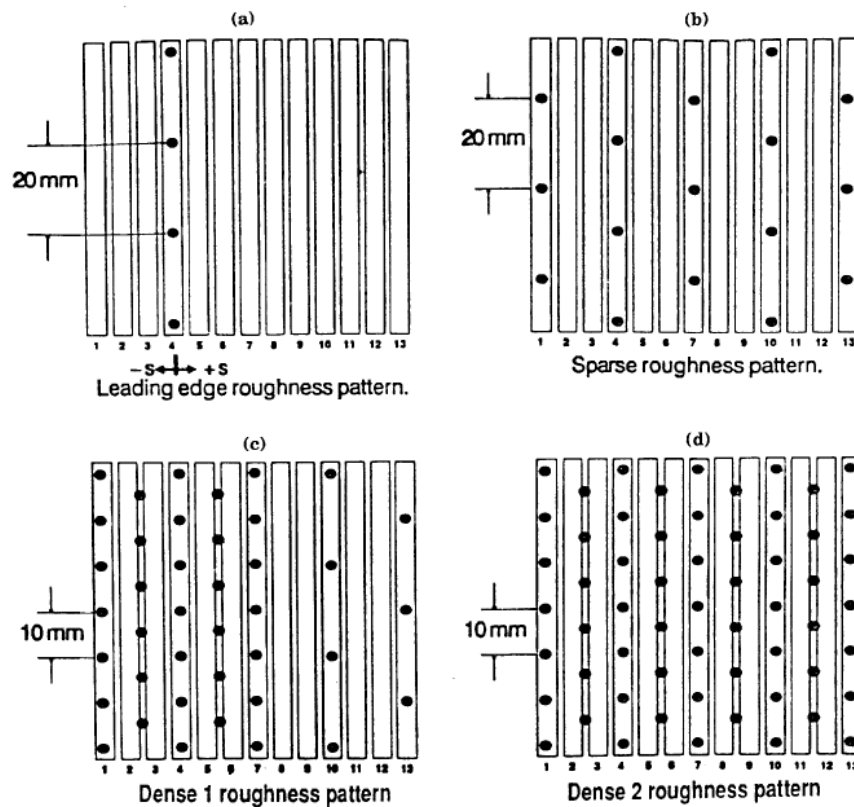


Figure 2.9: Ordered roughness distributions used by Poinatte et al. [46]

Bragg et al. [47] performed similar experiments using uniform roughness elements on the surface of a NACA 0012 airfoil but focused on the effects of the smooth-to-rough transition. Also, the freestream turbulence intensity was varied to observe its effect on the convection enhancement in the leading 20 to 40% of the airfoil. Downstream of this location the enhancement due to the elevated freestream turbulences experienced a significant drop off. This is explained by the unperturbed boundary layer transitioning earlier for the elevated turbulence cases. Figure 2.10 displays the results of the experiments performed by Bragg et al. [47]. It is important to note that these experiments performed [46,47] used a simplistic roughness model that does not accurately represent real ice roughness.

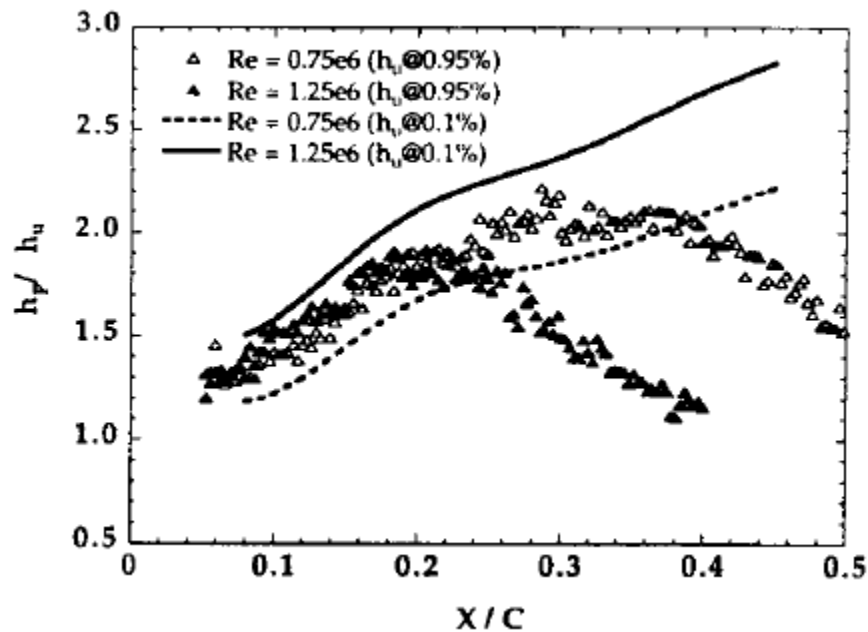


Figure 2.10: Heat transfer enhancement with varying freestream turbulence [47]

Expanding on the work of Poinsette et al. [46] and Bragg et al. [47], Dunkhan et al. [48] used testable models of NACA 0012 airfoils from the IRT to cast realistic ice

roughness distributions on the surface of an airfoil from aluminum. Figure 2.11 shows one of the aluminum cast models created by Dunkhan et al.

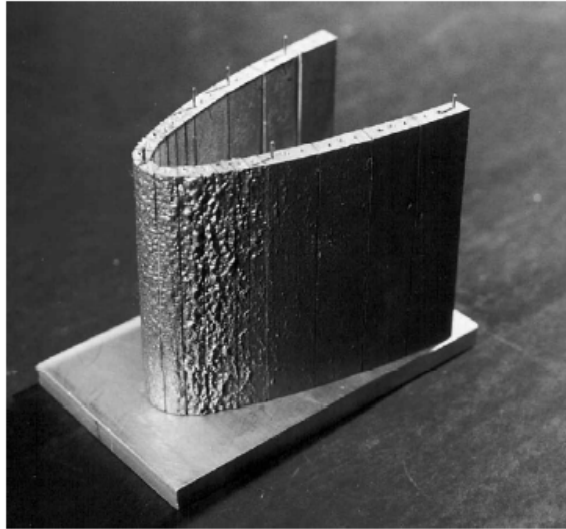


Figure 2.11: Aluminum cast of if roughness on a NACA 0012 airfoil [48]

The models were fitted with heaters and heat-flux gauges to measure local heat transfer coefficients along the airfoil surface. The heat transfer coefficients observed by Dunkhan et al. were higher than those observed by Poinsatte et al. These results were significant in ice accretion research because they emphasized the importance of using realistic ice roughness surfaces when characterizing heat transfer enhancement on iced airfoils. On a similar casted roughness surface to the investigation of Dunkhan et al., Han and Palacios [49] showed that their experimental measurements of ice roughness heights and heat transfer enhancements over predicted the convection enhancement predictions of LEWICE by 200 to 391%.

Anderson et al. [36] and Shin [45] performed investigation in the IRT at NASA Glenn which studied ice roughness distributions on various NACA 0012 airfoils subjected to Appendix C conditions. Using imaging technology, Anderson et al. reported

a statistical description of the roughness elements. These statistics included mean roughness element diameter, the standard deviation of said diameters, and the smooth zone width. These statistical descriptions provide a complete account of ice roughness parameters corresponding to Appendix C conditions.

Investigations of convective enhancement of roughness surfaces containing roughness distributions mimicking those found on an airfoil with real ice roughness were performed by Tecson and McClain [50]. To create the simulated roughness surfaces, Tecson and McClain [51] developed a Lagrangian droplet simulator which was used. The simulator models droplet impingement and coalescence, thus imitating how real ice roughness forms on an aircraft surface. Once a simulation is run, a data file is output with the precise location of the centroid of each droplet along with the droplet's diameter. The resulting pattern was modified using the statistics from previous studies in the IRT [36,45] to match surface characteristics and statistics. The investigations of Tecson and McClain provided an alternate method to characterize heat transfer enhancement on realistic ice roughness surfaces. Figure 2.12 is a solid model of a section of a surface created by Tecson and McClain [51].

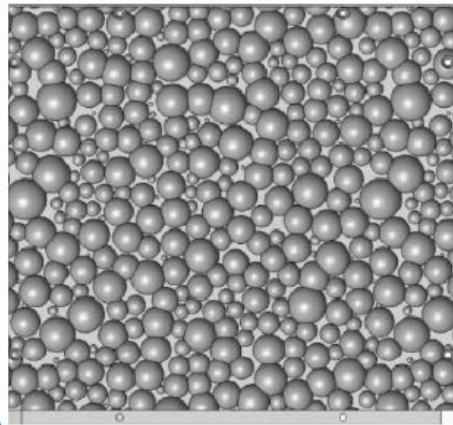


Figure 2.12: Solid model of realistic ice roughness surface [51]

Walker et al. [52] expanded on the work of Tecson and McClain [50,51] by imposing varying boundary conditions and observed the convective heat transfer. Walker et al. determined that varying boundary conditions had little or no effect on the convective enhancement over the realistic ice surface.

Recent Ice Roughness Investigations and Surface Creation

This section describes recent ice roughness investigations. The creation of simulated and real ice roughness surfaces in these recent investigations is relevant to this study.

Smooth Starting Length (SSL) Surface Patterns

Using the Lagrangian droplet simulator described above, a random distribution of hemispheres was created by Shannon and McClain [TAIAA] that matched the Appendix C statistics reported by Anderson et al. (case identifier 052996.04). Table 2.1 displays the characteristics reported by Anderson et al. and those matched by the SSL surface. The SSL surface statistics were scaled by 10 compared to the tested airfoil for testing purposes discussed later. Note: average spacing was not reported by Anderson et al., but only stated the elements were “close” and “touching”.

Table 2.1: Comparison of measured Appendix C icing roughness condition and SSL parameters [53]

Case Identifier	D_{mean} (mm)	S_E (mm)	$(P/D)_{mean}$	P_{mean}/D_{mean}	H/D	W_{SZ} (mm)
052996.04	0.936	0.372	“touching”	“touching”	0.515	23
052996.04_x10_SSL	10.37	3.81	1.032	0.84	0.5	230

The smooth zone width for 052996.04 was not reported by Anderson et al. but was detailed by Walker et al. [52] that the original images were obtained to measure the width of the smooth zone width. The 052996.04 and the SSL surfaces have no variation in roughness element height in the downstream direction after the abrupt smooth to rough transition.

After the creation of the roughness pattern, Shannon [53] constructed two solid models, one of hemispherical elements, and one of conical elements. Figure 2.13 shows the solid models of the two SSL distributions. The smooth-to-rough transition is abrupt, and the roughness properties downstream are constant.

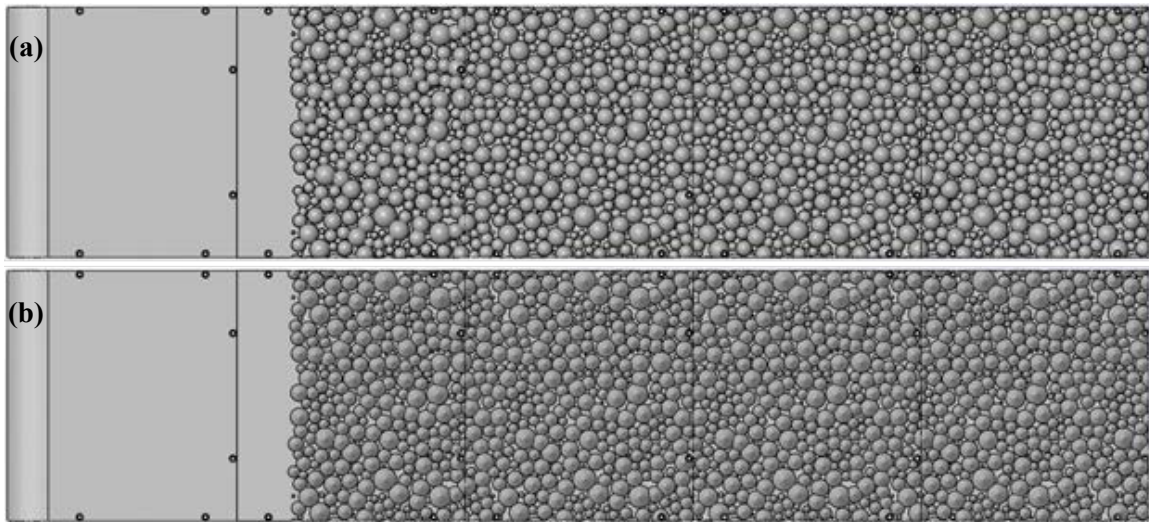


Figure 2.13: Heated Section SSL Panels: (a) 052996.04_x10_SSL_Hemispheres, (b) 052996.04_x10_SSL_Cones [53]

IRT Surface Patterns

McClain et al. [29] investigated the measured variation in roughness heights along the surface of a NACA 0012 airfoil subject to Appendix O icing conditions in the IRT.

The results from the experiments determined that the abrupt smooth-to-rough transition

was not representative of a real ice roughness distribution and the roughness heights decay in the downstream direction following the location of the maximum roughness height. This was a significant finding as the historical investigation discussed above were characterized by an abrupt transition, contained constant roughness properties in the downstream direction, and do not properly model real ice roughness properties. Figure 2.14 shows the variation in roughness height along the surface of a NACA 0012 airfoil for several Appendix O conditions.

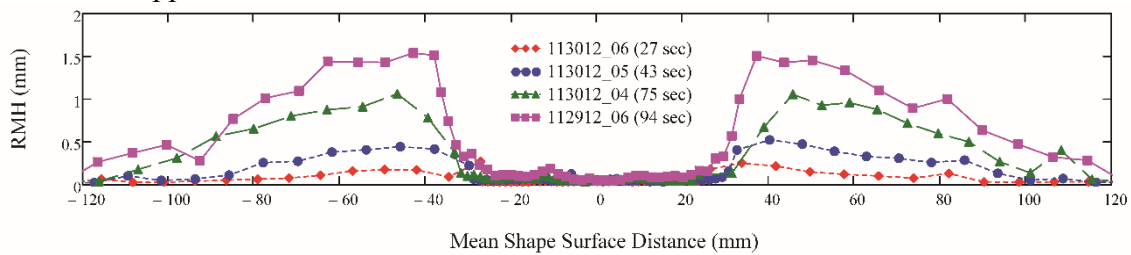


Figure 2.14: Roughness height measurements in Appendix O conditions [29]

The IRT realistic ice roughness surfaces were created by Shannon [8] and attempted to model realistic ice distributions in a more contemporary approach. That is, to create simulated roughness surfaces similar to the SSL droplet patterns, but with variations along the downstream direction match a real ice roughness distribution as reported by McClain et al. [29]. To do this, the information from the laser scan data from McClain et al. and the characterized roughness from the SOM approach of McClain and Kreeger [31], discussed in detail below, were used to characterize the roughness variations along the roughness surface in the downstream direction. Eq. (2.24) is used to calculate the local, 99%-Gaussian roughness maximum height variation at each codebook vector.

$$RMH_{\mathbf{b}^n} = 3.09R_q = 3.09 \left[\frac{1}{J} \sum_{j=1}^J N_{\mathbf{x}^j}^2 \right]^{\frac{1}{2}} \quad (2.24)$$

Figure 2.15 displays the results of using Eq. (2.19) at each codebook vector for the 113012.04 case. Figure 2.15 shows that the maximum RMH value for the 113012.04 case, when scaled by a factor of ten, is essentially the same height as the largest roughness element size in the SSL pattern. Therefore, the same base pattern used for the SSL surface is used to create the roughness pattern for the IRT surface. Also presented in Figure 2.15 is that the 113012.04 case has a smooth region up to 30-mm from the stagnation point. The roughness then grows rapidly to its maximum value close to 50-mm downstream, and decays slowly towards the 90-mm mark. In order to capture the variation on roughness along the flow direction for the IRT pattern, a series of transition functions were created to imitate the RMH variation of the 113012.04 surface. A combination of three transition functions created a scaling function which captured the measured RMH values. The resulting scaling function is shown in Figure 2.15 and was multiplied to the SSL surface pattern and scaled up by 10x to create the IRT surface pattern.

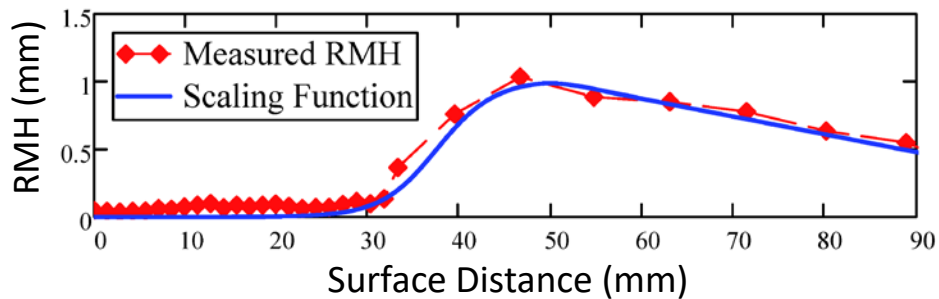


Figure 2.15: 99%-Gaussian RMH values for the 113012.04 Case with the IRT Scaling Function [8]

Similar to the SSL surfaces, after the roughness patterns for the IRT surfaces were created, Shannon [8] constructed two solid models of the pattern with conical and hemispherical elements. Figure 2.16 shows the solid models of the IRT surfaces.

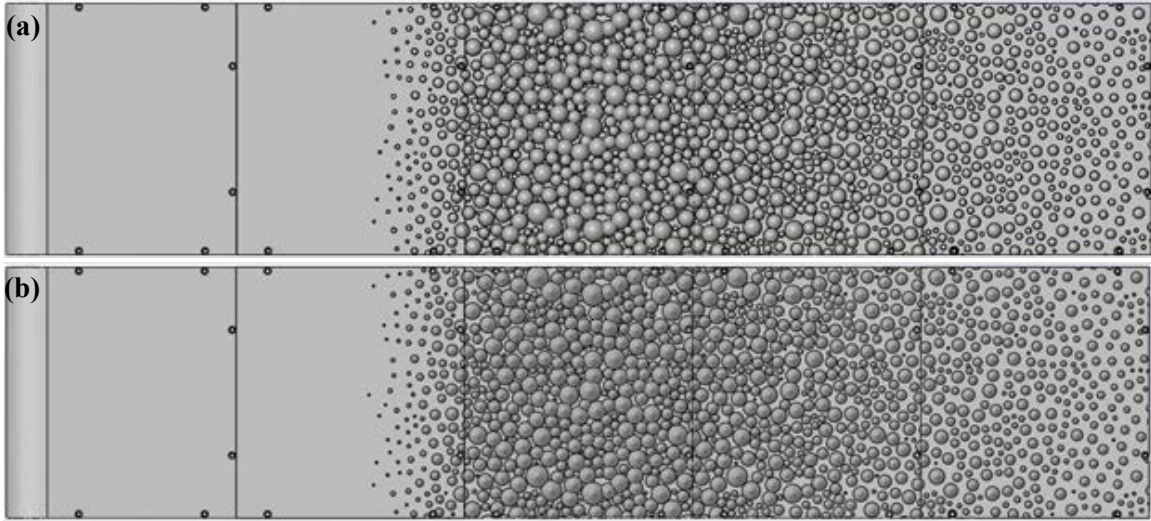


Figure 2.16: Heated Section IRT Panels: (a) 113012.04 IRT Hemispheres, (b) 113012.04 IRT Cones [53]

It can be observed from Figure 2.16 that the variation of roughness along the surface along the downstream direction for the IRT surfaces better replicates real ice roughness distributions reported by McClain et al. [29]. Also seen in Figure 2.16 is that the IRT and SSL surfaces share very similar roughness characteristics near the middle of the third roughness panel even though they were created from different conditions.

Real Ice Roughness Surfaces

Following the investigation of Shannon, Hawkins [10] created a real ice roughness surface using the laser scan data for the 113012.04 run of McClain et al. [29] to compare to the realistic ice roughness (IRT) surfaces described above. McCarrell [11]

made three more real ice surfaces from the laser scan data to investigate the effects of increasing exposure time on a 21-in NACA 0012 airfoil. An account of the surface creation is given below.

Based on “Appendix O”, or supercooled large droplets (SLD), an experiment run by McClain et al. [29] examined ice roughness formation in short duration SLD icing events. A 21 in NACA 0012 airfoil at 0° angle of attack spanning the 72 inch test section of the IRT was used for all of the SLD events. The environmental conditions set for each surface are displayed in Table 2.2.

Table 2.2: Conditions of the Four SLD Studied Surfaces [11]

Case Identifier	T_t (°F)	V (knots)	MVD (μm)	LWC (gm/m ³)	Δt_s (s)	A_c	β_0	$\overline{N}_{0,R}$ (mm)
113012.05	27.7	129.7	150	0.6	43	0.112	0.969	0.92
112912.02	27.8	129.7	100	0.6	55	0.143	0.950	1.15
113012.04	27.7	129.7	150	0.6	75	0.195	0.969	1.60
112912.06	27.7	129.7	150	0.6	94	0.245	0.969	2.00

It is important to note that the 112912.02 case experienced droplets with an MVD of 100 μm, whereas in the other cases the MVD is 150 μm. This is attributed to the fact that the 55 second exposure time under an MVD of 150 μm showed significant variations in the spanwise direction, suggesting there was an error during the laser scanning, thus the 112912.02 case under 100 μm without spanwise variation was a more appropriate option. Each of the four cases were exposed to increasing exposure times, Δt_s , from 43 to 94 s. These variations in exposure times between the four studied surfaces yield a temporal roughness development. Once the exposure time was met, the wind tunnel speed was reduced and the tunnel was kept at -4 °C to prevent melting. The ice on the

airfoil was painted with titanium dioxide paint and a ROMER Absolute Arm was placed in the IRT to perform laser scans from the center-span of the airfoil. Figure 2.17 shows elevation maps of the four laser scanned surfaces used in this study.

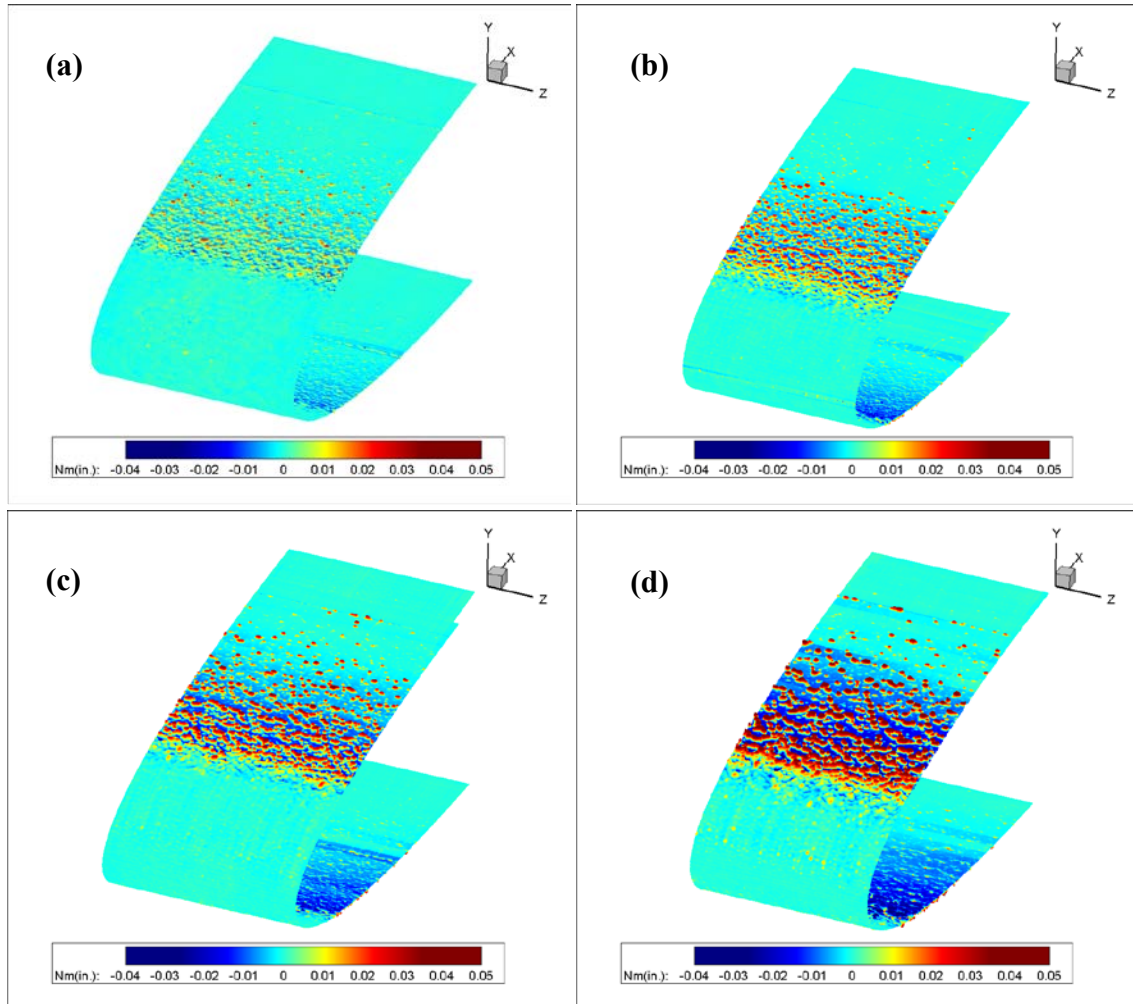


Figure 2.17: Laser Scanned Roughness Data (a) 113012.05, (b) 112912.02, (c) 113012.04, (d) 112912.06 [11]

Unwrapping Laser Scan Data

To characterize the roughness and unwrap the point clouds of the iced surfaces used in this experiment, a self-organizing map (SOM) method by McClain and Kreeger [29] was used. This method uses relatively small group codebook vectors in order to

represent the trends of the larger data set. Individual codebook vectors are linked together linearly in order to complete the whole SOM. The linked codebook vectors represent the mean iced surface, or ice manifold. A coordinate system for the data is created using an X-Y plane in reference to the chord and chord-normal plane, respectively. N is the direction normal to the ice manifold and S moves along the surface of the ice manifold. Similarly, N^0 and S^0 follow normal-to and along the surface of the clean airfoil. Figure 2.18 shows an example of the coordinate system used in the unwrapping process.

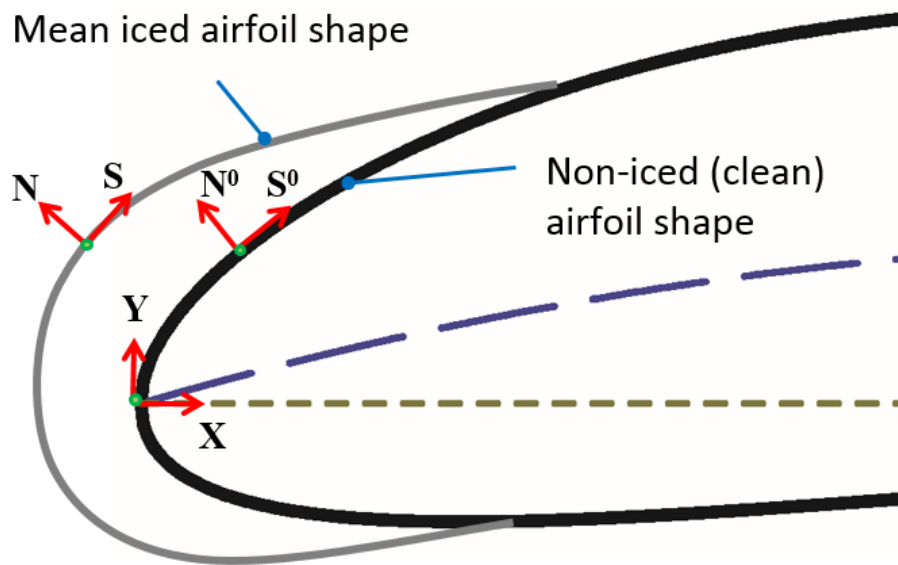


Figure 2.18: SOM Coordinate System Example [54]

Unwrapping the surface required a conversion of the airfoil shape in the S and N coordinates to traditional X-Y coordinates using a discrete arc-length approach. The distance between the stagnation point and the arc length at the end of the linked codebook vectors is initially known, and the surface distance of each of the remaining codebook vectors was calculated and represented as an S-distance along the ice manifold. Naturally, the conversion between S-distance and X-distance along the airfoil yields a skewed

representation of the unwrapped surface. It is noted that the current study focuses on ice roughness rather than thickness, so the data points were shifted because the first ten to fifteen inches of the iced surface, the glazed plateau, has negligible roughness compared to further downstream from the stagnation region. The data was appropriately leveled by applying more shifts and by eliminating ice thickness from the mean ice manifold.

Significant roughness had been identified and the surface was properly leveled. Figure 2.19 shows an example of the unwrapped and final point cloud for one of the surfaces used in this study, the 113012.04 case.

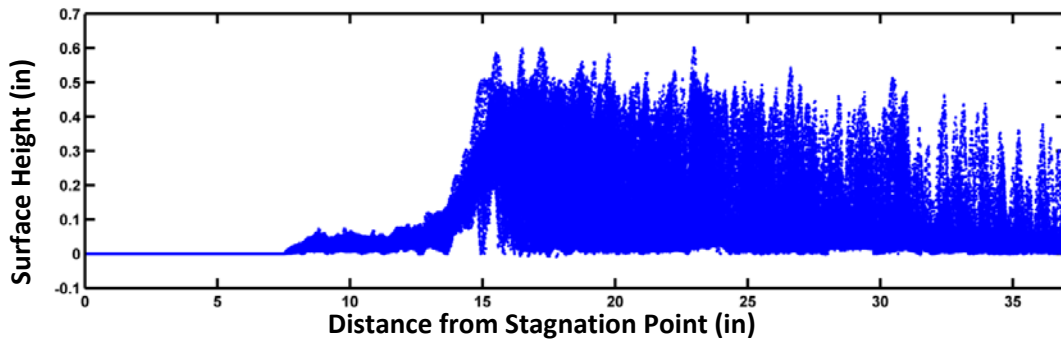


Figure 2.19: Surface Height Distribution of Laser Scanned Ice Roughness [10]

In order to manufacture the unwrapped roughness surface, the point cloud was projected in three dimensions on a flat surface. Before manufacturing the 3D surface, a quadratic interpolation code was used to generate a surface function that fit the point cloud. Initially, the projected 3D surface contained large gaps between the data points, thus the surface was resampled to create new surface points and allowed for proper STL file creation and CNC machining. One section of the projected surface map, along with the resampled surface map are presented in Figure 2.20. After the resampled point cloud map was created, solid models of the real ice surfaces were made and are shown in Figure 2.21

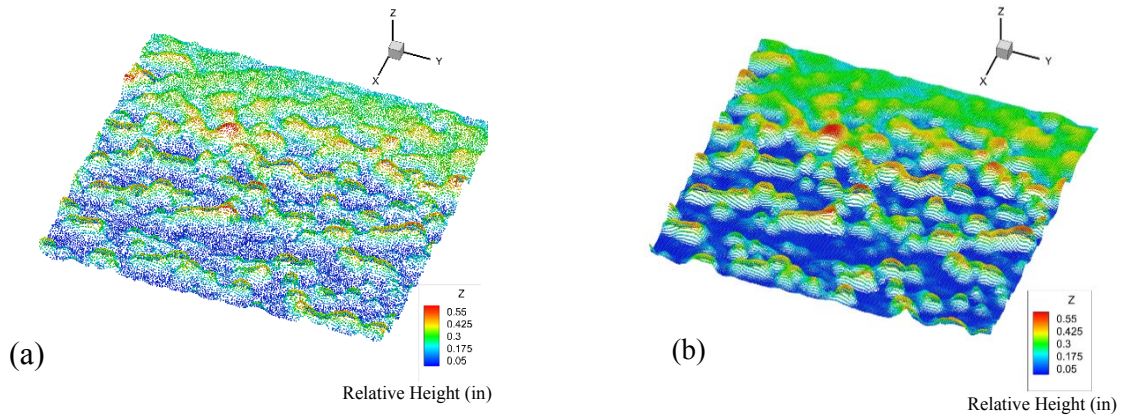


Figure 2.20: (a) Leveled Point Cloud Surface Height Map, (b) Resampled Point Cloud Height Map [10]

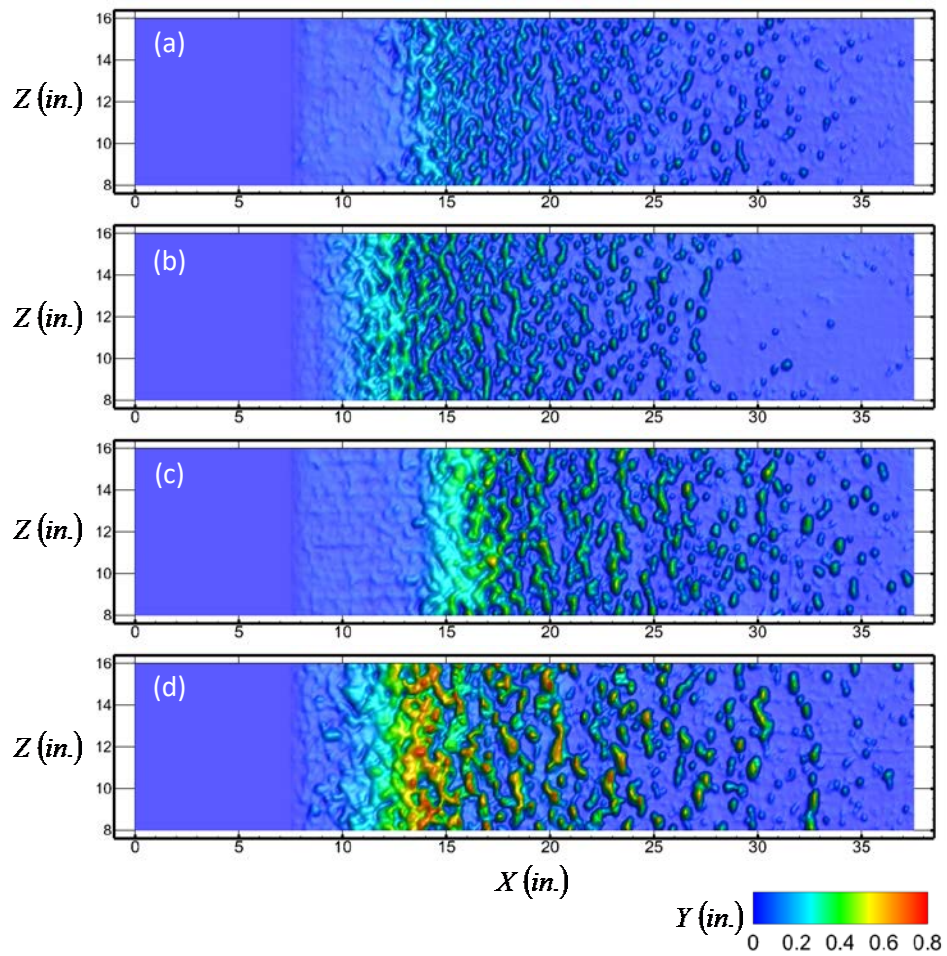


Figure 2.21 Solid models of the real ice roughness surfaces: (a) 113012.05, (b) 112912.02, (c) 113012.04, (d) 112912.06 [11]

Autocorrelation Surface Creation

The investigation of Hawkins [10] determined that the IRT surfaces did not accurately model the heat transfer and boundary layer behavior of the corresponding real ice surface. Clemenson [12] then attempted to create a new method to model the 113012.04 real ice surface with deterministic features that can be described mathematically in a simple manner.

The two surfaces created by Clemenson [12] use roughness elements of cones and hemispheres with elliptical shaped bases in order to more closely match the ridge-like elements of the 113012.04 surface. To capture the surface statistics of the 113014.04 surface, an autocorrelation was performed on an 8-in by 8-in region near the area of peak roughness 18-in downstream of the leading edge. Figure 2.22 displays the region of peak roughness on the 113012.04 surface used for autocorrelation.

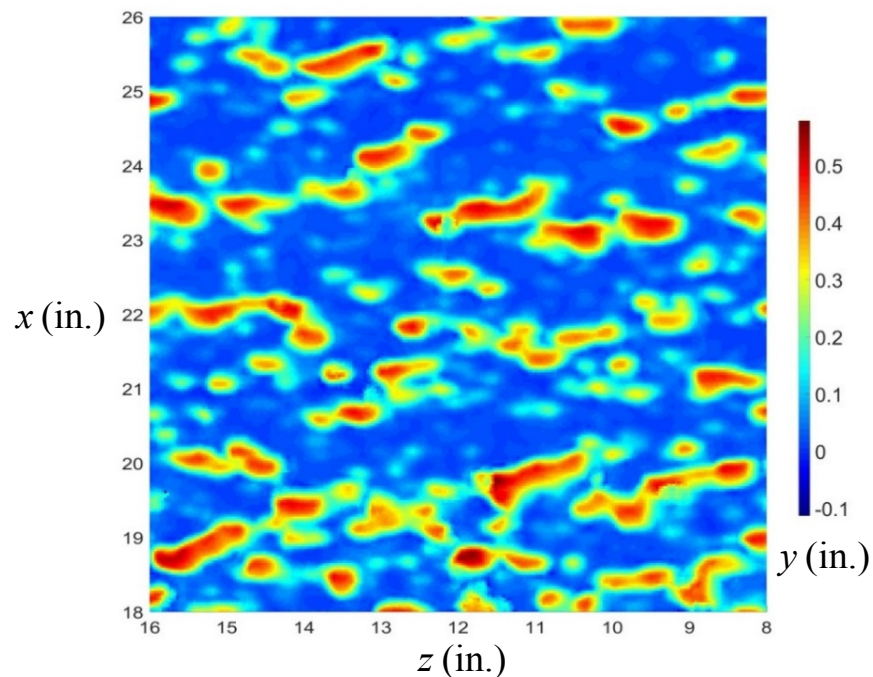


Figure 2.22: Peak Roughness Area Analyzed for Surface Characteristics [12]

The root-mean-square height and element ridge spacing were gathered from the autocorrelation. To determine the eccentricity of each element's elliptical base, points were taken from the autocorrelation and parabolized from the maximum height down to the surface, in both the streamwise and spanwise directions. The intersection between the parabola and the surface was used to calculate the elemental eccentricity, which was determined to be 0.5962. The eccentricity value was applied to a surface mapping program to generate the two surfaces: ellipsoids and elliptical cones. To match the calculated ridge spacing and root-mean-square height of the 113012.04 surface, the surface generation program iterated the element spacing. By characterizing and matching the ridge spacing of the real ice surface, these analog surfaces are able to emulate the downstream eddy interactions found on real ice accretions. Once the surface generation is complete, an autocorrelation is performed on the two new surfaces in order to confirm statistical matching. Figure 2.23 shows the autocorrelation applied to the 113012.04 surface in comparison to the autocorrelations of the newly generated surfaces.

Once surface statistics were confirmed to be matching, solid models of the roughness patterns were constructed. Figure 2.24 shows the solid model of the 113012.04 surface alongside the models of the ellipsoidal and elliptical surfaces, the two surfaces generated through autocorrelation and surface generation iteration.

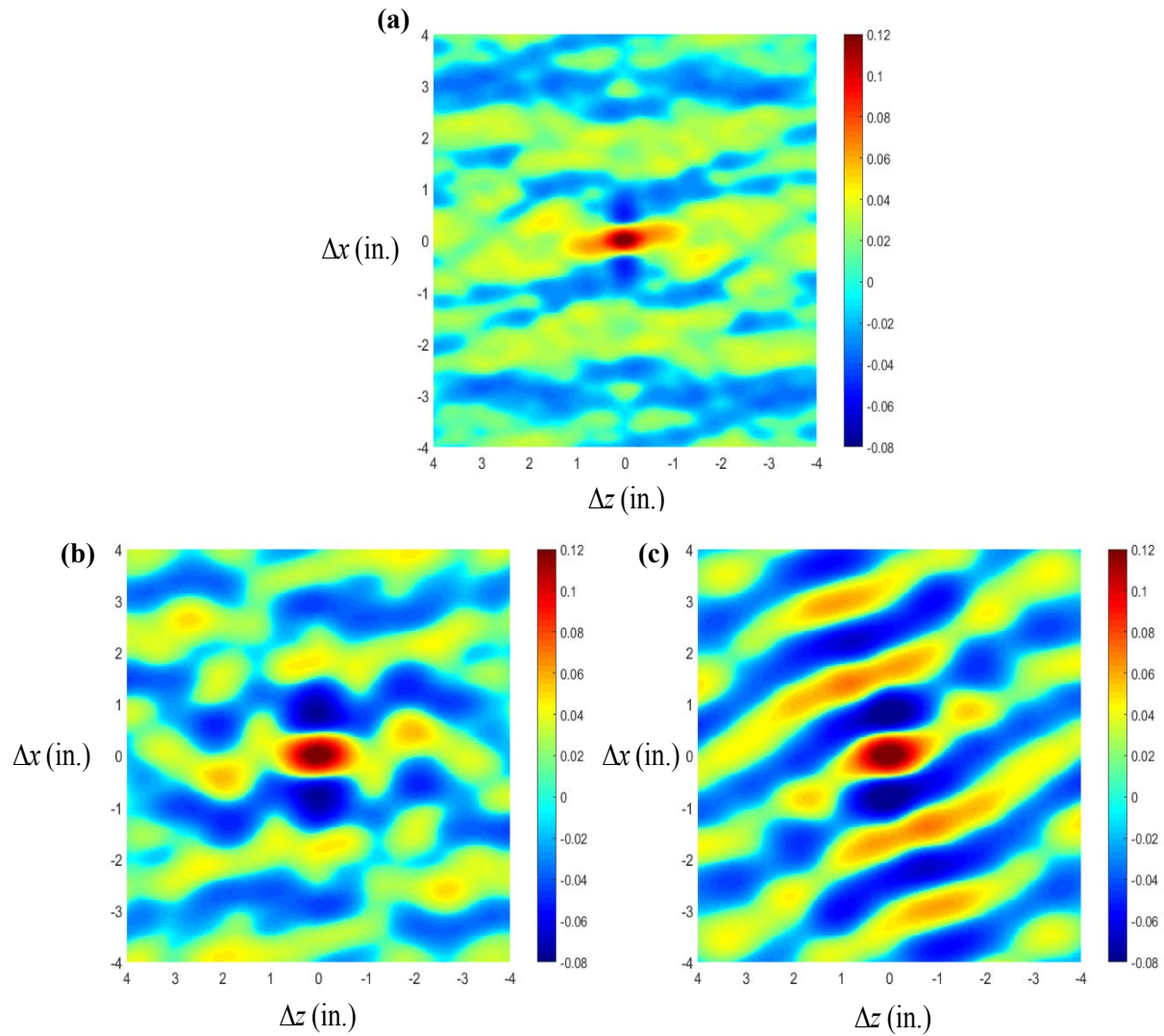


Figure 2.23: Autocorrelation comparison of (a) real ice surface and (b) ellipsoid surface, and c) elliptical cone surface [12]

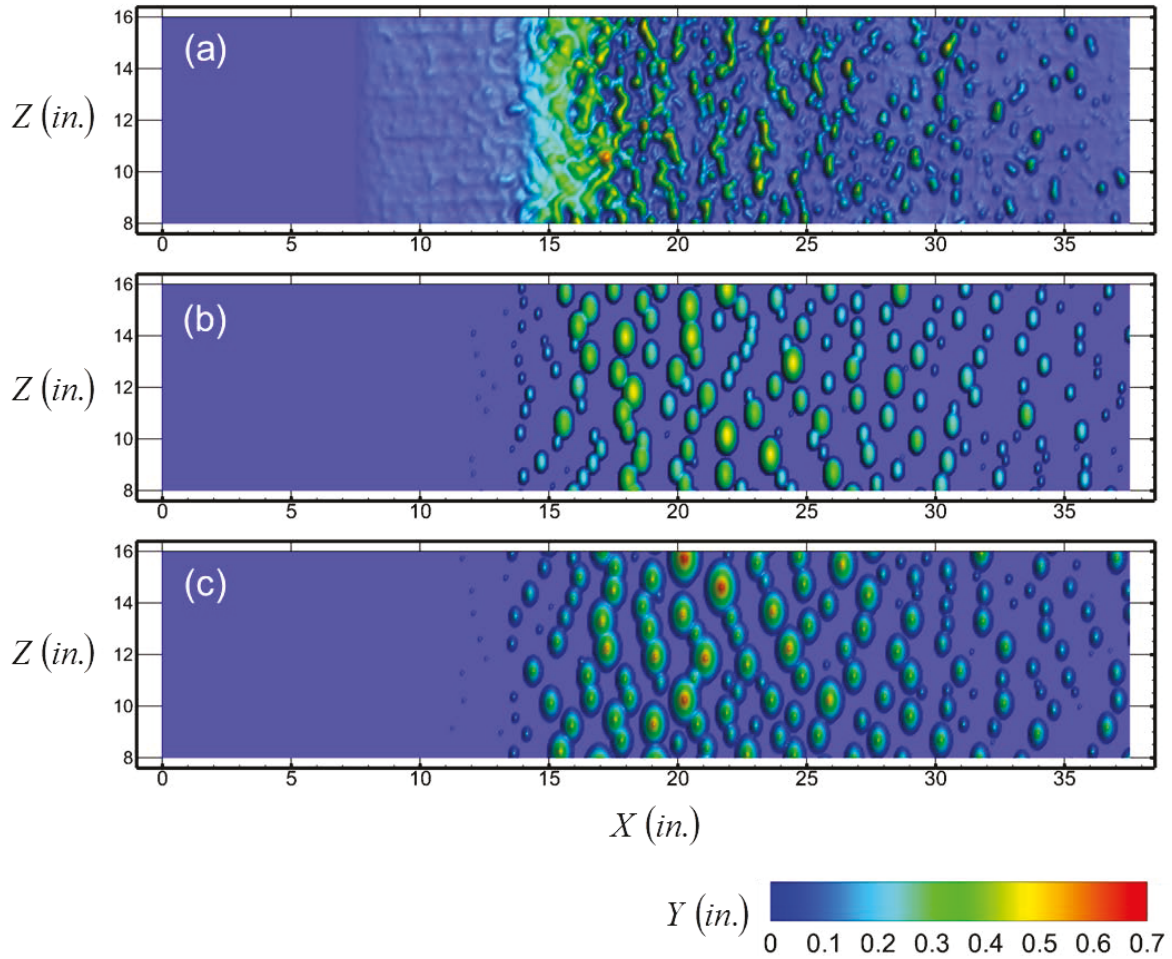


Figure 2.24: Solid models of the heated section of (a) 113012.04 Surface, (b) Ellipsoidal Surface, and (c) Elliptical Cone Surface [12]

Roughness Scaling

Historic and recent ice roughness investigations were performed using the information gathered from 21-in NACA 0012 airfoils at low-speed highly-glazed ice conditions. The recent investigations using laser scans have been important to the understanding of roughness spatial and temporal evolution; however, in order to relate the roughness studies to large commercial aircraft wings and flight, proper scaling of the results is needed.

Reynolds Number Scaling

The Reynolds number, discussed above, can be scaled, which is important for research as full-scale testing can be costly and in some cases impractical. A model can be tested in a wind tunnel and the data can be correlated to the actual flow. Eq. (2.25) shows the calculation necessary to create similar flows over proportional geometries by matching Reynolds numbers.

$$Re = \frac{\rho U_{\infty} x}{\mu} = Re_m = \frac{\rho U_m x_m}{\mu} \quad (2.25)$$

Where the subscript m denotes the model attempting to match Reynolds numbers with the full scale. In the particular case of ice roughness surface experimentation discussed above, the length scale (x) of the airfoil and roughness elements was increased by a factor of ten (x_m) and thus the wind tunnel velocity during heat transfer experimentation was set a factor of ten lower in order to preserve the Reynolds number experienced by a 21-in chord NACA 0012 airfoil.

Scaled Ice Roughness Investigation

A study by McClain et al. [55] characterized the roughness of 72-in and 21-in airfoils in icing conditions in the IRT to investigate the similarities of ice roughness created on the different sized airfoils. While the Reynolds number is a significant parameter when discussing ice shape scaling, the stagnation collection efficiency (β_0) and the Weber number (We_L) are the most significant parameters in scaling glaze ice accretions. The Weber number is given by Eq. (2.26) where L is the length scale and σ is the surface tension.

$$We_L = \frac{\rho_w U_\infty^2 L}{\sigma} \quad (2.26)$$

Under a similar set-up as the experiments run by McClain et al. [29], the 72-in and 21-in airfoils were subject to various icing conditions. The tests run on the 72-in airfoil are known as the “reference tests” while the tests run on the 21-in airfoil are called the “scaled tests”. The parameters set for the experiments are displayed in Table 2.3.

Table 2.3: Summary of test parameters for roughness scaling parameters [55]

<i>Case Number</i>	<i>Chord (in)</i>	<i>T_{total} (°C)</i>	<i>V (m/s)</i>	<i>MVD (μm)</i>	<i>LWC (gm/m³)</i>	<i>Δt_s (s)</i>	<i>A_c</i>	<i>Re_c·10⁻⁶</i>	<i>β₀</i>	<i>We_d·10⁻⁶</i>
41514.01	72	-4.7	51.5	50	0.75	477.1	0.348	6.68	0.710	2.36
41514.02	72	-5.5	51.5	100	0.75	477.1	0.348	6.68	0.859	2.36
41514.03	72	-5.7	51.5	150	0.75	477.1	0.348	6.68	0.911	2.36
41514.04	72	-5.8	51.5	174	0.75	477.1	0.348	6.68	0.925	2.36
32814.05	21	-2.9	95.3	18.2	0.90	62.6	0.348	3.61	0.710	2.36
32814.02	21	-4.0	95.3	35.8	1.00	56.4	0.348	3.61	0.859	2.36
32814.03	21	-2.3	95.3	53.2	0.58	97.2	0.348	3.61	0.911	2.36
32814.04	21	-2.7	95.3	61.5	0.65	86.7	0.348	3.61	0.925	2.36

Shown in Table 2.3, the parameters varied between the four reference tests were the MVD and the resulting stagnation collection efficiency (β_0). For the scaled tests, the accretion time (Δt_s) and the MVD were varied to match the Weber number (We_d) where the length scale, L , for this case was twice the leading-edge radius, A_c is the accumulation parameter, and β_0 is the stagnation point collection efficiency for each condition of the reference test.

The resulting ice roughness accreted on the airfoils tested were scanned with a ROMER Absolute Arm as discussed in the above section. The laser scanned data was

evaluated using the SOM approach of Kreeger and McClain [31] in the same way as the real ice roughness described above.

Figure 2.25 shows a comparison of the 041514.01 reference point cloud and its corresponding scaled point cloud, run 032814.05. As shown in Table 2.3, the two runs match in Weber number, stagnation point collection efficiency, freezing fraction, and accumulation parameter. It should be noted that the color maps of the two point clouds have different ranges. It can be observed that the roughness elements on the 041514.01 case are taller and have wider bases than on the 032814.05 case.

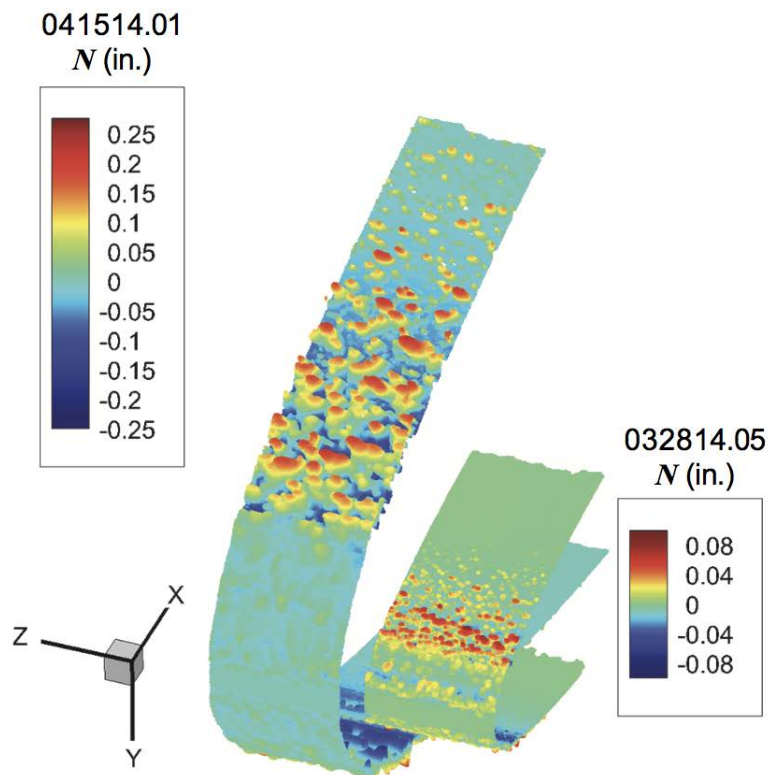


Figure 2.25: Comparison of 041514.01 and 032814.05 point clouds [55]

Figure 2.26 presents the variations in RMS roughness at each SOM codebook vector plotted against the surface distance along the airfoil for (a) the reference and (b)

scaled airfoil cases. Figure 2.27 shows the average ice thickness at each codebook vector against the surface distance along the airfoil for (a) the reference and (b) the scaled airfoil cases. These two figures show the variation of the ice roughness height and ice thickness corresponding to the varying stagnation point collection efficiencies. There are 3 distinct regions in all of the roughness profiles: 1) the smooth stagnation point, 2) a region of ice roughness elements on an ice plateau, and 3) a region of peak roughness elements downstream of the ice plateau and the slow decay in heights downstream of the peak roughness heights. While all of the airfoils exhibit these regions, it can be seen that the 21-in airfoils have larger isolated elements on the ice plateau (relative to the roughness height maximum).

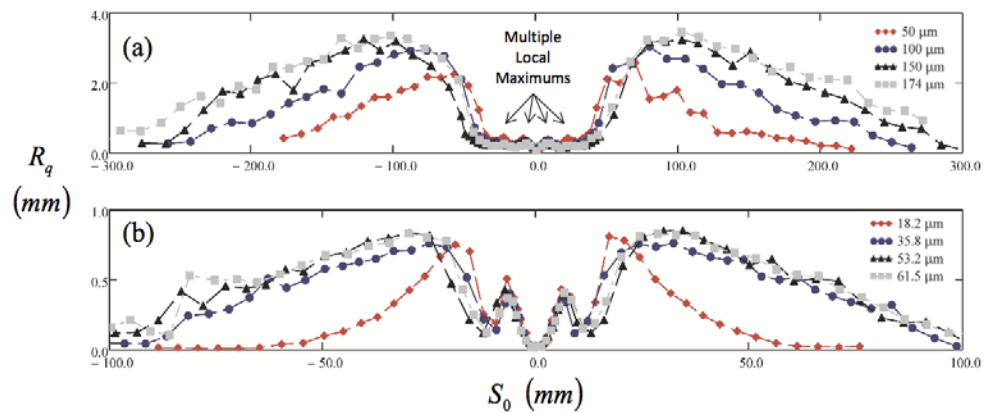


Figure 2.26: Measured RMS roughness heights along the surface of airfoils (a) reference conditions with 72-in chord and (b) scaled conditions with 21-in chord [55]

To study the geometric similarities between the airfoils tested, Figure 2.28 presents the relative roughness height variations along the surfaces of the airfoils tested. Either leading-edge radius or airfoil chord can be used to normalize the roughness heights. In this study, the airfoil chord is used to scale the roughness and the airfoil surface distance. Observed in Figure 2.27 is that for each different value of the stagnation

collection efficiency, the relative roughness of both the scaled and reference conditions match quite well with the exception of the roughness elements on the surface of the glaze ice plateau.

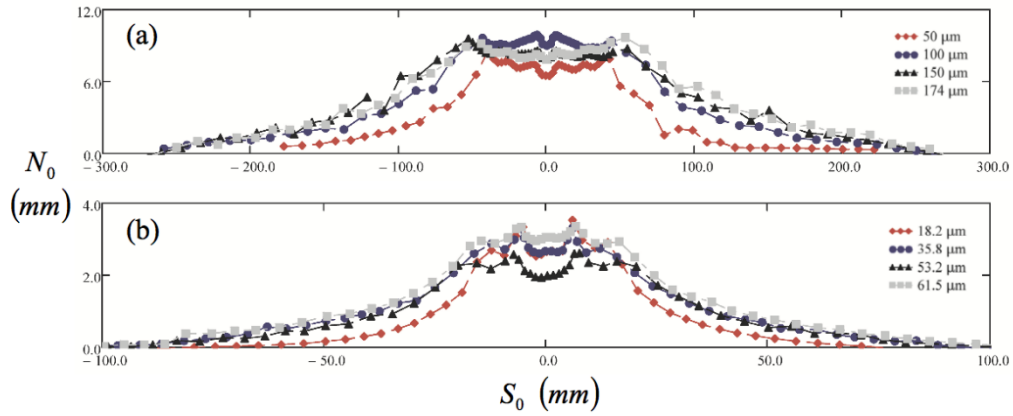


Figure 2.27: Measured ice thickness along the surface of airfoils (a) reference conditions with 72-in chord and (b) scaled conditions with 21-in chord [55]

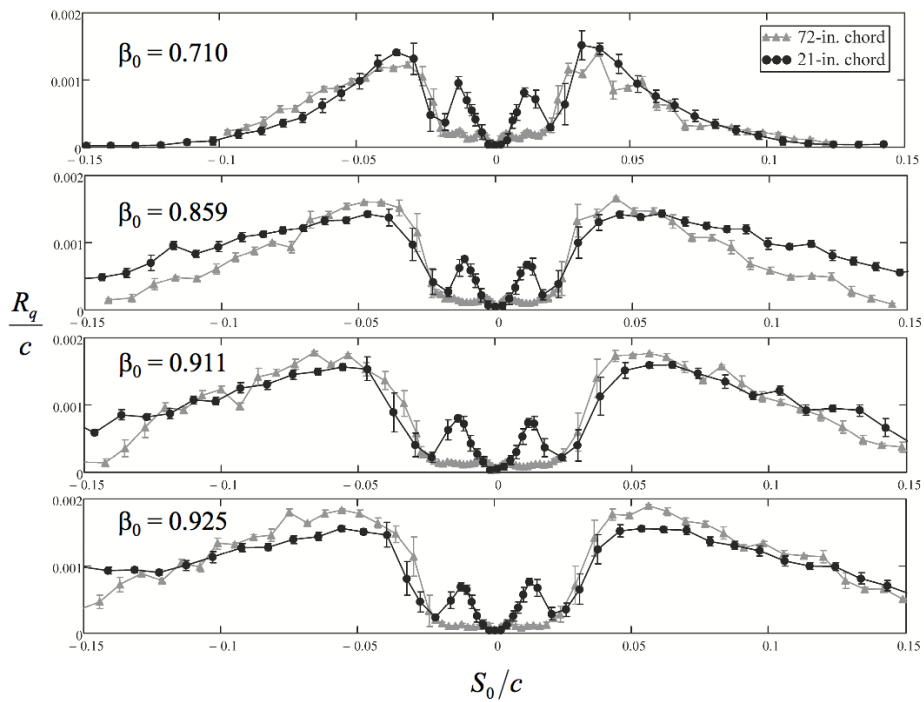


Figure 2.28: Roughness versus surface distance scaled by airfoil chord grouped by collection efficiency [55]

Figure 2.29 presents the relative ice thickness variations versus the scaled surface distance from the stagnation point. Similar to Figure 2.28, the data is grouped by the local stagnation collection efficiency. As expected, the biggest differences between the relative thickness occurs in the glaze ice plateau region. Beyond the plateau the data matches very well.

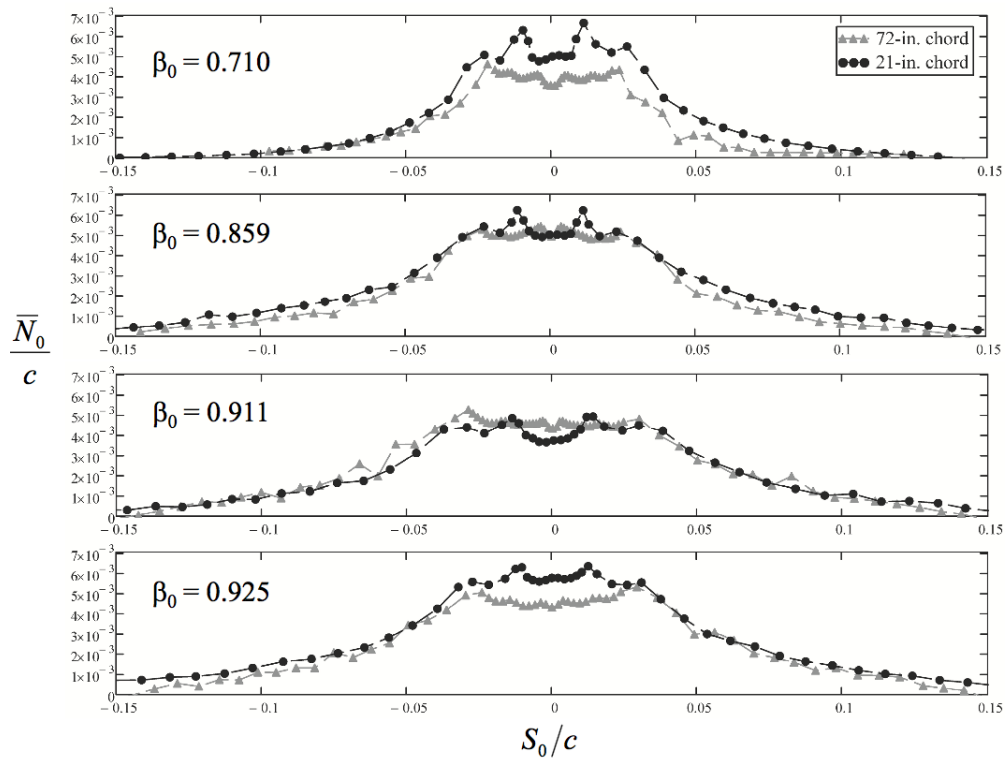


Figure 2.29: Ice thickness versus surface distance scaled by airfoil chord grouped by collection efficiency [55]

While the results from the above Figures 2.28 and 2.29 show a geometric scaling of ice roughness and thickness between a 72-in and 21-in NACA 0012 airfoil, a method to collapse all of the data from the reference and scaled tests was performed by McClain et al. [55]. For a detailed description refer to McClain, Vargas, and Tsao [55], a cursory description of the results will be given for the purpose of this paper.

The data from McClain et al. [55] was plotted against a new parameter that calculated the actual collection efficiency at a certain point along the surface of the airfoil. For an airfoil at zero angle of attack the local collection efficiency is estimated by Eq. (2.27).

$$\beta_s \approx \beta_0 \cos(\alpha + \gamma_s) \quad (2.27)$$

Where α and γ_s are the angles defined on Figure 2.30.

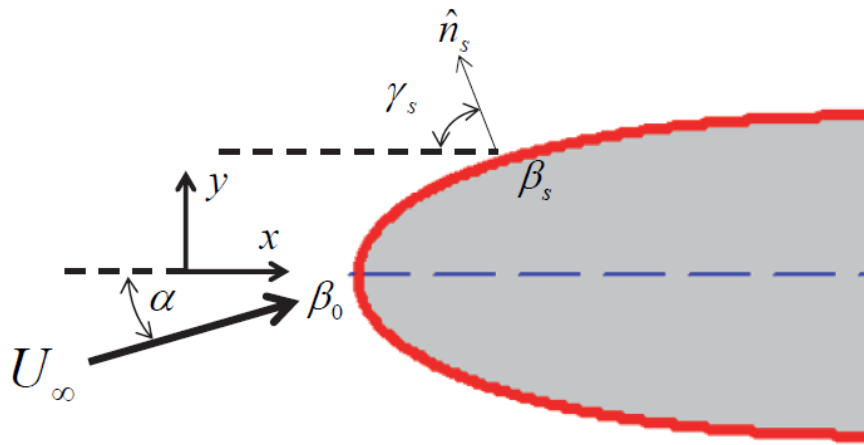


Figure 2.30: Geometric evaluation of local collection efficiency [55]

Figure 2.31 shows the maximum roughness variations (scaled by the theoretical rime-ice stagnation point thickness, $N_{0,R}$) versus the estimated local collection efficiency. The relative roughness height values are expected to correlate with the local collection efficiency, in Rime ice conditions. While there is some scatter in the collapsed data, there appear to be two discrete regions: 1) the glaze ice plateau where the data is not correlated to the local collection efficiency and 2) the region downstream of the glaze ice plateau where the scaled roughness data correlates with the local collection efficiency. Just downstream of the ice plateau the maximum roughness increases to a maximum and then decays. These two regions give valuable insight on the physics that are dominant. The

glaze ice plateau is dominated by the behavior of the liquid film rather than the droplet collection, whereas downstream of the plateau (the location where the liquid film breakdown occurs) droplet collection physics control the ice accumulation on the surface.

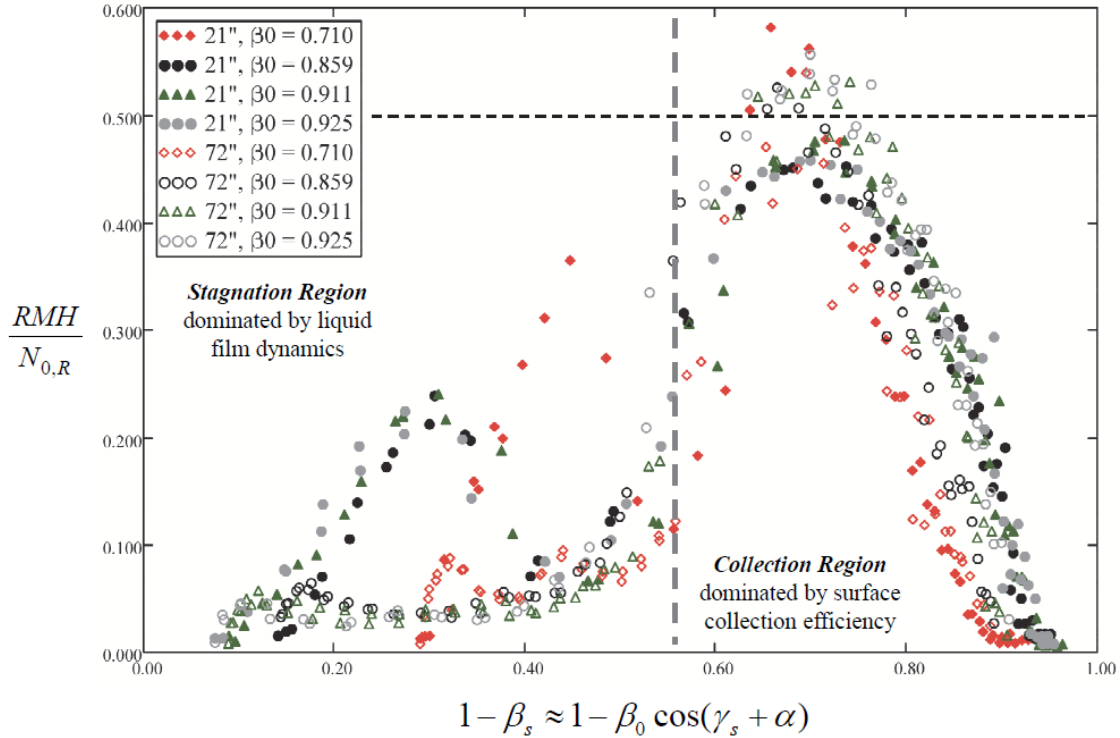


Figure 2.31: Scaled maximum roughness against local collection efficiency (β_s) [55]

The significant findings with regard to the study from the investigation of McClain et al. [55] are that the relative roughness in the collection region of a 21-in and a 72-in NACA 0012 airfoil, based on matching Weber number and stagnation collection efficiency, scales geometrically.

In regard to the current study, an attempt to match several parameters was made in order to properly scale testing. Figure 2.32 shows a small and large airfoil with the parameters important to scaling.

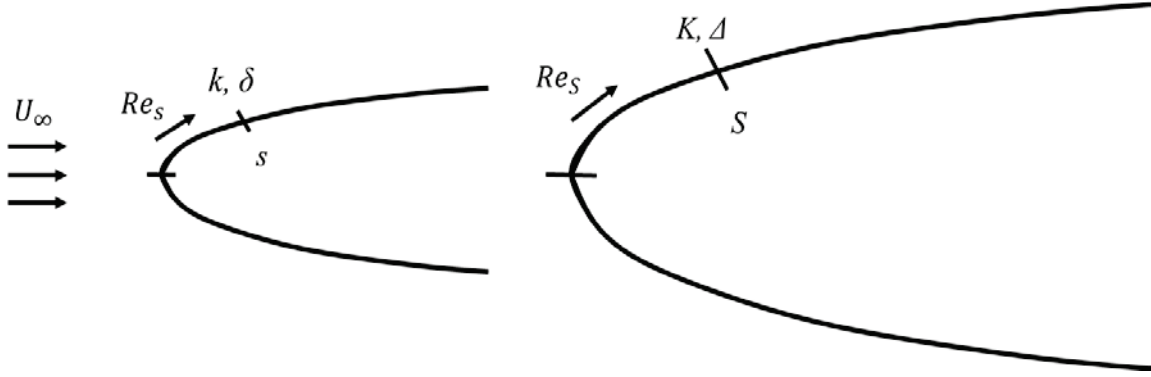


Figure 2.32: Scaling parameters used for experimentation

Where S and s are the distance along the airfoil surface, δ and Δ represent the boundary layer thickness, and k and K are the mean roughness heights. Using the assumption that the roughness scales geometrically from above, the mean roughness heights scaled by surface distance is equal between the full size airfoil and the model used for testing is shown by Eq. (2.28).

$$\frac{k}{s} = \frac{K}{S} \quad (2.28)$$

Eqs (2.29) and (2.30) are known from boundary layer scale analysis

$$\frac{\delta}{s} \sim Re_s^{-\frac{1}{2}} \quad (2.29)$$

$$\frac{\Delta}{S} \sim Re_S^{-\frac{1}{2}} \quad (2.30)$$

By combining Eqs. (2.28)-(2.30) it is determined that the roughness heights of the model and full size airfoils, scaled by the respective boundary layer heights, are equal and is shown by Eq. (2.31)

$$\frac{k}{\delta} = \frac{K}{\Delta} \quad (2.31)$$

From Eq. (2.31) the Reynolds number experienced by the model can be matched to that of the full size airfoil by using Eq. (2.32). This equation shows edge velocity (u_e and U_e) and the length scales (s and S) between the model and full size airfoil are directly proportional.

$$u_e s \sim U_e S \quad (2.32)$$

In this experiment the length scale was raised by a factor of ten from the full size model so the wind tunnel velocity can be scaled down by a factor of ten. It is also noted that the velocity variation along the full size airfoil is matched using a ceiling insert. This ceiling insert is discussed in detail in Chapter Three.

The objective of this study is to build on the works of Shannon [8], Hawkins [10], McCarrell [11], and Clemenson [12] by characterizing the heat transfer enhancement of real and simulated roughness surfaces experiencing flows similar to those of a larger NACA 0012 airfoil using roughness surfaces previously created. Roughness surfaces previously created on 21-in NACA airfoil can be used because of evidence of roughness scaling discussed above.

CHAPTER THREE

Materials and Methodology

Heat transfer experiments were performed on ten different roughness surfaces to characterize the convective heat transfer in the presence of scaled accelerated flow. Four of the surfaces represent laser-scanned real ice roughness, while the remaining six use geometric shapes as individual elements to represent realistic ice roughness. This chapter discusses the manufacturing of the surfaces as well as the apparatus and procedures used in the experiments. Also discussed in this chapter is the smooth surface boundary layer velocity validation procedure and apparatus. Lastly, this chapter will also outline data reduction and uncertainty analysis used for the convective heat transfer experiments and the boundary layer traces performed.

Roughness Surface Manufacturing

The unwrapped ice roughness surfaces were split up into twelve separate surface panels and converted into STL files using a MATLAB code. The surfaces were also scaled by a factor of 10 for the purpose of Reynolds number scaling, as discussed in Chapter 2. SolidWorks was used to create a solid model from the STL files generated shown in Chapter 2. From these solid models, each panel section was created using a Dimension 768 SST 3D printer. The first panels of each column on all surfaces, representing the region close to the stagnation point, were smooth due to the neglected roughness on the glazed plateau previously discussed. These panels were not reprinted for each case and were used as the control. The nine sections of the surface with

roughness were printed using ABS plastic. The middle columns for each surface, the heated section, were also manufactured in a CNC machine using 6061 aluminum. The back of each surface panel along the heated section was fastened with 1/16" of neoprene gasket, this neoprene gasket served as a means for even contact between the surface panel and the Mylar film heaters. For the purpose of matching height, the rest of the panels were fitted with the neoprene gasket as well. To ensure the heated section had a known emissivity, the panels were painted a matte black, emissivity of 0.95. Shown in Figure 3.1 and 3.2 are the unpainted aluminum heated section and the full plastic roughness surface manufactured for the 113012.04 case.



Figure 3.1: Unpainted aluminum heated section for 113012.04 Case [10]



Figure 3.2: Full Plastic Manufactured Unwrapped Surface for 113012.04 Case [10]

Instrumented Test Plate

The plate on which the surfaces will be tested, designed to model the experiments of Anderson et al. [36], represents the leading 17.1% (3.6-in) region on a NACA 0012 airfoil immediately downstream of the stagnation point. This region of interest was determined to be where ice accretion is most predominant. For the purpose of testing, the 3.6-in region was scaled by a factor of 10 to create a 36-in long test plate. Due to this geometric scale, the Reynolds number during testing is reduced by a factor of 10 to emulate the actual Reynolds number of the airfoil.

For a basic understanding of the experiments performed in this paper, an explanation of the construction of the test plate by Tecson [6] will be provided below. For a detailed and complete account, refer to Tecson [6]. The test plate was designed to house 25 substitutable surface panels. This eliminates the need for creating a new test plate for each desired test surface. Figure 3.3 shows a solid model of the test plate. The test plate is composed of four main subsystems listed below. These subsystems will be discussed in greater detail in the following sections: Plexiglas sub-plate, instrumentation and wiring, Mylar film heaters, and aerodynamic features

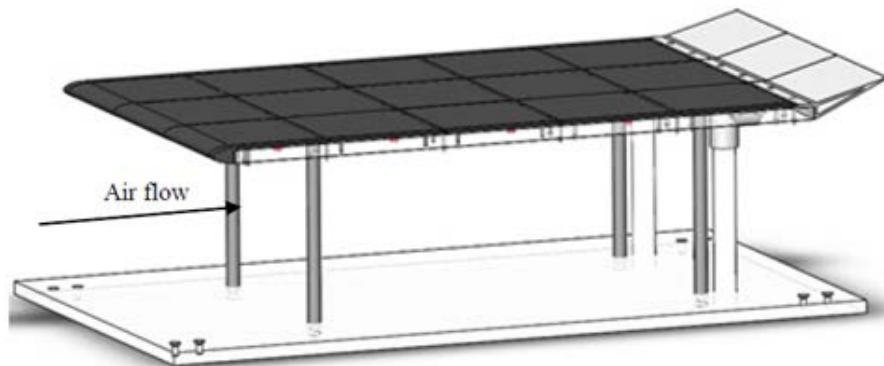


Figure 3.3: Solid Model of the Test Plate [6]

Plexiglas Sub-Plate

A base plate made from Plexiglas was used to house the interchangeable surface panels and measures 24-in x 36-in x 0.75-in. The width and height were chosen for the 36-in long test region and to fit in the 24-in wide wind tunnel test section. The depth was chosen in order to allow copper electrodes to be placed into the plate and still remain flush with the surface. Additionally, 1/8-in channels were machined out in order to house thermocouples just below the test surface along with off-center through channels for the wiring of the thermocouples. Fifty-two through-holes were drilled into the test plate which were used alongside #4 1.25-in long bolts and #4 nuts to fasten the surface panels to the sub-plate. Additionally, four steel legs, 0.75-in diameter, attach the sub-plate to the wind tunnel floor.

Instrumentation and Wiring

Used to monitor subsurface temperatures, eight Type K thermocouples were imbedded into the machined channels using a plastic epoxy. The thermocouples were positioned along the downstream centerline of the plate. Five thermocouples were placed at the center of each of the heated sections. Two additional thermocouples were added to the first section from the leading edge and one additional thermocouple was added to the second section. These extra thermocouples are used to determine the heat loss gradients in the downstream direction. Eight self-adhesive Type K thermocouples were attached to the bottom of the Plexiglas plate at the same locations as the embedded thermocouples. These thermocouple pairs were used to calculate the heat loss through the bottom of the test plate. Figure 3.4 shows a side view of the test plate along with the locations of the 16

thermocouples. The thermocouple pairs were named according to the heated sections, with letter designations added to denote sections with multiple thermocouple pairs.

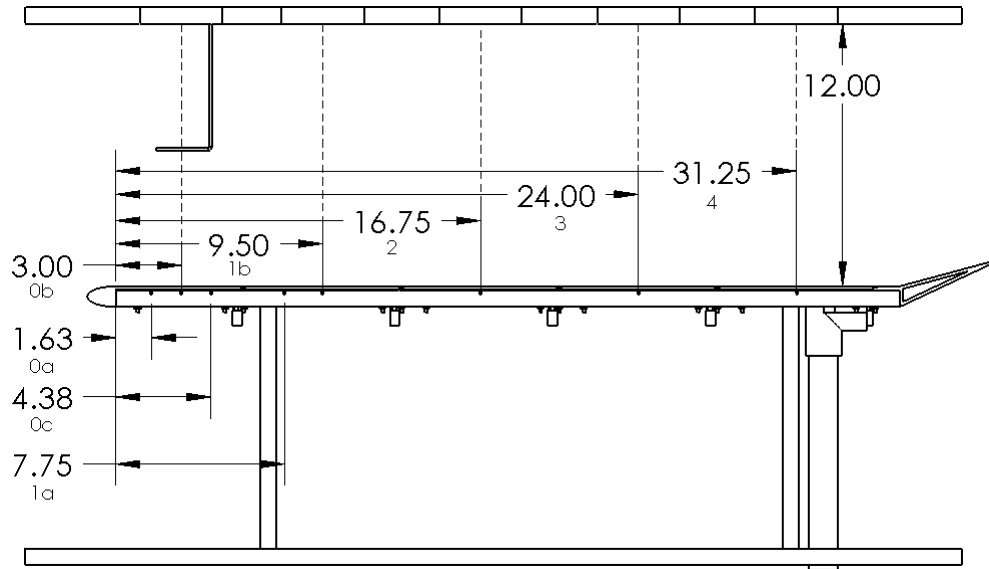


Figure 3.4: Side view of test plate showing thermocouple locations relative to the leading edge (dimensions in inches, flow direction is left to right) [6]

To supply power to the Mylar heaters, fourteen gauge copper wire was connected to terminal ports on each of the copper electrodes. Twenty-two gauge copper wire was connected to each terminal port to measure voltage supplied to each heater. The wires were grouped and routed through the bottom of the test plate into an electrical junction box, which runs the wires through the wind tunnel floor and allows for accessing of the wires outside of the test section.

Mylar Film Heaters

Each heated section contains a gold-deposited Mylar film heater that provides a nominally constant flux boundary condition. The heaters span the distance between the copper electrodes in the Plexiglas sub-plate. A conductive silver paint was applied to

reduce contact resistance between the heaters and the electrodes. Figure 3.5 shows a top view of the Plexiglas sub-plate, the shaded regions designate the Mylar heater locations.

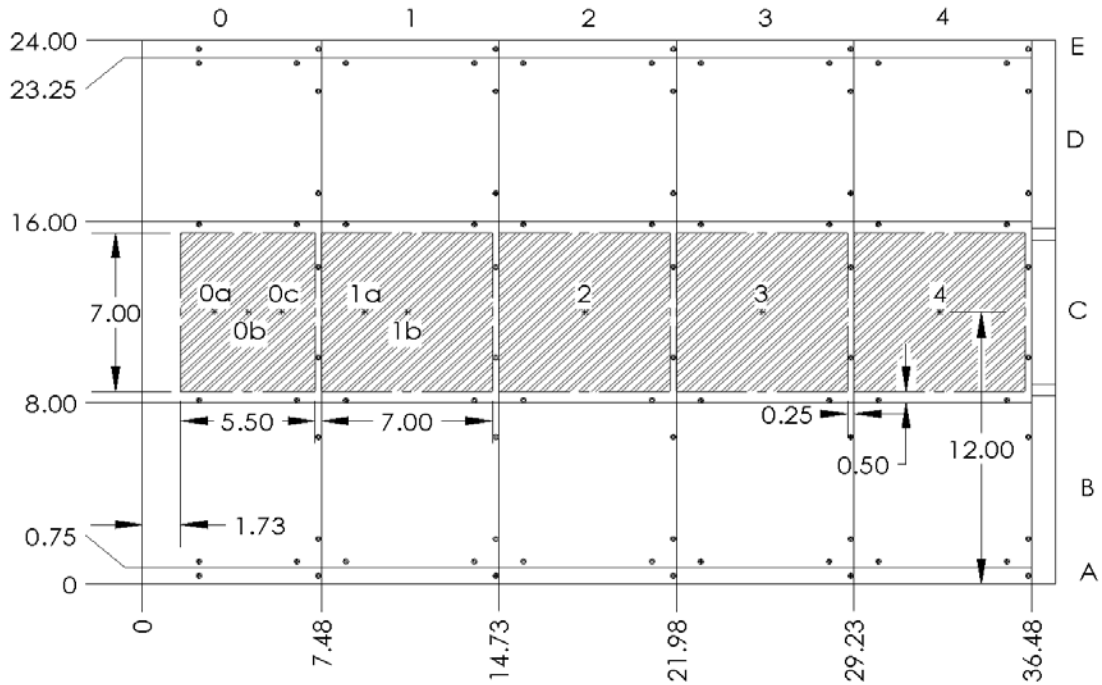


Figure 3.5: Top view of Plexiglas sub-plate showing heated sections (dimensions in inches, flow direction is left to right) [6]

When installing the heater it was imperative to avoid contact of skin oils or other contaminants with the gold layer. A compromised gold layer could lead to uneven heating. The heaters were applied to the sub-plate, gold side down, using a spray adhesive. Excess bubbles and adhesive were removed to keep heating even and protect the longevity of the heater.

Aerodynamic Features

Two distinct aerodynamic features were added to the test plate, a bullnose at the leading edge and a fin at the trailing edge. The bullnose is used at the leading edge to prevent flow separation. The fin at the trailing edge is used to account for the blockage

caused by instrumentation housing and the steel legs. The frontal area of the fin was designed to be equal to the area of the blockage.

Ceiling Insert for Flow Acceleration

Ceiling Insert Design

To imitate the flow acceleration found along a NACA 0012 airfoil at 0° angle of attack Shannon [8] designed a wind tunnel ceiling insert. The goal of the insert design was to match the local Reynolds number variation like in Eq. (3.1).

$$\frac{\rho U_e x}{\mu} \Big|_{Plate} = \frac{\rho U_e s}{\mu} \Big|_{NACA 0012} \quad (3.1)$$

As the flow moves downstream, along the x-direction, from the stagnation point of the test plate, the geometry and velocity are scaled and attempt to match the local Reynolds number of the airfoil based on surface distance, s, from the stagnation point.

The design process began with using a vortex-panel solver to generate the variation in pressure coefficients along the surface of a NACA 0012 airfoil. Because the experiments in this study were performed at low subsonic speeds, compressibility effects are ignored. The results of the vortex panel solver are shown in Figure 3.6, and the region to the left of the green vertical line is the leading 17.1% region of the airfoil which the test plate represents.

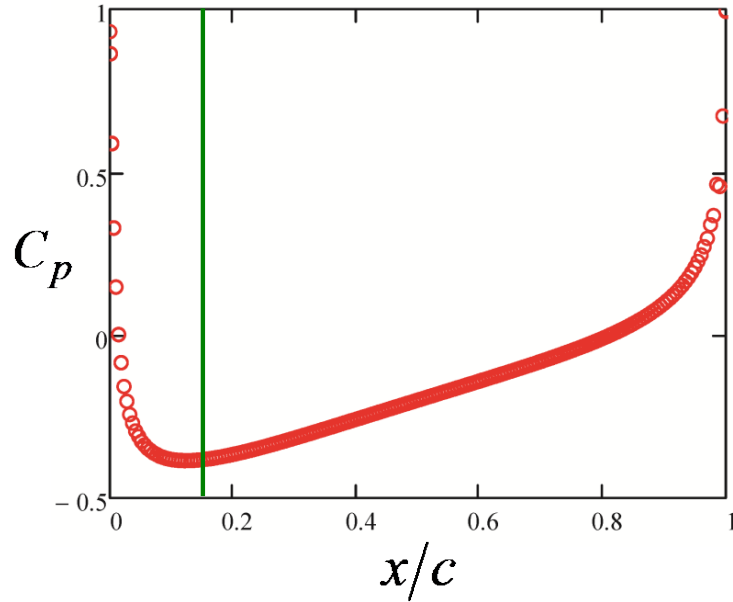


Figure 3.6: Pressure coefficient variation along a low speed NACA 0012 airfoil [8]

Using the pressure coefficients a velocity variation can be calculated using Eq. (3.2), where F_s , the surface geometry scaling factor, is 10 as discussed above.

$$U_e(x) = \frac{U_{\infty,IRT}}{F_s} (1 - C_p)^{1/2} \quad (3.2)$$

Figure 3.7 displays the resulting velocity variation along the airfoil along with the matched design variation. Seen in Figure 3.7, the design variation does not match the airfoil variation in the first 0.02% near the stagnation point. This is a characteristic complication when modeling flow acceleration with a flat plate and an insert, flow stagnation cannot properly be achieved. To deal with the issues in the stagnation region, a “cut-in” velocity of 12 m/s was used, meaning the insert design imparted a velocity of 12 m/s over the bullnose area of the test plate.

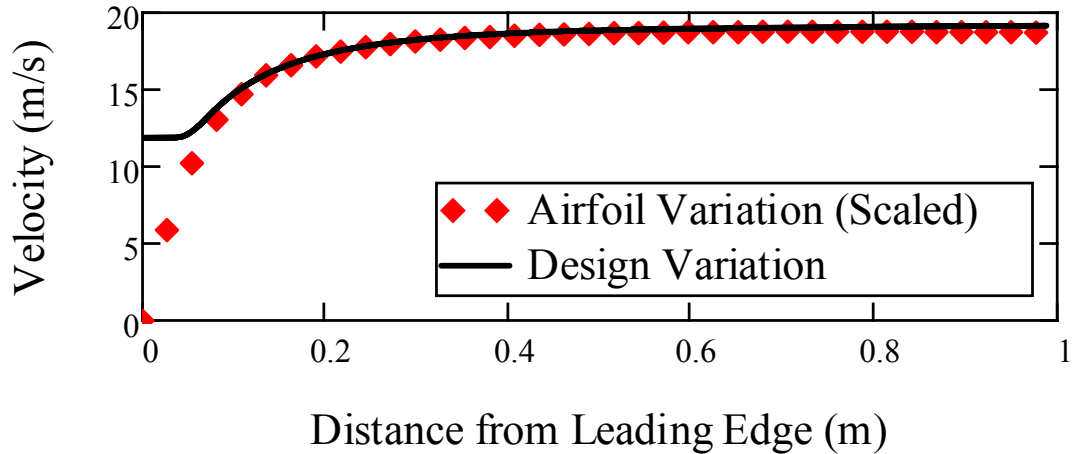


Figure 3.7: Scaled airfoil velocity variation and design velocity variation

The design velocity variation along the test plate was imported into a boundary layer code that calculated momentum thickness growth on the test plate and the ceiling insert in the wind tunnel test section. The resulting thickness profile of the ceiling insert was formulated and the insert was ready for construction.

Ceiling Insert Construction

The ceiling insert was constructed from surfboard foam using a hotwire CNC foam cutter. An area on the top of the foam cut out was removed in order to install a wood mounting plate for proper and consistent attachment to the wind tunnel ceiling. Five cylindrical ports were added to the insert along the centerline of the heated section for proper viewing when taking infrared measurements. To minimize the effect on the flow near the leading edge of the insert, the first viewing port has a smaller diameter than the other ports. Figure 3.8 shows a solid model of the ceiling insert.

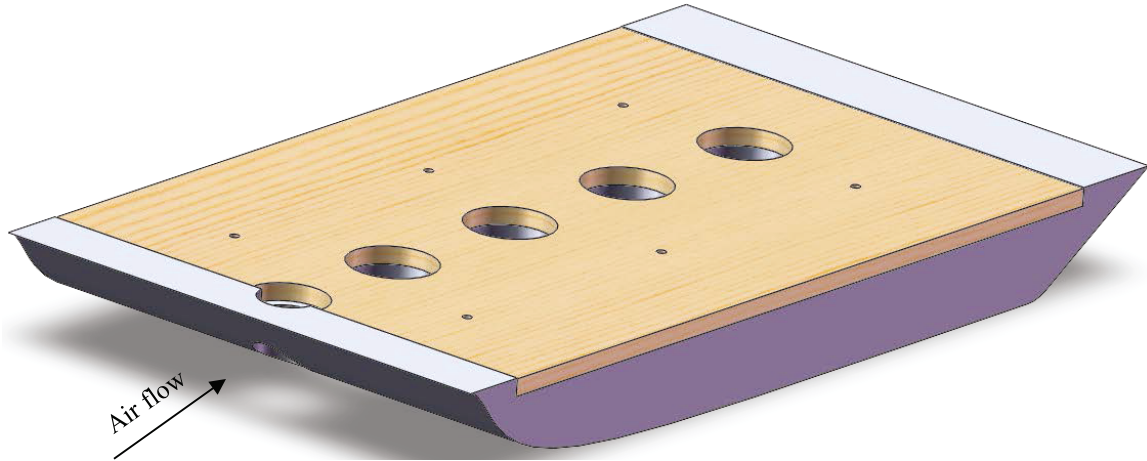


Figure 3.8: Solid model of the ceiling insert [8]

Experimental Setup and Procedure

The testing was performed in the Baylor University Subsonic Wind Tunnel (BIG BLUE), manufactured by Engineering Laboratory Design, Inc., Model 406B. The BUSWT uses a 40 horsepower, variable speed electric motor that drives a constant pitch fan capable of producing airflows ranging from 0.1 m/s to 50 m/s with a velocity variation of less than $\pm 1\%$. Three high-porosity screens and the honeycomb inlet provide an inlet turbulence of 0.2%. The test section of the wind tunnel has a cross sectional area of 24-in by 24-in with a length of 48-in in the flow direction.

For the ten surfaces discussed above, steady-state heat transfer coefficient measurement experiments were performed. Also performed in the BUSWT were hot-wire velocity boundary layer traces for velocity validation. Figure 3.9 shows a sketch of the experimental setup used for experimentation. The procedures and experiments used in this study are outlined in the following sections.

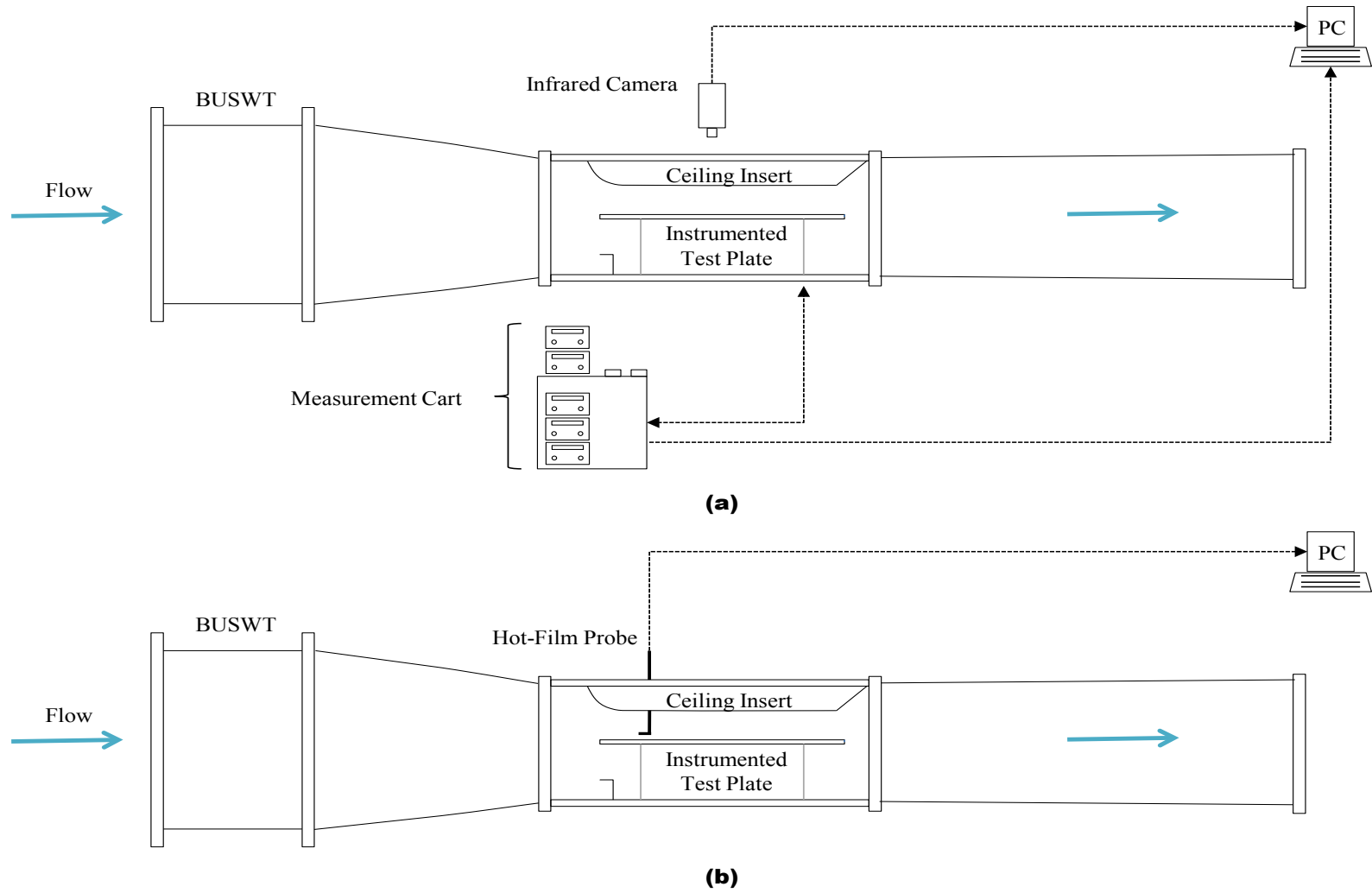


Figure 3.9: Side view of experimental setups for (a) the convection tests and (b) velocity boundary layer tests (not to scale) [8]

Convection Measurements

A FLIR SC4000 ThermoVision IR camera with a 25-mm lens was used to make temperature measurements. This camera has an indium-antimonide (InSb) detector that generates a 320 by 256 pixel image of temperature on a surface. The images taken by the camera were 6.4-in in the flow direction and 5.12-in spanwise. The data from the images were collected using FLIR ExmaminIR software. To capture the images, five viewing ports were installed into the wind tunnel ceiling and fitted with FLIR IRW-3C calcium-fluoride windows. The windows were positioned at a 30° angle to prevent reflections interfering with the IR camera. The IR camera was mounted on a one-dimensional Velmex BiSlide traversing system which positioned the camera above each of the viewing windows. Figure 3.10 shows the test section with the traversing system, IR camera mounted, and the infrared viewing windows.

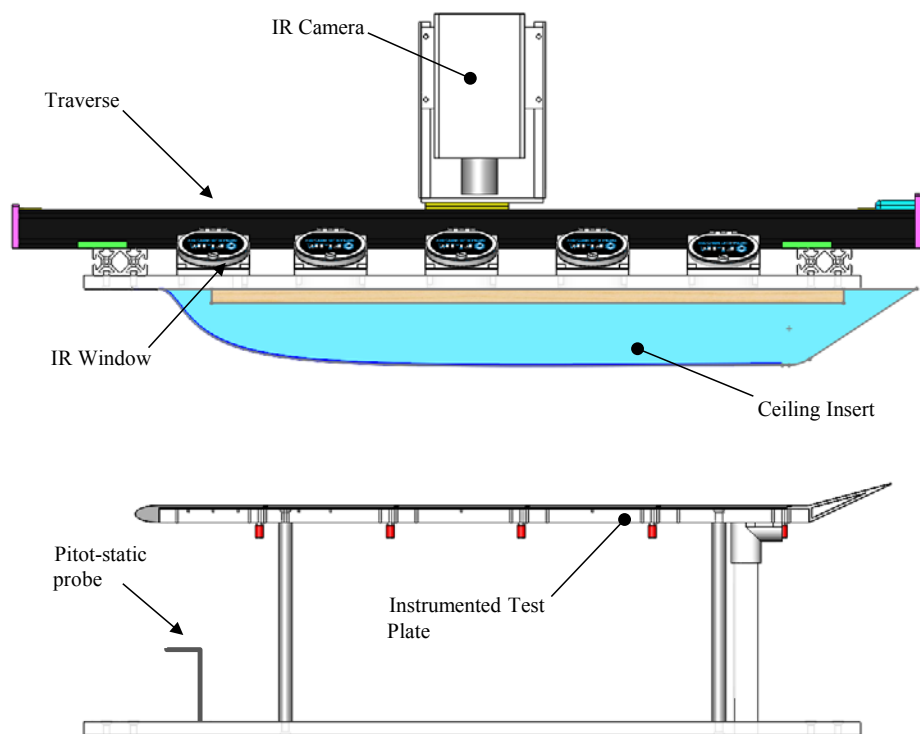


Figure 3.10: Side view of test section during convective heat transfer testing [8]

A 6-in pitot-static probe connected to an Omega PCL-2A pressure transducer with a PCL MA-01 WC pressure module was installed on the bottom of the test section to monitor the freestream velocity. Attached to the pitot-static probe was a Type K thermocouple used to monitor the freestream temperature. A zSeries-THBP-LCD atmospheric condition monitor outside of the test section was used to measure the ambient temperature, pressure, and relative humidity during the tests. To ensure that the correct freestream velocity was achieved over the top of the surface, a calibration procedure was used. The wind tunnel velocity was set based on the reading from the PCL-2A to ensure repeatability between the tests.

The following list of required equipment was added to a modified wooden cart by Tecson [6] for completion of convective heat transfer testing:

1. Five BK Precision power supplies to deliver power to each of the Mylar film heaters.
2. NI 9929 DAQ Module to measure and monitor the voltage across heaters in sections zero to three.
3. Three Powertek CTH/10A/TH/24Vdc Type 1 current transducers to measure and monitor the current through heated sections one through three.
4. One Powertek CTH/20A/TH/24Vdc Type 1 current transducers to measure and monitor the current through heated section zero.
5. Two Newport TrueRMS HHM290/N Supermeters to measure and monitor the voltage and current through heated section four. (Used due to equipment availability)

6. NI 9205 DAQ Module to read the outputs from the current transducers zero to three.
7. Five NI 9211 DAQ modules used to record and monitor the outputs of the eight thermocouple pairs in the test plate and the one thermocouple monitoring the freestream temperature.
8. Two NI cDAQ-9172 chassis used to house the seven DAQ modules discussed above.

Outputs from each of the DAQ modules were read into a LabVIEW software Virtual Instrument. Figure 3.11 shows a picture of the modified wood cart with listed equipment. A diagram of the wiring for heated sections is shown in Figure 3.12.

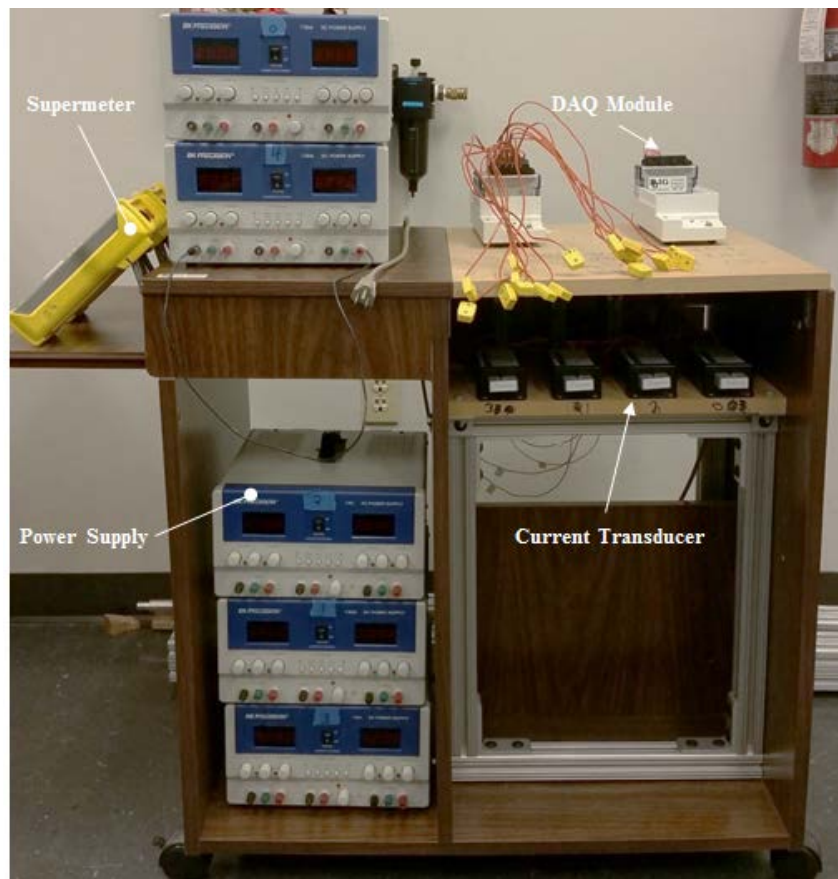


Figure 3.11: Modified wood cart with equipment used in experimentation [8]

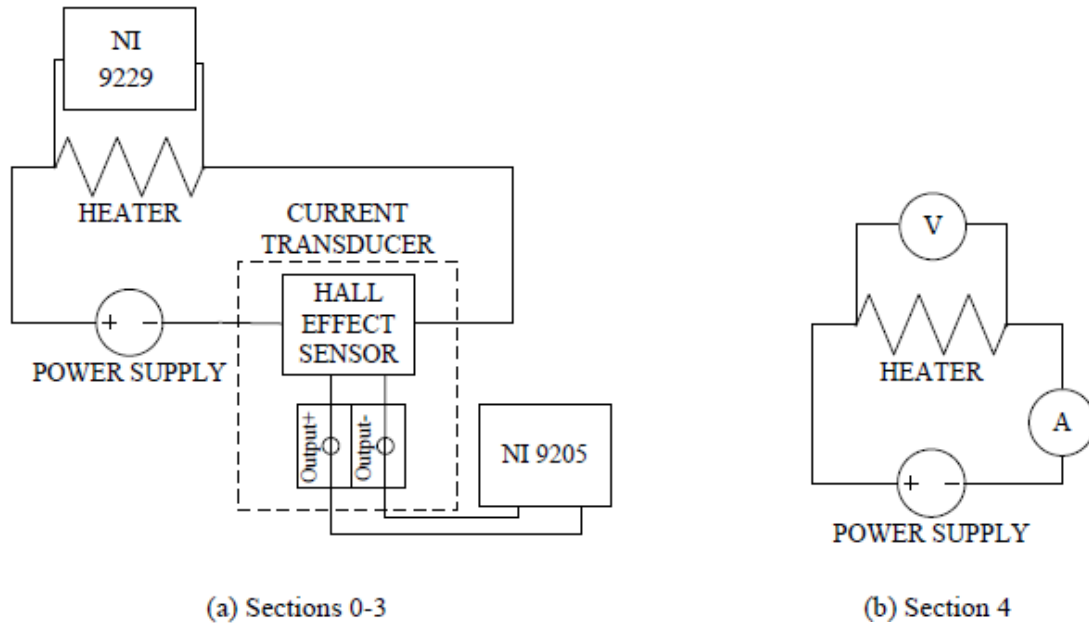


Figure 3.12: Wiring diagram for each heated section [8]

The day prior to testing, some procedures were performed to set-up for the experiment. The surface panels for desired testing were attached to the test plate and the plate was installed into the test section via affixing the wind tunnel test section floor. The pitot-static probe was inserted and attached to the test section floor. The modified rolling cart was placed below the test section, and the equipment was connected to the test plate instrumentation. The monitoring LabVIEW program was run to ensure proper connections to thermocouples and heaters were achieved. The IR camera was turned on and was properly focused, then the camera and test section were covered by a large black felt sheet to reduce light pollution and radiation interference. The test section is left uninterrupted overnight to ensure the temperature of the test plate reaches equilibrium with the ambient room temperature. After the test section sat overnight, the following procedures were performed on test day:

1. The IR camera power was connected, turned on, and left untouched for fifteen minutes to allow the camera's detector to reach proper operating temperature.
2. The PCL-2A pressure transducer, traverse system, DAQ modules, and current transducers were powered on. The PCL-2A was zeroed.
3. Two LabVIEW VI's were started. The first VI was used to read the DAQ, zSeries, and PCL-2A measurements. The second program was used to control the traverse system and position the IR camera.
4. Once the thermocouple readings in were steady state after power up, ExamInIR software was opened and the camera was connected. The IR recording settings were set to seventy frames at a rate of seven frames per second. Calibration images were taken at each of the five heated sections.
5. The PCL-2A was zeroed again and the wind tunnel was started. The velocity through the test section was set according to the pitot-static probe and PCL-2A reading of 0.765 inH₂O in dynamic pressure.
6. The five power sources were turned on and set to provide a flux of 500 W/m² to each of the heated sections.
7. Using the thermocouple readings monitored on the LabVIEW front panel, steady state was reached. This usually took close to two hours.
8. The IR camera was used to record steady state images at each of the five heated sections. Again the IR recording settings were set to seventy frames at a rate of seven frames per second.
9. Upon the capture of the heated section four images, the voltage and current measurements read on the Supermeters were manually recorded.

10. Upon completion of the steady state images, the LabVIEW program was stopped and the equipment was powered down, beginning with the power supplies.

Velocity Validation Measurements

To validate the scaled flow over the test plate surface, velocity boundary layer measurements were taken at the center of each heated section on flat surface panels with a leading edge 2-mm square trip. This trip induced transition to turbulent flow. The PCL-2A, Pitot-static probe, and zSeries conditions monitor discussed above were used. The ceiling from the convection tests was modified to house a Velmex two-dimensional traversing system which allowed movement in the vertical (z) direction. A model 1246-20 X-Array hot-film probe was used for velocity measurements and was powered by a TSI Inc. IFA300 constant temperature anemometry system.

Prior to velocity measurements, the X-Array hot-film probe required calibration. A clean test section (no test plate or ceiling insert) is required for proper calibration. The probe was mounted to a Velmex B487TS rotary table and was placed in the wind tunnel at the same height as the Pitot-static probe. A velocity sweep from 0 to 30-m/s was performed at 10° increments over a range of $\pm 20^\circ$. At each angle and velocity, the wire voltages of each wire on the probe were recorded using an NI 9223 DAQ module in an NI cDAQ-9178 chassis.

For the velocity validation measurements the wind tunnel velocity was set using the same procedure as the convective heat transfer tests discussed above. A LabVIEW program was used to take a velocity boundary layer trace at 101 stations spanning 6-in above the flat plate (the stations were geometrically expanded on a grid with an expansion factor of 1.07). Again, an NI 9223 DAQ module in an NI cDAQ-9178 chassis

was used to acquire the hot-wire trace data. Each station was sampled at a rate of 200,000-Hz, and 300,000 samples were taken from each wire.

Data Reduction and Uncertainty

Convection Data Reduction Equation

To track the heat transfer in the test section during testing, a one dimensional energy balance was implemented. Four modes of heat transfer were considered during the data reduction process, heat added to the test section via the Mylar heaters (Q_{GEN}), heat losses through the Plexiglas test plate (Q_{HL}), heat loss due to radiation (Q_{RAD}), and heat convected from the surface (Q_{CONV}). These four heat transfer modes are illustrated in Figure 3.13.

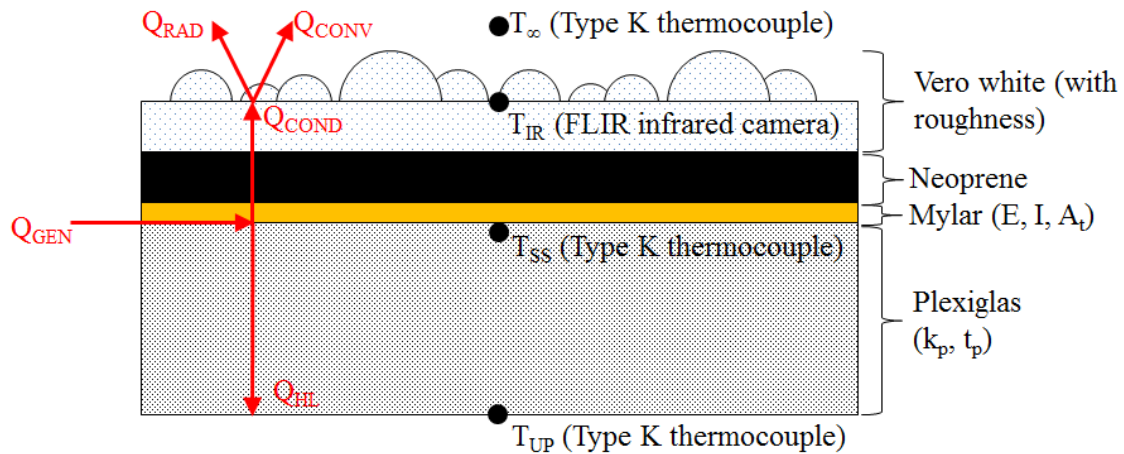


Figure 3.13: Heated section heat transfer schematic (not to scale) [6]

The one dimensional heat balance results in Eq. (3.3).

$$Q_{GEN} = Q_{HL} + Q_{RAD} + Q_{CONV} \quad (3.3)$$

To solve for the heat transfer coefficient, the terms of Eq. (3.3) were broken down further and are explained in the following paragraphs.

The generation term, heat added to the plate via the Mylar heaters, is defined by Eq. (3.4) using Ohm's law on a per pixel basis. E is the voltage across the heater, I is the current through the heaters, A_{pix} is the individual pixel area, and A_t is the total area of the heater.

$$Q_{GEN} = EI \frac{A_{pix}}{A_t} \quad (3.4)$$

The heat loss, conduction through the Plexiglas sub-plate, is modeled by Fourier's Law of conduction. Given by Eq. (3.5) is the conductive heat loss on a per pixel basis. C_k is the conduction parameter, k_p is the thermal conductivity of the Plexiglas, T_{SS} is the is the temperature of the Plexiglas measured by the subsurface thermocouples, T_{UP} is the temperature on the underside of the Plexiglas sub-plate, and t_p is the thickness of the Plexiglas sub-plate.

$$Q_{HL} = C_k \frac{k_p A_{pix} (T_{SS} - T_{UP})}{t_p} \quad (3.5)$$

The losses due to radiation from the surface are calculated by Eq. (3.6) using Stefan-Boltzmann's law of radiation. In this equation ε is the known surface emissivity, σ is the Stefan-Boltzmann constant, T_{IR} is the surface temperature as measured by the IR camera, and T_∞ is the freestream temperature measured by the thermocouple at the pitot-static probe.

$$Q_{RAD} = \varepsilon \sigma A_{pix} (T_{IR}^4 - T_\infty^4) \quad (3.6)$$

Governing the convection term is Newton's law of cooling. Eq. (3.7) gives the term calculation on a per pixel basis where h is the heat transfer coefficient.

$$Q_{CONV} = hA_{pix}(T_{IR} - T_{\infty}) \quad (3.7)$$

By substituting Eqs. (3.4) - (3.7) into Eq. (3.3) a term for the heat transfer coefficient on a per pixel basis is given by Eq. (3.8).

$$h = \frac{\frac{EI}{A_t} - C_k \frac{k_p(T_{SS} - T_{UP})}{t_p} - \varepsilon\sigma(T_{IR}^4 - T_{\infty}^4)}{T_{IR} - T_{\infty}} \quad (3.8)$$

During the derivation of Eq. (3.8) three important assumptions were made. First the conduction in the spanwise direction is negligible, second the Mylar film heaters do generate a uniform heat flux to the test surface, and lastly the heat loss through each of the sections is constant and can be measured by the thermocouple at the center of the section.

When validating the instrumented test plate, Walker [7] found that the heat transfer coefficients calculated from a smooth-laminar and a smooth-turbulent experiment failed to match the accepted values using theoretical correlations. Upon further observation, Walker [7] discovered that the thermal connectivity of the Plexiglas sub-plate was inaccurate due to the thermocouples that were embedded using an epoxy. Through experiments on the Plexiglas sub-plate, Walker [7] found a correction factor C_k as seen in Eq. (3.5) and Eq. (3.8). Each heated section had a different conduction parameter used to match the theoretical conditions. Table 3.1 displays the correction factors found by Walker [7]. For a more in-depth account of the experiments performed and the calculations used to find the conduction parameters, refer to Walker [7].

Table 3.1: Conduction parameter values, C_k [7]

Heated Section Number	C_k
0	0.90
1	0.90
2	1.05
3	1.10
4	1.05

Air Properties

Convective heat transfer experiments were run over the course of several weeks. Because of this, the results utilize non-dimensional Stanton numbers for proper comparison. Therefore an analysis of the air properties during each of the tests is required. As mentioned previously in this chapter, an Omega zSeries zED-THYPB-LCD atmospheric conditions monitor was used during each experiment to record the ambient air temperature, pressure, and relative humidity at the tunnel inlet. To get the resulting Stanton numbers, a program based on the International Association for the Properties of Water and Steam guidelines [56], Sutherland's law [57], and Wilke's equation for gas mixtures [58] calculated the air dynamic viscosity, thermal conductivity, density, specific heat, and Prandtl number.

Thermocouple Calibration

Using an *in situ* calibration method, thermocouple readings were referenced to an averaged fifty by fifty pixel temperature as measured by the IR camera. Eq. (3.9) shows this process.

$$T_{TC,calibrated} = T_{TC,test} - (T_{TC,cal} - \bar{T}_{IR,cal}) \quad (3.9)$$

The thermocouples in each section were calibrated to the reading from the IR camera measurements positioned over the corresponding sections.

Smooth Surface Heat Transfer Validation

To validate the data reduction equation used above, Shannon [8] performed convection measurements on a set of smooth surface panels with laminar and turbulent flows. The heat transfer coefficients found were compared to the accepted theoretical values. The experiments shared identical methodology and procedure as the experiments detailed in this paper. For more details of the data reduction validation refer to Shannon [8].

Uncertainty Analysis

Based on the same method used by Shannon [8], the uncertainties of the area averaged heat transfer coefficients presented in Chapter Five were calculated. These uncertainties were found using the large sample size method of Coleman and Steele [59], an extension of Kline and McClintock [60]. The random uncertainties of each of the variables in the data reduction equation, Eq. (3.9), are found using Eq. (3.10).

$$U_{random} = \frac{t \cdot S}{\sqrt{N}} \quad (3.10)$$

In Eq. (3.10), t is the student's t-value, S is the standard deviation of the measurements, and N is the number of samples. Table 3.2 shows the total uncertainty of each of the variables in Eq. (3.9). It is noted that the uncertainty of the Plexiglas sub-plate is not considered in this analysis because it is already accounted for in the conduction correction factors discussed above. For further explanation on the inclusion of uncertainty in the conduction correction factors, refer to Walker [7]. There is no random uncertainty

accompanying the voltage and current measurements in heated section four because only a single sample was taken for these values.

Table 3.2: Convective Heat Transfer Coefficient Measurement Uncertainty [8]

Variable	Total Uncertainty	Uncertainty Components
E	$\sqrt{U_{E,fixed}^2 + \left(\frac{tS_E}{\sqrt{N}}\right)^2}$	$U_{E,fixed} = 0.03\% E$ (sections 0 - 3) $U_{E,fixed} = 0.25\% E$ (section 4)
I	$\sqrt{U_{I,fixed}^2 + \left(\frac{tS_I}{\sqrt{N}}\right)^2}$	$U_{I,fixed} = 0.1$ A (section 0) $U_{I,fixed} = 0.05$ A (sections 1 - 3) $U_{I,fixed} = 2.5\% I$ (section 4)
A_t	$\sqrt{(U_{d,fixed} W_{ha})^2 + (U_{d,fixed} L_{ha})^2}$	$U_{d,fixed} = 1/32''$
T_{IR}	$\sqrt{B_T^2 + \left(\frac{tS_{T_{IR}}}{\sqrt{N}}\right)^2}$	$B_T = 1.4$ K
T_{SS}	$\sqrt{B_T^2 + \left(\frac{tS_{T_{IR}}}{\sqrt{N}}\right)_{cal}^2 + \left(\frac{tS_{T_{SS}}}{\sqrt{N}}\right)_{cal}^2 + \left(\frac{tS_{T_{SS}}}{\sqrt{N}}\right)_{test}^2}$	$B_T = 1.4$ K
T_{UP}	$\sqrt{B_T^2 + \left(\frac{tS_{T_{IR}}}{\sqrt{N}}\right)_{cal}^2 + \left(\frac{tS_{T_{UP}}}{\sqrt{N}}\right)_{cal}^2 + \left(\frac{tS_{T_{UP}}}{\sqrt{N}}\right)_{test}^2}$	$B_T = 1.4$ K
T_∞	$\sqrt{B_T^2 + \left(\frac{tS_{T_{IR}}}{\sqrt{N}}\right)_{cal}^2 + \left(\frac{tS_{T_\infty}}{\sqrt{N}}\right)_{test}^2}$	$B_T = 1.4$ K

Probe Calibration and Data Reduction

Before velocity measurements are taken, a calibration procedure for the x-array probe is performed. To begin calibration, the effective velocity experienced in each of the wires was calculated by Eqs. (3.11) and (3.12).

$$V_{eff,1} = \sqrt{(V_{meas} \cos \alpha_1)^2 + \kappa^2 (V_{meas} \sin \alpha_1)^2} \quad (3.11)$$

$$V_{eff,2} = \sqrt{(V_{meas} \sin \alpha_2)^2 + \kappa^2 (V_{meas} \sin \alpha_2)^2} \quad (3.12)$$

In these equations V_{meas} is the velocity measured by the pitot-static probe, α is the angle of the wire relative to the flow direction (set by the rotary), and κ is the tangential velocity attenuation factor.

A fourth-order polynomial was fit to the effective velocities in each of the two wires on the x-array probe. This polynomial fit is shown in Figure 3.14.

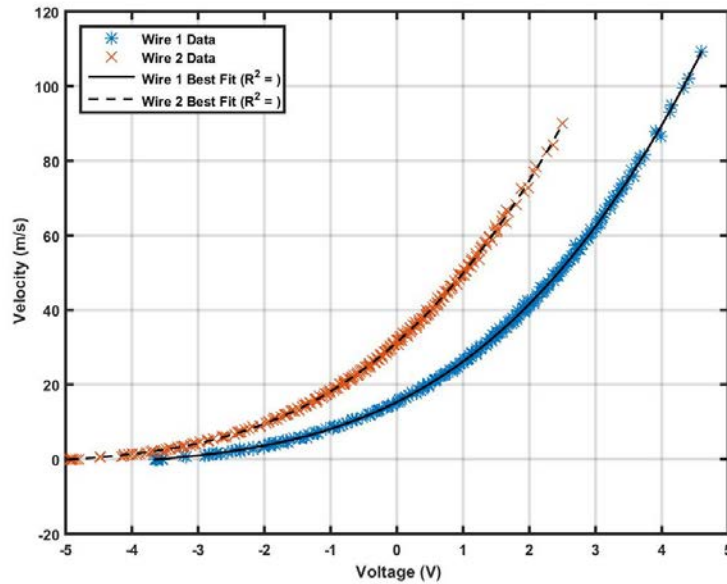


Figure 3.14: Hot-film probe calibration plot

For voltage measurements obtained from the x-array wire, the normal and tangential flows experienced by the first wire were calculated using Eqs. (3.13) and (3.14).

$$V_{N1} = \left(\frac{V_{eff,1}^2 - \kappa^2 V_{eff,2}^2}{1 - \kappa^4} \right)^{1/2} \quad (3.13)$$

$$V_{T1} = \left(\frac{V_{eff,2}^2 - \kappa^2 V_{eff,1}^2}{1 - \kappa^4} \right)^{1/2} \quad (3.14)$$

From the normal and tangential wire velocities, the x and z-components of the flow velocity relative to the probe were found using Eqs. (3.15) and (3.16).

$$u_i = \frac{V_{T1} + V_{N1}}{\sqrt{2}} \quad (3.15)$$

$$w_i = \frac{V_{T1} - V_{N1}}{\sqrt{2}} \quad (3.16)$$

At each of the 101 stations, the mean velocity components were calculated using Eqs.

(3.17) and (3.18)

$$\bar{u} = \frac{1}{N} \sum_{i=1}^N u_i \quad (3.17)$$

$$\bar{w} = \frac{1}{N} \sum_{i=1}^N w_i \quad (3.18)$$

Finally, the root-mean-square turbulent fluctuating velocity components were assessed using Eqs. (3.19) and (3.20).

$$u'_{RMS} = \sqrt{\frac{1}{N-1} \sum_{i=1}^N (u_i - \bar{u})^2} \quad (3.19)$$

$$w'_{RMS} = \sqrt{\frac{1}{N-1} \sum_{i=1}^N (w_i - \bar{w})^2} \quad (3.20)$$

CHAPTER FOUR

Results and Discussion

This chapter will first present the results from the smooth surface flow measurements and validation. Next, the results from the convective heat transfer tests will be presented. The SSL and IRT convective results will be discussed first, followed by the presentation and discussion of the real ice roughness surface results. Lastly, the convective results from the autocorrelation surfaces will be presented and discussed.

Smooth Surface Flow Measurements and Validation

Figure 4.1 presents the boundary layer traces at each of the five sections along the smooth surface on the sub-plate. The freestream velocity in each of the sections can be observed where the velocity trace is essentially constant in a vertical line. Using the freestream velocity, the acceleration of the flow due to the ceiling insert can be observed. The flow accelerates from section zero to section three and begins to decelerate slightly at the back of the sub-plate where the ceiling insert begins to expand again. The velocities through the test section develop as predicted.

Figure 4.2 plots the freestream velocities found from the smooth surface boundary layer trace against the calculated airfoil velocity variation and also the design velocity variation by the ceiling insert discussed in Chapter Three. The calculated freestream velocities along the smooth surface match the design velocities very well. The velocities experienced by the test surface match the case of a NACA 0012 airfoil with a 50-in. chord in 67-m/s (130-knots) flow.

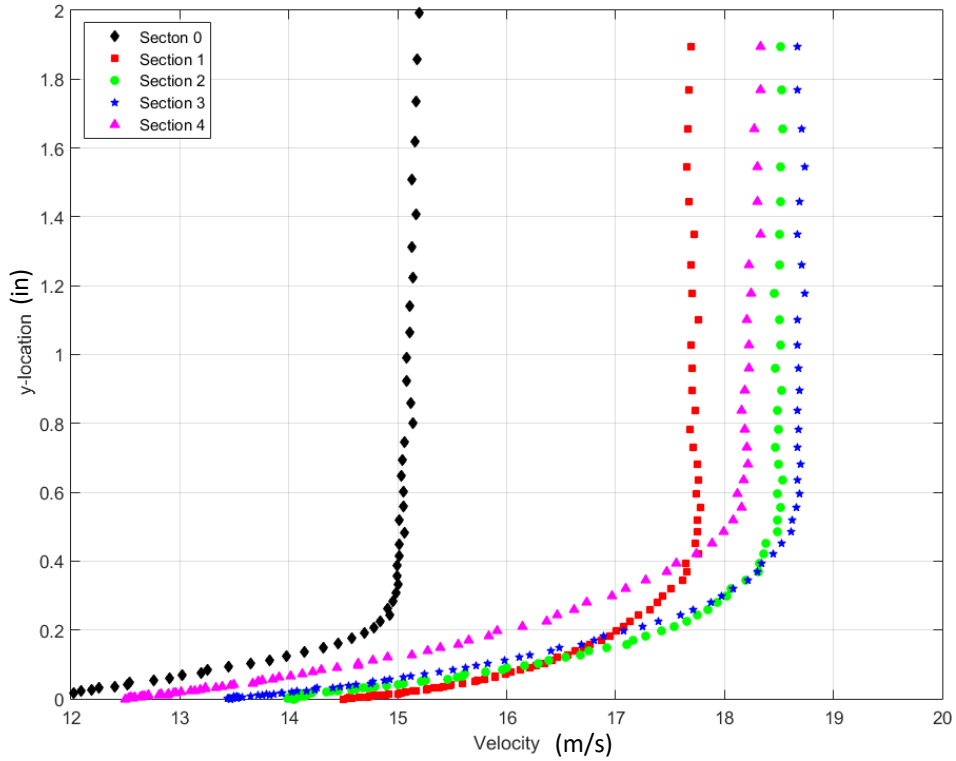


Figure 4.1: Smooth surface boundary layer trace

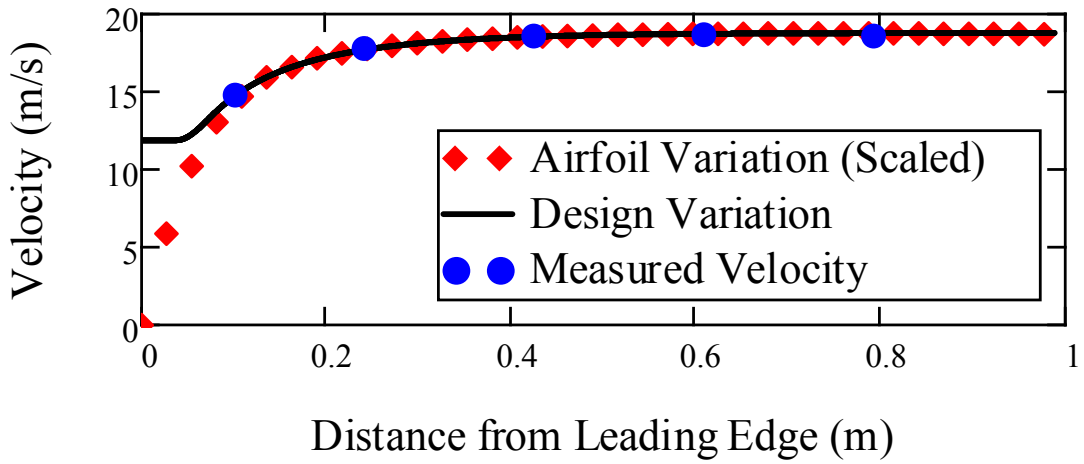


Figure 4.2: Design airfoil velocity variation plotted with measured freestream velocities along a smooth surface

Convective Heat Transfer Results

SSL and IRT Surface Results

Figure 4.3 presents contour maps of the local convection coefficients for the SSL Plastic Hemisphere, SSL Plastic Cone, and SSL Aluminum Cone surfaces. An initial observation of these contour maps in the hemispherical elements appear a darker red than the conical elements. This is likely caused by the interaction between the pressure gradient and the roughness elements. The pressure gradient forces the fluid to the surface, and the hemispherical elements, which have a greater surface area, show increased heat transfer.

Figure 4.4 presents contour maps of the local convection coefficients for the IRT Plastic Hemisphere, IRT Plastic Cone, and IRT Aluminum Cone surfaces. An initial observation of the IRT contour maps is the individual elements are lighter than those of the SSL surfaces. The effect of the gradual smooth-to-rough transition on the heat transfer coefficients can be seen on the contour maps.

For a proper and more detailed comparison of the test results, the area averaged heat transfer coefficients, in a 2-in square (100 by 100 pixels) centered on each section's thermocouple pair, were used to calculate the localized Stanton number. As mentioned in Chapter Three, non-dimensional Stanton numbers take into account the air properties during each test, thus allowing for a proper comparison between tests taken over a period of several weeks. Stanton numbers are plotted against Reynolds numbers, using the air properties and velocities measured during each test. The Stanton number plots display two theoretical correlation lines, turbulent and laminar, that display the theoretical heat transfer results along a smooth surface, as discussed in Chapter Three.

Local Stanton number plots for the SSL surfaces and are presented in Figure 4.5 (a). As expected, the hemispherical surface exhibits slightly higher Stanton numbers than the plastic conical surface. The aluminum conical surface has Stanton numbers noticeably higher than the plastic surfaces due to material thermal conductivity. The control panels upstream and downstream of the aluminum surface panels (sections zero and four) match the Stanton number values of the corresponding plastic surface. The abrupt smooth-to-rough transition causes a rapid increase in Stanton numbers in heated section one. After the transition, the Stanton numbers are relatively constant along the surface. This result is anticipated because the surface has constant roughness properties downstream from the smooth-to-rough transition.

Figure 4.5 (b) presents the local Stanton number plots for the IRT surfaces. The local Stanton numbers for the IRT surfaces are discernably lower than those of the SSL surfaces. This is an expected result in heated Sections One and Four as the roughness properties on the IRT surfaces are smaller and the smooth-to-rough transition is gradual, rather than the abrupt transition on the SSL surface. However, at heated Section Two the roughness properties between the IRT and SSL patterns match, but still differ in Stanton number values. An explanation of this difference could be attributed to the fact that the later and more gradual smooth-to-rough transition on the IRT surfaces does not create the same elevated levels of turbulence near the surface roughness, which would cause lower Stanton numbers. Also seen on Figure 4.5 (b) is that the shape of the individual plastic elements does not have an effect on the measured Stanton numbers to a greater level than the uncertainty bands. Meaning, although the measured convection coefficients differ between different elements (seen in Figure 4.4), the area average Stanton numbers are not

sensitive to these differences. Again, the aluminum surface exhibits higher measured Stanton numbers due to its lack of thermal resistance.

Real Ice Convection Results

Contour maps of the local convection coefficients for the plastic and aluminum real ice surfaces are presented in Figures 4.6 and 4.7 respectively. As anticipated, the heat transfer coefficients on the aluminum surfaces are higher than those on the plastic surfaces. The smooth-to-rough transition point for each of the real ice surfaces can be observed on the plastic contour maps. The 112912.02 and 112912.06 exhibit a much earlier transition. The effect of the transition zone on the heat transfer coefficients is most evident when inspecting Figure 4.7, the aluminum contour maps. Also observed on the plastic contour maps is with larger individual roughness elements comes higher (darker red) convective heat transfer. Figure 4.8 (a) and (b) displays the Stanton number results for the plastic and aluminum real ice surfaces respectively. As observed by Figure 4.7, the aluminum heated test sections (b) have higher resulting Stanton numbers. This is an expected result as aluminum has a higher thermal conductivity than the plastic. Section zero, the smooth surface with the bullnose, is unheated and serves as a control between all of the tests. The first three local Stanton numbers should remain relatively consistent given some uncertainty.

One interesting difference between the tested surfaces occurs at the differing smooth-to-rough transition points as discussed above. In Figure 4.8 (a), the plastic surfaces, the effect of the transition can be seen in the fifth thermocouple pair. The two surfaces with earlier smooth-to-rough transition, the 112912.02 and the 112912.06 surfaces, show higher Stanton numbers.

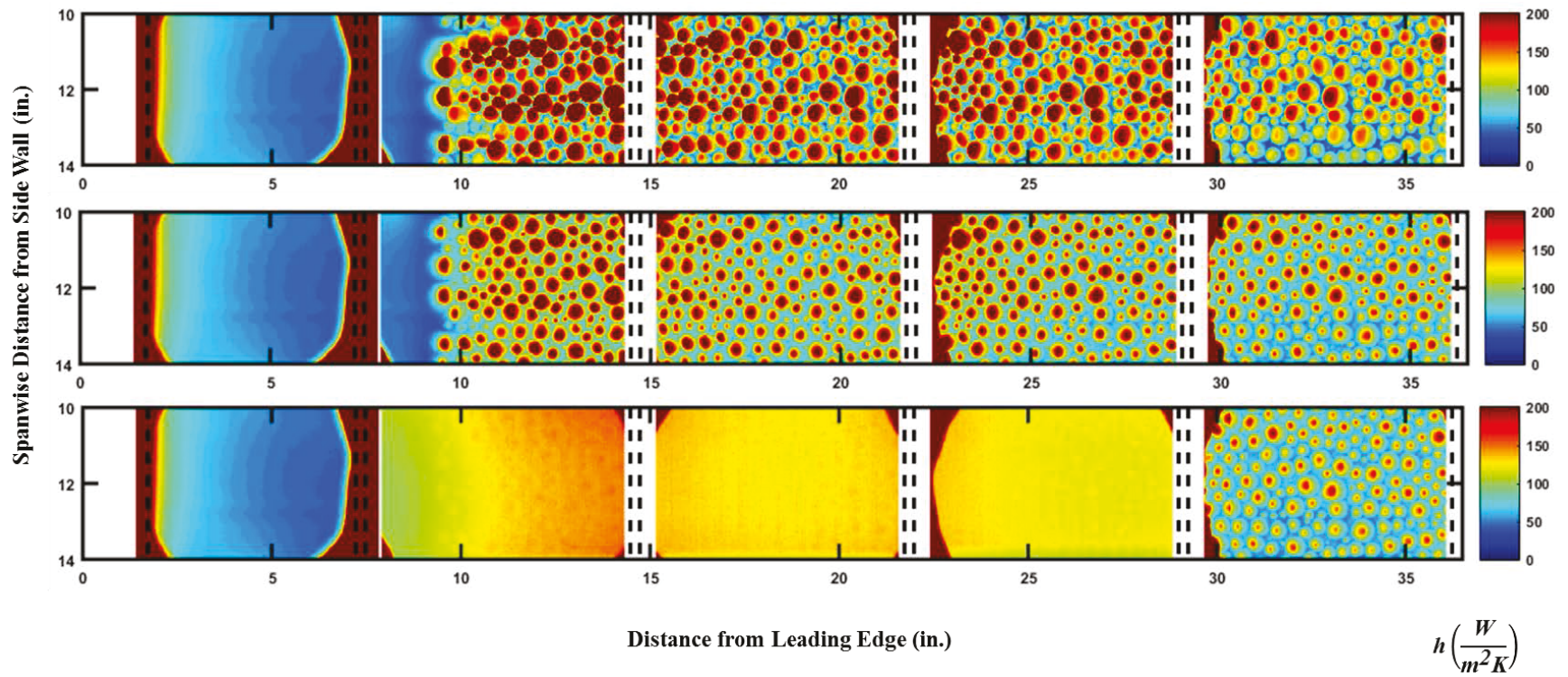


Figure 4.3: Convective heat transfer coefficient contour plot for (a) SSL Plastic Hemisphere, (b) SSL Plastic Cone, and (c) SSL Aluminum Cone

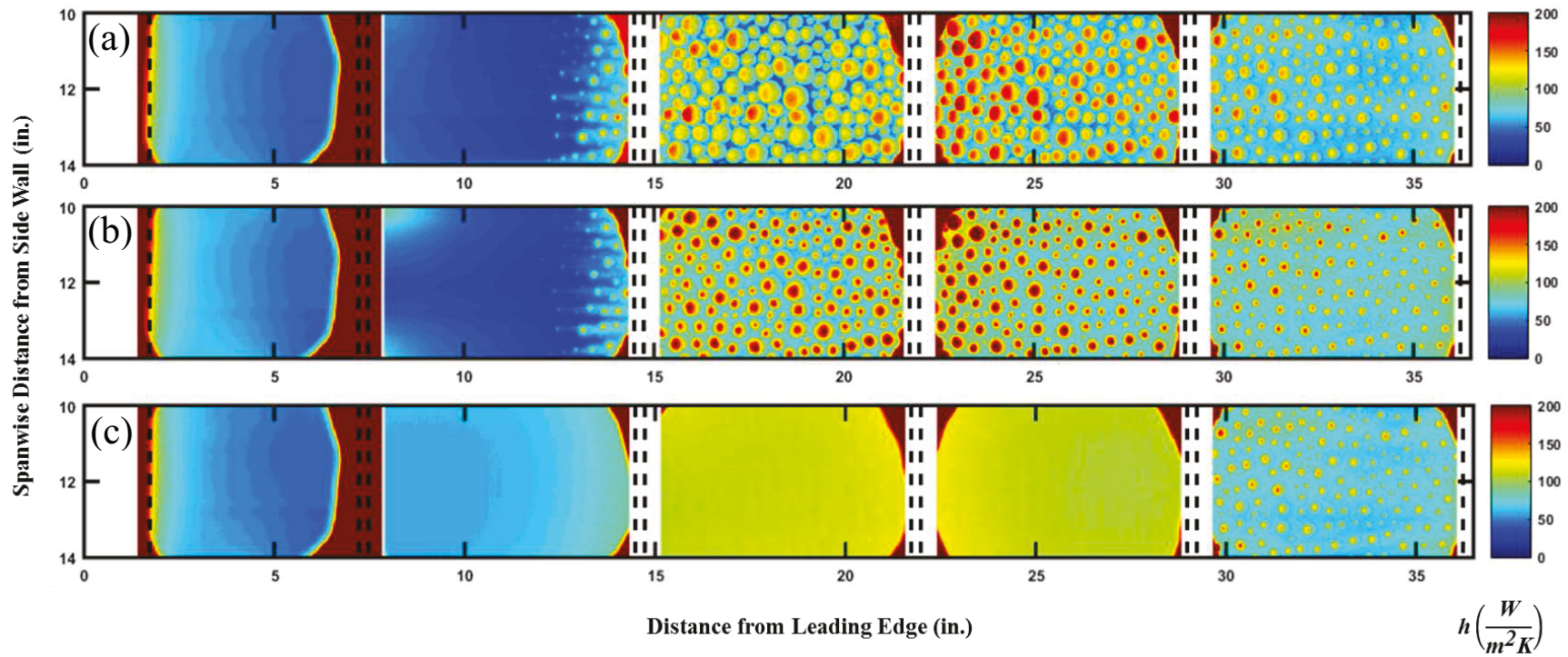


Figure 4.4: Convective heat transfer coefficient contour plot for (a) IRT Plastic Hemisphere, (b) IRT Plastic Cone, and (c) IRT Aluminum Cone

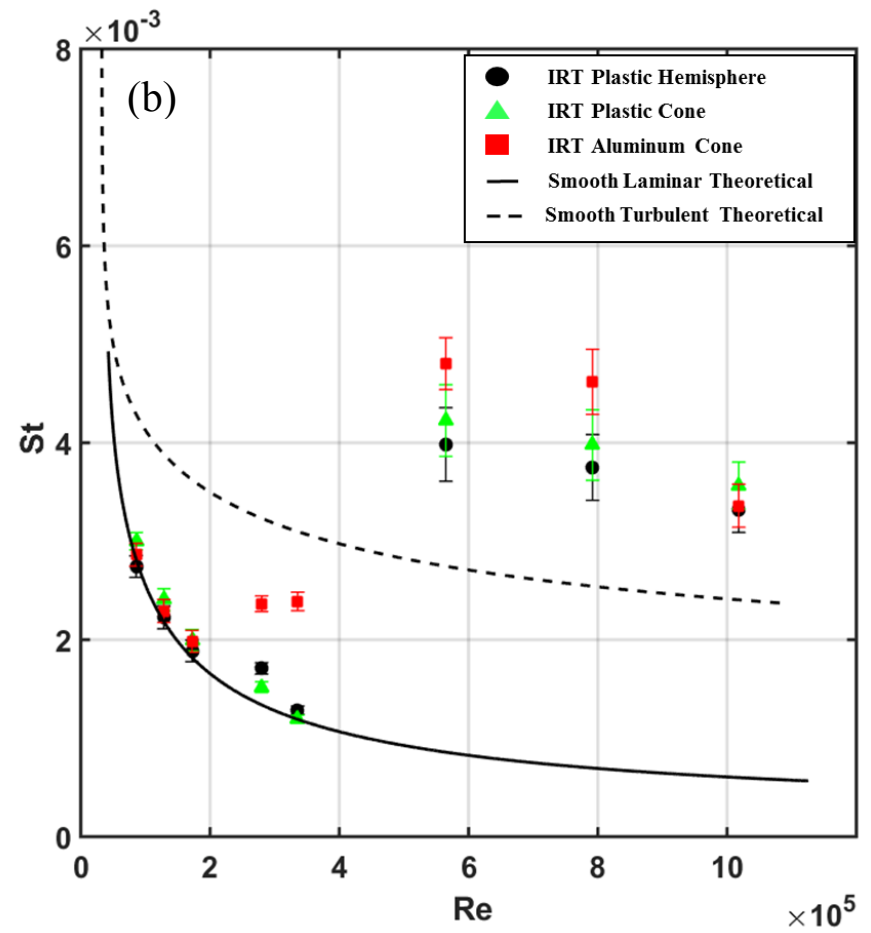
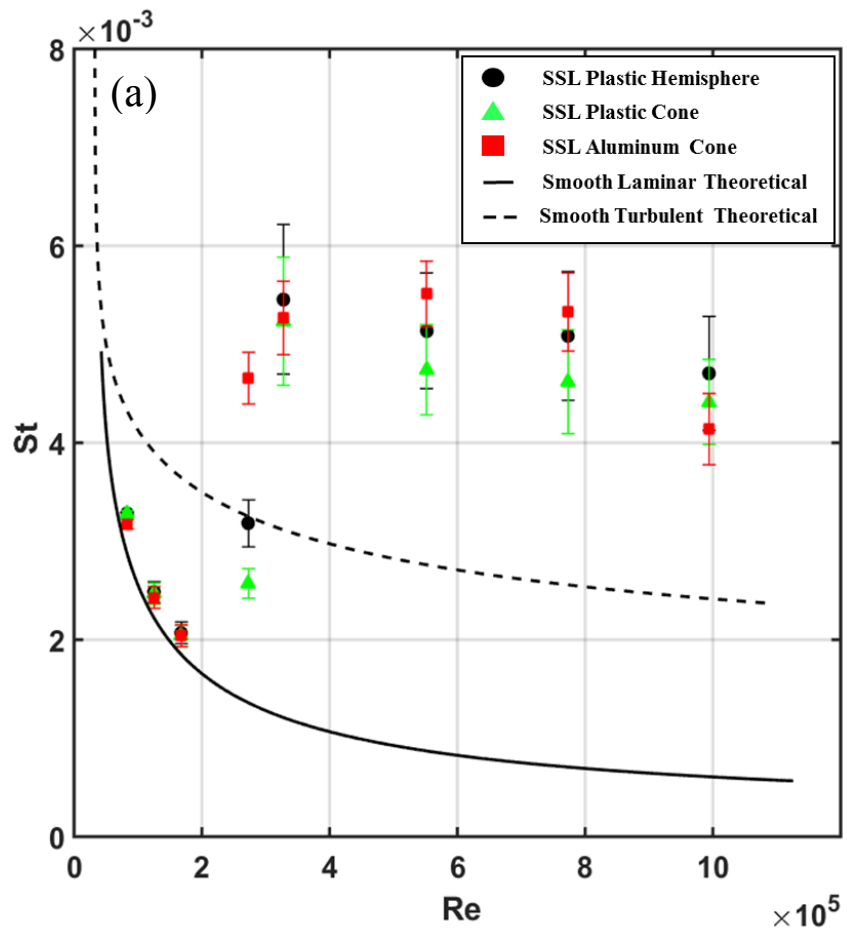


Figure 4.5 Local Stanton number measurements for (a) SSL Surfaces and (b) IRT Surfaces

On the aluminum surfaces, Figure 4.7 (b), this transition effect is more clearly seen on both the fourth and fifth thermocouple pairs. Beyond the smooth-to-rough transition areas, the trends of the Stanton number plot are closer to what is expected, with larger roughness elements heights causing larger Stanton numbers. One possible solution for addressing the discrepancy caused by transition location would be to recreate the results of these experiments on reconstructed surfaces with the same geometries, but consistent transition locations.

The expectation of the experimental results was surfaces with larger roughness heights produce a larger heat transfer enhancement. Examining heated sections three and four, the areas where the roughness is full developed and beginning to decay, this expectation seems to hold true. The Stanton numbers for the 113012.04 and 112912.06 surfaces, the surfaces with larger roughness elements, are higher than the two smaller surfaces (113012.05 and 112912.02). However, with the inclusion of uncertainty bars, the difference in Stanton numbers between the surfaces are not as significant as first predicted. It is also observed from the results of the 113012.04 surface that the trends in Stanton numbers for the IRT surface do not match results of a real ice roughness surface. This is likely because the IRT surface uses a single length scale when attempting to match the roughness of the 113012.04 surface.

Autocorrelation Analog Surface Results

Local heat transfer contour maps for the plastic and aluminum analog surfaces and the 113012.04 real ice surface are shown in Figures 4.9 and 4.10. On the plastic surfaces (Figure 4.8) the ellipsoidal surface has the darkest elements. This could be attributed to the larger elemental surface areas of the ellipsoids interacting with the flow

pushed to the surface by the acceleration insert compared to the more ridge-like shapes of the real ice and the elliptical cones. Also seen on the plastic contour maps is the effect of the flow moving around the roughness elements and its effect on the heat transfer enhancement. The trends between each plastic contour map appear to match quite well, especially the 113012.04 and the elliptical cone surface. On the aluminum heat transfer contour maps, the real ice surface appears to have slightly higher heat transfer enhancement than the two analog surfaces. This is most evident downstream of the point of peak roughness.

Again, for proper comparison the results are presented in local Stanton number plots. Figure 4.11 presents the Stanton number plot comparisons for plastic (a) and aluminum (b) surfaces. For both aluminum and plastic cases, the first two sections match and follow the theoretical lines due to these sections having little to no roughness.

On Figure 4.11 (a), the plastic Stanton number plots, the autocorrelation surfaces are discernably higher than the real ice surface, especially at heated section two (the sixth thermocouple pair). A possible explanation for the significantly high Stanton number at this heated section could be the group of large roughness elements centered at the thermocouple pair. Although the Stanton numbers use an area average around the thermocouple pair, these wide elements, under relatively large Reynolds numbers and freestream acceleration, do not make good fins and display a pseudo raised convection enhancement. This highlights the importance of testing roughness surfaces using a high conductivity material such as aluminum.

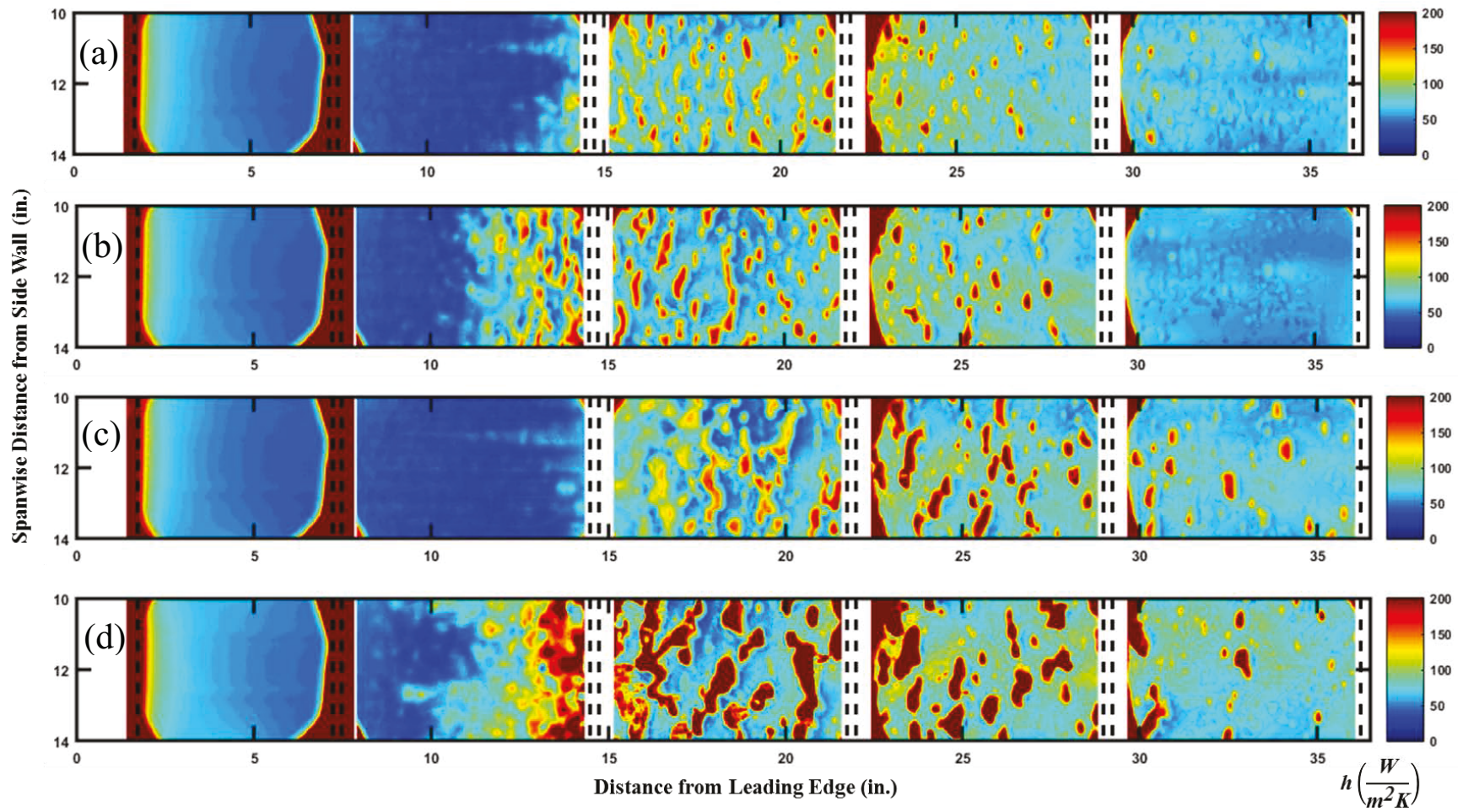


Figure 4.6: Convective heat transfer coefficient contour plot for plastic surfaces (a) 113012.05, (b) 112912.02, (c) 113012.04, (d) 112912.06

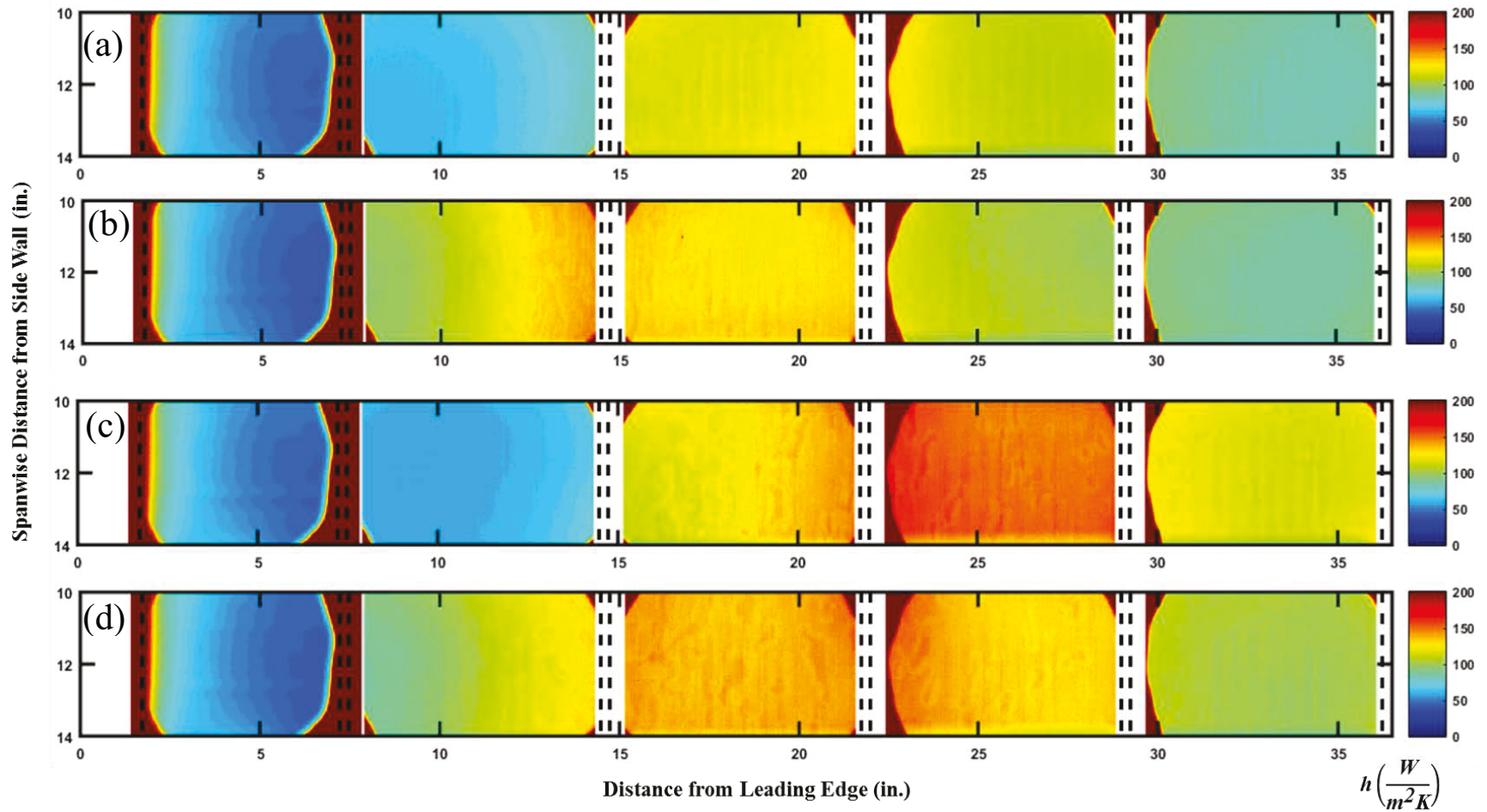


Figure 4.7: Convective heat transfer coefficient contour plot for aluminum surfaces (a) 113012.05, (b) 112912.02, (c) 113012.04, (d) 112912.06

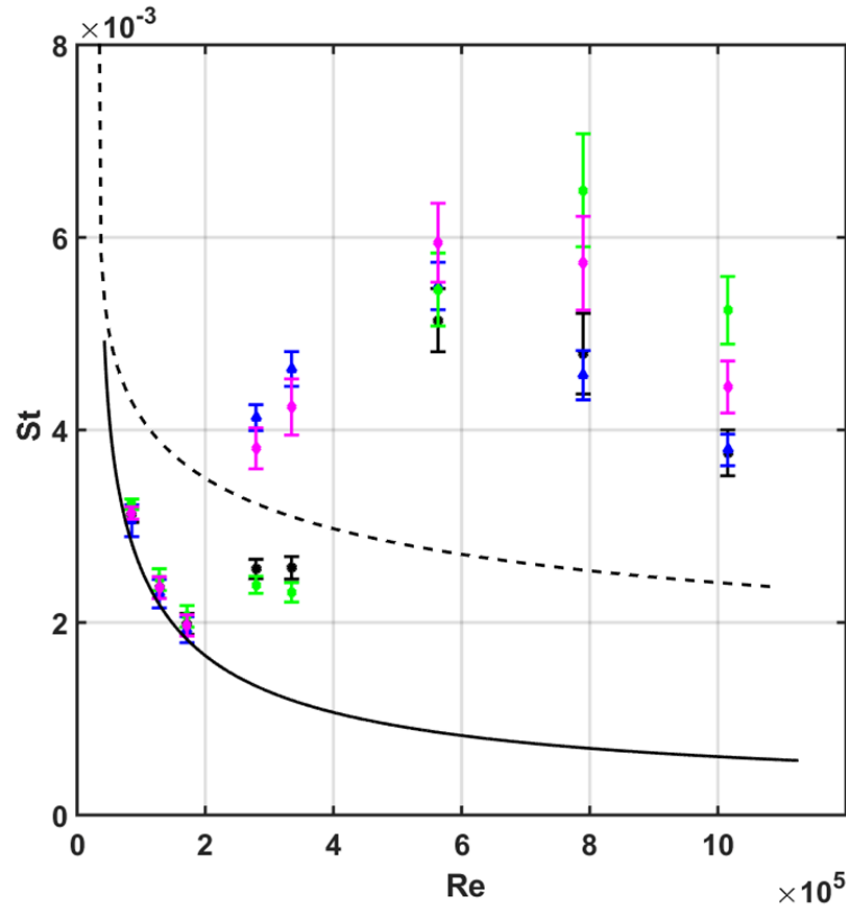
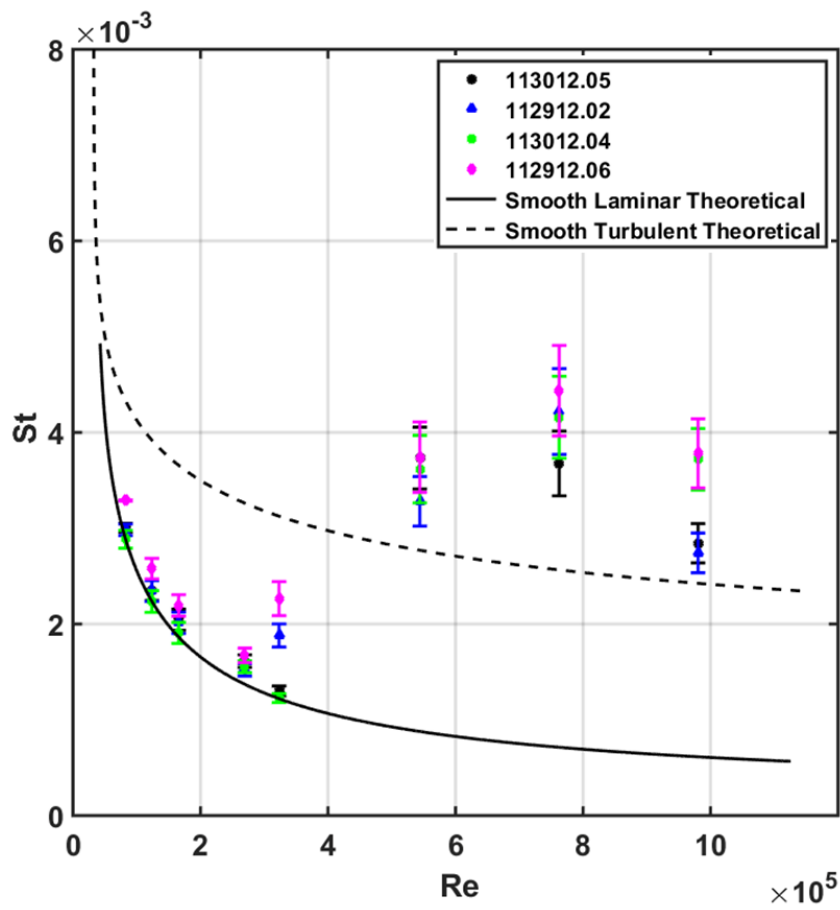


Figure 4.8: Local Stanton number measurements for (a) plastic and (b) aluminum real ice roughness surface

The aluminum Stanton numbers, Figure 4.11 (b), are higher than the plastic Stanton numbers because of the material thermal conductivity discussed above. The aluminum surfaces show more reasonable matching in heated section two compared to the plastic Stanton numbers. The Stanton numbers on the aluminum analog surfaces are slightly lower than those of the real ice surface in heated sections three and four. This may be because, as discussed in Chapter Two, the autocorrelation function was performed on an 8-in by 8-in area at 17-in downstream of the leading edge. The roughness characteristics downstream of this peak roughness region were likely not captured properly. The analog roughness elements do not capture the random nature of the small decaying roughness elements of the 113012.04.

Though analog surfaces of Clemenson [12] are not perfect in matching the real ice 113012.04 they are an improvement of the IRT surfaces. The analog surfaces employ multiple length scales to match the real ice surface, whereas the IRT surface only uses the global streamwise height variations.

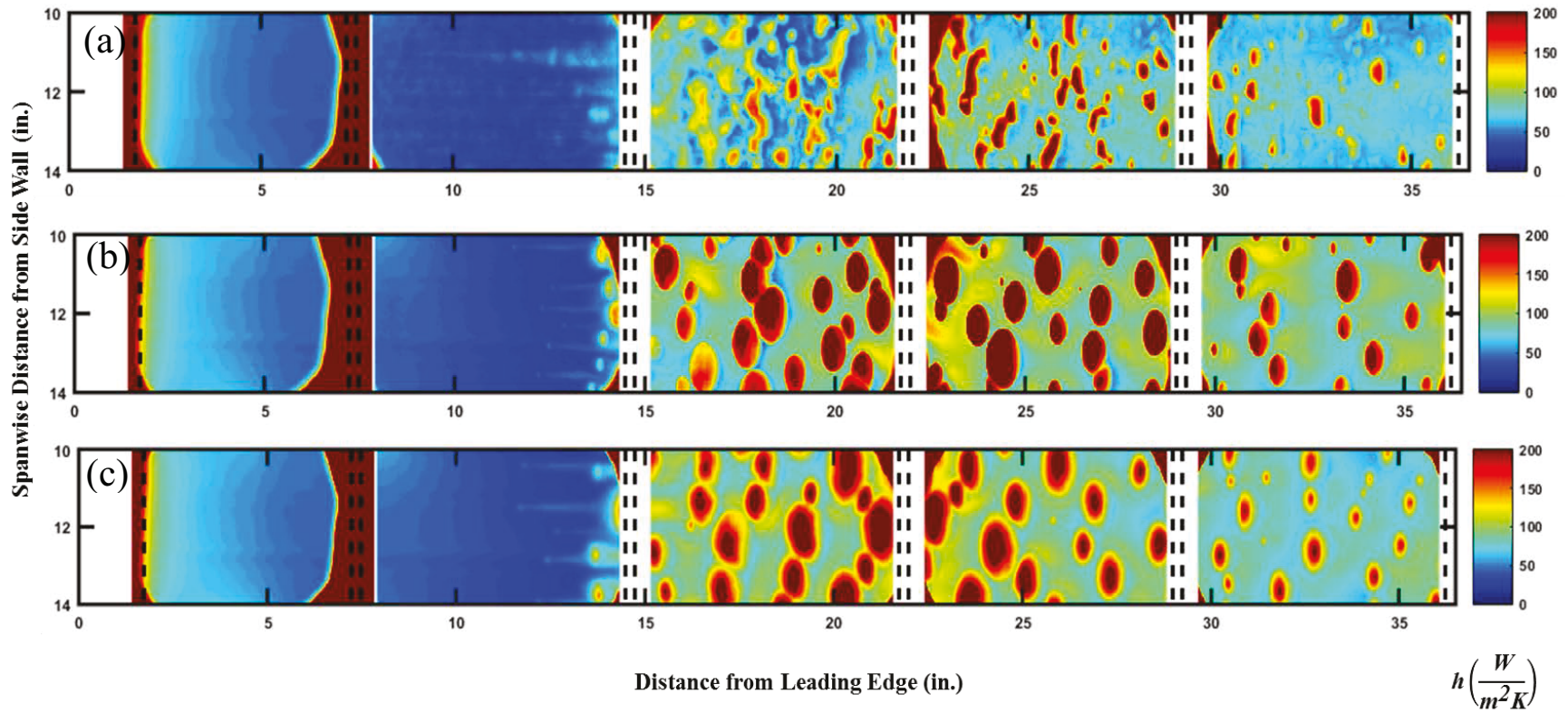


Figure 4.9: Convective heat transfer coefficient contour plot for plastic surfaces (a) 113012.04, (b) Ellipsoids, (c) Elliptical Cones

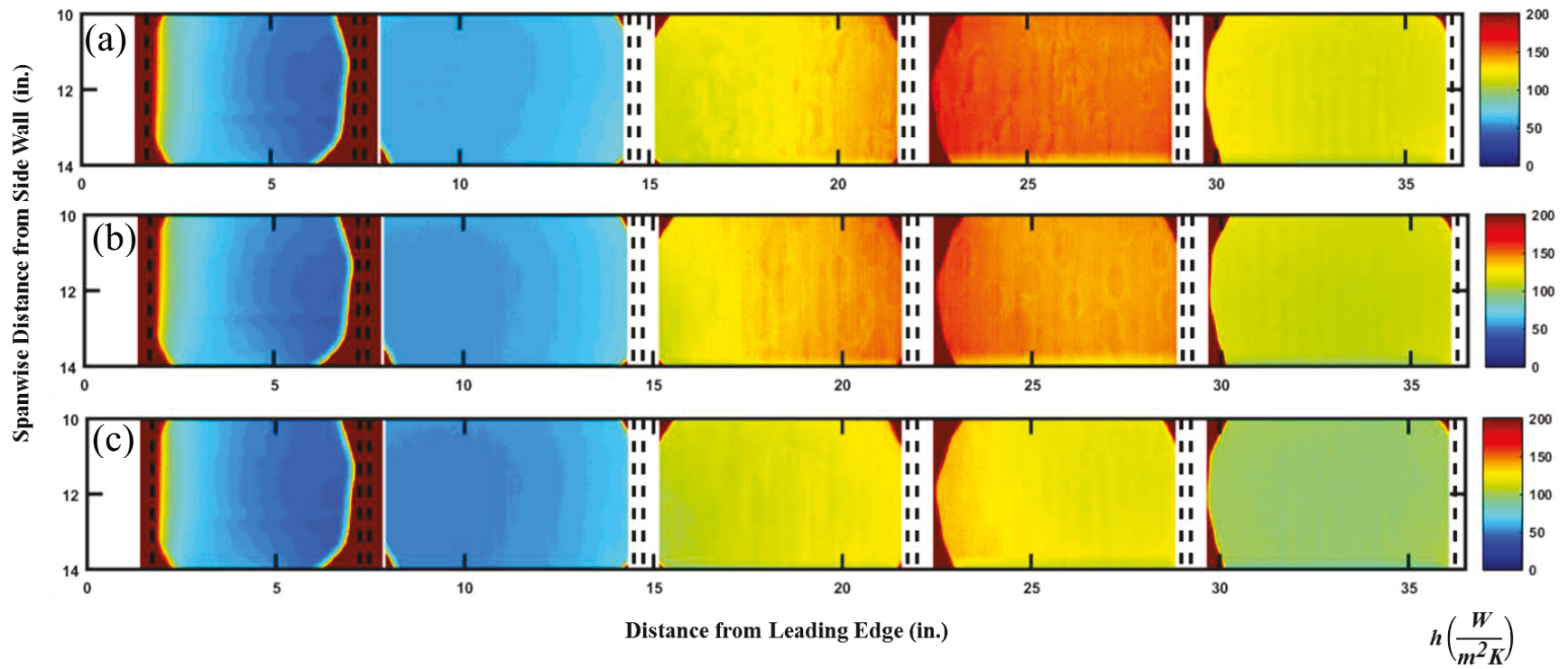


Figure 4.10: Convective heat transfer coefficient contour plot for aluminum surfaces (a) 113012.04, (b) Ellipsoids, (c) Elliptical Cones

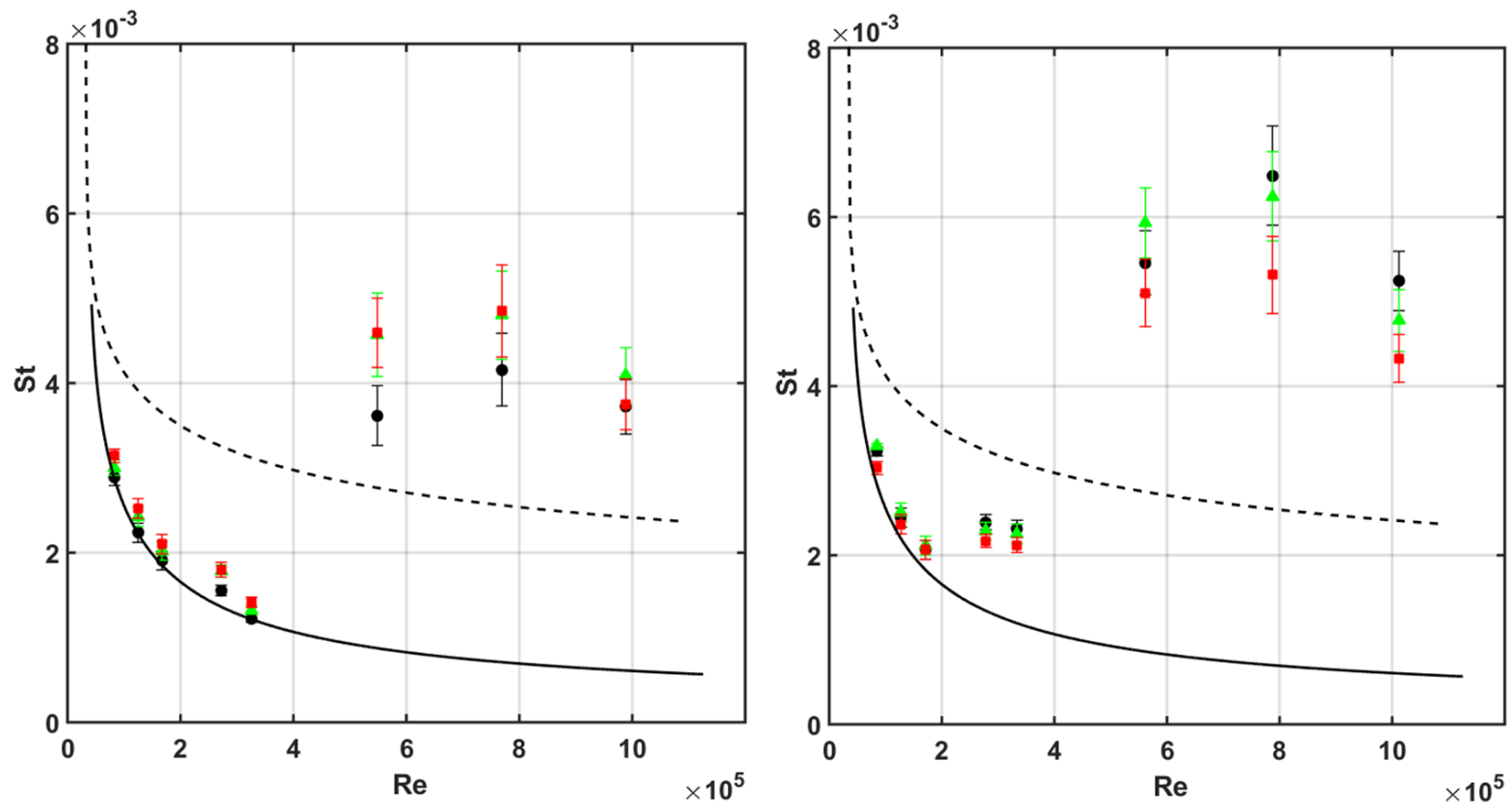


Figure 4.11: Local Stanton number measurements for (a) plastic surfaces (b) aluminum surfaces

CHAPTER FIVE

Conclusions

Summary of Work

A series of experiments were performed to characterize the convective heat transfer of real and analog ice roughness surfaces experiencing flows similar to those found on NACA 0012 airfoils larger than 21-in. Ten roughness surfaces were tested in this investigation. Two of the surfaces simulate ice roughness and were created using the historical view of ice roughness which consists of an abrupt smooth-to-rough transition and the roughness properties are constant in the downstream direction. The next two surfaces tested were created in a similar way to the historical roughness surfaces but implemented surface roughness variations in the downstream direction. Four of the surfaces were created using laser scan data of real ice shapes to create a set of real ice roughness surfaces that form a temporal progression of ice roughness. The final two surfaces used autocorrelation to match multiple length scales of a real ice roughness surface in order to better replicate a real ice roughness.

Although these surfaces were created using data gathered from ice accretions on a 21-in NACA 0012 airfoil, a previous study determined roughness in the collection region of a NACA 0012 airfoil scales geometrically. Therefore the surfaces are tested using Reynolds number scaling to characterize convective enhancement of the roughness on a larger airfoil.

The primary findings of this investigation were:

- The velocity profiles along a smooth surface through the test section developed as designed to match flow of a NACA 0012 airfoil with a 50-in chord in 67-m/s (130-knots) flow.
- The abrupt smooth-to-rough transition of the SSL surfaces have significant impact on the convective enhancement and provide information on the historical view of surface ice roughness. When using a more contemporary approach to ice roughness, the roughness heights vary along the downstream direction and exhibit a more gradual smooth-to-rough transition. This causes the roughness surface to exhibit lower convection coefficients, even in the areas where the SSL and IRT roughness heights match. The IRT surfaces only use a single length scale to match real ice data, resulting in differing convective enhancement between the IRT and Real Ice surfaces.
- The convective enhancement between the four real ice surfaces is not as sensitive to exposure time as expected, but is rather more dependent on the location of the smooth-to-rough transition. A more proper comparison of the convective enhancement between the surfaces could be observed by reconstruction of the roughness surfaces with a consistent transition point.
- The aluminum ellipsoidal surface matches the 113012.04 surface well in the area of maximum roughness but shows lower Stanton numbers downstream of this location. The roughness characteristics downstream of the area of peak roughness, where the autocorrelation was performed, do not capture the random nature of the small decaying elements on the 113012.04 real ice surface.

Future Work

Future research efforts will continue to investigate different aspects of ice roughness to improve on the characterization of convective enhancement prediction of LEWICE. Detailed skin friction coefficient data along several roughness surfaces is important for the improvement of the correlations used. Characterization of convective heat transfer and skin friction coefficients from ice accretions formed on different types of airfoils and swept wings can further improve the prediction methods of LEWICE.

APPENDIX

Test Data

This appendix provides the test data for the all of the convective heat transfer tests.

Table A.1: SSL Hemisphere

Parameter	0a	0b	0c	1a	1b	2	3	4
x (in)	3.10	4.48	5.85	9.23	10.98	18.23	25.48	32.73
A_t (in ²)	35.06	35.06	35.06	44.63	44.63	44.63	44.63	44.63
ϵ	0.95	0.95	0.95	0.95	0.95	0.95	0.95	0.95
σ (W/m ² K ⁴)	5.67e-8	5.67e-8	5.67e-8	5.67e-8	5.67e-8	5.67e-8	5.67e-8	5.67e-8
t_p (in)	0.72	0.72	0.72	0.72	0.72	0.72	0.72	0.72
C_k	0.90	0.90	0.90	0.90	0.90	1.05	1.10	1.05
E (V)	6.47	6.47	6.47	5.97	5.97	6.07	6.64	6.01
I (A)	2.11	2.11	2.11	2.55	2.55	2.53	2.68	2.64
k_p (W/mK)	0.205	0.205	0.205	0.205	0.205	0.205	0.205	0.205
T_{SS} (K)	311.85	312.15	312.86	310.16	310.85	311.26	312.81	314.54
T_{UP} (K)	295.40	295.81	296.05	296.17	296.12	296.71	297.18	297.45
T_∞ (K)	294.24	294.24	294.24	294.24	294.24	294.24	294.24	294.24
T_{IR} (K)	300.26	301.76	302.79	299.27	297.19	297.18	297.72	297.32
h (W/m ² K)	66.94 ± 0.28	52.56 ± 2.33	44.99 ± 2.4	71.31 ± 5.34	123.28 ± 17.17	117.65 ± 13.45	116.81 ± 15.02	108.16 ± 13.3

Table A.2: SSL Cone Plastic

Parameter	0a	0b	0c	1a	1b	2	3	4
x (in)	3.10	4.48	5.85	9.23	10.98	18.23	25.48	32.73
A _t (in ²)	35.06	35.06	35.06	44.63	44.63	44.63	44.63	44.63
ϵ	0.95	0.95	0.95	0.95	0.95	0.95	0.95	0.95
σ (W/m ² K ⁴)	5.67e-8	5.67e-8	5.67e-8	5.67e-8	5.67e-8	5.67e-8	5.67e-8	5.67e-8
t _p (in)	0.72	0.72	0.72	0.72	0.72	0.72	0.72	0.72
C _k	0.90	0.90	0.90	0.90	0.90	1.05	1.10	1.05
E (V)	6.44	6.44	6.44	5.97	5.97	6.06	6.55	6.01
I (A)	2.10	2.10	2.10	2.54	2.54	2.53	2.70	2.64
k _p (W/mK)	0.205	0.205	0.205	0.205	0.205	0.205	0.205	0.205
T _{SS} (K)	312.84	313.23	314.01	310.75	310.67	310.96	313.25	312.95
T _{UP} (K)	296.39	296.86	297.13	297.25	297.09	297.63	298.14	298.20
T _∞ (K)	295.53	295.53	295.53	295.53	295.53	295.53	295.53	295.53
T _{IR} (K)	301.50	303.00	304.10	301.71	298.68	298.83	299.38	299.06
h (W/m ² K)	66.73 ± 0.67	52.56 ± 2.29	44.18 ± 2.38	57.52 ± 3.37	118.04 ± 14.66	108.40 ± 10.48	105.95 ± 12.1	101.32 ± 9.9

Table A.3: SSL Cone Aluminum

Parameter	0a	0b	0c	1a	1b	2	3	4
x (in)	3.10	4.48	5.85	9.23	10.98	18.23	25.48	32.73
A _t (in ²)	35.06	35.06	35.06	44.63	44.63	44.63	44.63	44.63
ϵ	0.95	0.95	0.95	0.95	0.95	0.95	0.95	0.95
σ (W/m ² K ⁴)	5.67e-8	5.67e-8	5.67e-8	5.67e-8	5.67e-8	5.67e-8	5.67e-8	5.67e-8
t _p (in)	0.72	0.72	0.72	0.72	0.72	0.72	0.72	0.72
C _k	0.90	0.90	0.90	0.90	0.90	1.05	1.10	1.05
E (V)	6.44	6.44	6.44	5.91	5.91	6.03	6.44	6.01
I (A)	2.09	2.09	2.09	2.58	2.58	2.54	2.73	2.64
k _p (W/mK)	0.205	0.205	0.205	0.205	0.205	0.205	0.205	0.205
T _{SS} (K)	312.94	313.13	313.54	303.20	303.92	303.47	305.48	312.01
T _{UP} (K)	296.68	297.09	297.28	296.64	296.62	296.81	297.27	298.11
T _∞ (K)	295.45	295.45	295.45	295.45	295.45	295.35	295.45	295.55
T _{IR} (K)	301.58	303.02	304.05	299.68	299.12	298.90	299.44	299.30
h (W/m ² K)	64.49 ± 0.98	51.35 ± 2.34	44.23 ± 2.4	104.04 ± 5.88	118.64 ± 8.4	125.82 ± 7.61	122.03 ± 9.08	94.86 ± 8.3

Table A.4: IRT Hemisphere

Parameter	0a	0b	0c	1a	1b	2	3	4
x (in)	3.10	4.48	5.85	9.23	10.98	18.23	25.48	32.73
A_t (in ²)	35.06	35.06	35.06	44.63	44.63	44.63	44.63	44.63
ε	0.95	0.95	0.95	0.95	0.95	0.95	0.95	0.95
σ (W/m ² K ⁴)	5.67e-8	5.67e-8	5.67e-8	5.67e-8	5.67e-8	5.67e-8	5.67e-8	5.67e-8
t_p (in)	0.72	0.72	0.72	0.72	0.72	0.72	0.72	0.72
C_k	0.90	0.90	0.90	0.90	0.90	1.05	1.10	1.05
E (V)	6.48	6.48	6.48	6.03	6.03	6.03	6.53	6.01
I (A)	2.09	2.09	2.09	2.53	2.53	2.51	2.66	2.64
k_p (W/mK)	0.205	0.205	0.205	0.205	0.205	0.205	0.205	0.205
T_{SS} (K)	310.61	310.77	312.28	308.51	311.48	310.17	309.69	308.69
T_{UP} (K)	294.66	295.23	295.64	295.74	295.36	296.00	296.39	296.51
T_∞ (K)	293.48	293.48	293.48	293.48	293.48	293.48	293.48	293.48
T_{IR} (K)	300.57	301.81	302.68	302.57	304.02	297.17	298.23	298.45
h (W/m ² K)	56.16 ± 2.24	47.41 ± 2.47	41.16 ± 2.39	38.45 ± 1.3	29.13 ± 8.4	91.58 ± 8.59	86.47 ± 7.7	94.86 ± 5.16

Table A.5: IRT Cone Plastic

Parameter	0a	0b	0c	1a	1b	2	3	4
x (in)	3.10	4.48	5.85	9.23	10.98	18.23	25.48	32.73
A _t (in ²)	35.06	35.06	35.06	44.63	44.63	44.63	44.63	44.63
ε	0.95	0.95	0.95	0.95	0.95	0.95	0.95	0.95
σ (W/m ² K ⁴)	5.67e-8	5.67e-8	5.67e-8	5.67e-8	5.67e-8	5.67e-8	5.67e-8	5.67e-8
t _p (in)	0.72	0.72	0.72	0.72	0.72	0.72	0.72	0.72
C _k	0.90	0.90	0.90	0.90	0.90	1.05	1.10	1.05
E (V)	6.47	6.47	6.47	5.99	5.99	6.01	6.42	6.01
I (A)	2.10	2.10	2.10	2.52	2.52	2.49	2.68	2.64
k _p (W/mK)	0.205	0.205	0.205	0.205	0.205	0.205	0.205	0.205
T _{SS} (K)	309.92	309.93	311.06	309.19	312.32	307.49	308.17	306.94
T _{UP} (K)	294.09	294.47	294.72	294.93	295.13	295.20	295.45	295.47
T _∞ (K)	293.07	293.07	293.07	293.07	293.07	293.07	293.07	293.07
T _{IR} (K)	299.60	300.83	301.87	302.52	303.67	296.69	297.57	297.77
h (W/m ² K)	62.01 ± 1.81	51.68 ± 2.42	43.93 ± 2.4	34.48 ± 1.24	27.29 ± 0.96	98.07 ± 8.44	92.58 ± 8.34	83.07 ± 5.55

Table A.6: IRT Cone Aluminum

Parameter	0a	0b	0c	1a	1b	2	3	4
x (in)	3.10	4.48	5.85	9.23	10.98	18.23	25.48	32.73
A_t (in ²)	35.06	35.06	35.06	44.63	44.63	44.63	44.63	44.63
ϵ	0.95	0.95	0.95	0.95	0.95	0.95	0.95	0.95
σ (W/m ² K ⁴)	5.67e-8	5.67e-8	5.67e-8	5.67e-8	5.67e-8	5.67e-8	5.67e-8	5.67e-8
t_p (in)	0.72	0.72	0.72	0.72	0.72	0.72	0.72	0.72
C_k	0.90	0.90	0.90	0.90	0.90	1.05	1.10	1.05
E (V)	6.51	6.51	6.51	5.98	5.98	6.04	6.38	6.01
I (A)	2.09	2.09	2.09	2.58	2.58	2.53	2.72	2.64
k_p (W/mK)	0.205	0.205	0.205	0.205	0.205	0.205	0.205	0.205
T_{SS} (K)	308.34	309.15	310.56	303.32	304.34	300.86	303.53	306.88
T_{UP} (K)	293.96	294.38	294.68	294.36	294.32	294.30	294.80	295.32
T_∞ (K)	292.85	292.85	292.85	292.85	292.85	292.85	292.85	292.85
T_{IR} (K)	299.93	301.13	301.83	300.37	300.07	296.74	297.24	297.82
h (W/m ² K)	58.98 ± 2.39	49.08 ± 2.5	43.55 ± 2.43	53.54 ± 1.8	54.52 ± 2.14	111.11 ± 6.08	107.16 ± 7.67	78.03 ± 5.06

Table A.7: 113012.05 Plastic

Parameter	0a	0b	0c	1a	1b	2	3	4
x (in)	3.10	4.48	5.85	9.23	10.98	18.23	25.48	32.73
A _t (in ²)	35.06	35.06	35.06	44.63	44.63	44.63	44.63	44.63
ε	0.95	0.95	0.95	0.95	0.95	0.95	0.95	0.95
σ (W/m ² K ⁴)	5.67e-8	5.67e-8	5.67e-8	5.67e-8	5.67e-8	5.67e-8	5.67e-8	5.67e-8
t _p (in)	0.72	0.72	0.72	0.72	0.72	0.72	0.72	0.72
C _k	0.90	0.90	0.90	0.90	0.90	1.05	1.10	1.05
E (V)	6.38	6.38	6.38	5.95	5.95	6.04	6.52	6.01
I (A)	2.07	2.07	2.07	2.57	2.57	2.54	2.71	2.64
k _p (W/mK)	0.205	0.205	0.205	0.205	0.205	0.205	0.205	0.205
T _{SS} (K)	313.57	313.98	313.82	312.38	314.99	312.25	312.87	312.88
T _{UP} (K)	296.41	296.87	297.08	297.21	297.39	297.74	298.09	298.15
T _∞ (K)	294.95	294.95	294.95	294.95	294.95	294.95	294.95	294.95
T _{IR} (K)	301.15	302.43	303.31	304.05	305.08	298.97	299.78	300.32
h (W/m ² K)	60.71 ± 0.92	49.41 ± 2.23	44.01 ± 2.37	35.8 ± 1.45	29.11 ± 1.15	84.66 ± 7.32	83.64 ± 7.69	64.72 ± 4.67

Table A.8: 113012.05 Aluminum

Parameter	0a	0b	0c	1a	1b	2	3	4
x (in)	3.10	4.48	5.85	9.23	10.98	18.23	25.48	32.73
A _t (in ²)	35.06	35.06	35.06	44.63	44.63	44.63	44.63	44.63
ϵ	0.95	0.95	0.95	0.95	0.95	0.95	0.95	0.95
σ (W/m ² K ⁴)	5.67e-8	5.67e-8	5.67e-8	5.67e-8	5.67e-8	5.67e-8	5.67e-8	5.67e-8
t _p (in)	0.72	0.72	0.72	0.72	0.72	0.72	0.72	0.72
C _k	0.90	0.90	0.90	0.90	0.90	1.05	1.10	1.05
E (V)	6.46	6.46	6.46	5.88	5.88	6.01	6.41	6.01
I (A)	2.11	2.11	2.11	2.59	2.59	2.55	2.74	2.64
k _p (W/mK)	0.205	0.205	0.205	0.205	0.205	0.205	0.205	0.205
T _{SS} (K)	310.96	311.18	312.52	304.72	305.90	303.33	307.34	306.56
T _{UP} (K)	295.27	295.62	295.90	295.56	295.59	295.53	296.21	296.20
T _∞ (K)	293.96	293.96	293.96	293.96	293.96	293.96	293.96	293.96
T _{IR} (K)	300.34	301.90	302.81	300.87	300.61	297.51	298.03	298.60
h (W/m ² K)	63.91 ± 1.58	50.38 ± 2.41	43.36 ± 2.37	57.58 ± 2.27	58.31 ± 2.65	118.34 ± 7.57	110.65 ± 9.67	86.94 ± 5.51

Table A.9: 112912.02 Plastic

Parameter	0a	0b	0c	1a	1b	2	3	4
x (in)	3.10	4.48	5.85	9.23	10.98	18.23	25.48	32.73
A _t (in ²)	35.06	35.06	35.06	44.63	44.63	44.63	44.63	44.63
ϵ	0.95	0.95	0.95	0.95	0.95	0.95	0.95	0.95
σ (W/m ² K ⁴)	5.67e-8							
t _p (in)	0.72	0.72	0.72	0.72	0.72	0.72	0.72	0.72
C _k	0.90	0.90	0.90	0.90	0.90	1.05	1.10	1.05
E (V)	6.42	6.42	6.42	5.92	5.92	6.02	6.53	6.01
I (A)	2.07	2.07	2.07	2.57	2.57	2.54	2.72	2.64
k _p (W/mK)	0.205	0.205	0.205	0.205	0.205	0.205	0.205	0.205
T _{SS} (K)	313.67	314.20	314.37	313.64	315.84	312.04	313.51	314.03
T _{UP} (K)	296.35	296.86	297.12	297.30	297.57	297.74	298.16	298.34
T _∞ (K)	294.93	294.93	294.93	294.93	294.93	294.93	294.93	294.93
T _{IR} (K)	301.21	302.46	303.38	304.16	302.16	299.49	299.15	300.34
h (W/m ² K)	59.96 ± 1.22	48.98 ± 2.27	43.09 ± 2.38	33.60 ± 1.43	41.86 ± 2.68	74.04 ± 5.83	95.5 ± 10.13	62.12 ± 4.68

Table A.10: 112912.02 Aluminum

Parameter	0a	0b	0c	1a	1b	2	3	4
x (in)	3.10	4.48	5.85	9.23	10.98	18.23	25.48	32.73
A _t (in ²)	35.06	35.06	35.06	44.63	44.63	44.63	44.63	44.63
ε	0.95	0.95	0.95	0.95	0.95	0.95	0.95	0.95
σ (W/m ² K ⁴)	5.67e-8	5.67e-8	5.67e-8	5.67e-8	5.67e-8	5.67e-8	5.67e-8	5.67e-8
t _p (in)	0.72	0.72	0.72	0.72	0.72	0.72	0.72	0.72
C _k	0.90	0.90	0.90	0.90	0.90	1.05	1.10	1.05
E (V)	7.10	7.10	7.10	6.53	6.53	6.62	7.01	6.01
I (A)	1.79	1.79	1.79	2.58	2.58	2.28	2.20	2.64
k _p (W/mK)	0.205	0.205	0.205	0.205	0.205	0.205	0.205	0.205
T _{SS} (K)	306.37	306.99	307.70	300.31	300.45	298.78	299.94	300.86
T _{UP} (K)	294.94	295.31	295.56	295.14	295.16	295.22	295.56	295.74
T _∞ (K)	293.77	293.77	293.77	293.77	293.77	293.77	293.77	293.77
T _{IR} (K)	300.27	301.84	302.92	299.17	298.57	297.42	298.10	299.03
h (W/m ² K)	62.75 ± 3.39	49.09 ± 3.19	42.10 ± 2.95	93.10 ± 3.02	105.34 ± 4.1	126.66 ± 5.67	105.62 ± 5.92	87.74 ± 3.79

Table A.11: 113012.04 Plastic

Parameter	0a	0b	0c	1a	1b	2	3	4
x (in)	3.10	4.48	5.85	9.23	10.98	18.23	25.48	32.73
A _t (in ²)	35.06	35.06	35.06	44.63	44.63	44.63	44.63	44.63
ϵ	0.95	0.95	0.95	0.95	0.95	0.95	0.95	0.95
σ (W/m ² K ⁴)	5.67e-8							
t _p (in)	0.72	0.72	0.72	0.72	0.72	0.72	0.72	0.72
C _k	0.90	0.90	0.90	0.90	0.90	1.05	1.10	1.05
E (V)	6.46	6.46	6.46	5.91	5.91	6.06	6.57	6.01
I (A)	2.08	2.08	2.08	2.56	2.56	2.53	2.70	2.64
k _p (W/mK)	0.205	0.205	0.205	0.205	0.205	0.205	0.205	0.205
T _{SS} (K)	312.64	313.37	314.25	312.19	314.93	313.87	312.91	312.80
T _{UP} (K)	296.12	296.58	296.85	297.01	297.13	297.68	297.90	298.00
T _∞ (K)	294.33	294.33	294.33	294.33	294.33	294.33	294.33	294.33
T _{IR} (K)	300.99	302.36	303.24	303.58	304.74	298.22	298.62	298.49
h (W/m ² K)	58.56 ± 1.90	47.18 ± 2.39	41.24 ± 2.38	34.66 ± 1.38	27.58 ± 1.06	82.44 ± 8.03	95.08 ± 9.78	85.10 ± 7.35

Table A.12: 113012.04 Aluminum

Parameter	0a	0b	0c	1a	1b	2	3	4
x (in)	3.10	4.48	5.85	9.23	10.98	18.23	25.48	32.73
A _t (in ²)	35.06	35.06	35.06	44.63	44.63	44.63	44.63	44.63
ϵ	0.95	0.95	0.95	0.95	0.95	0.95	0.95	0.95
σ (W/m ² K ⁴)	5.67e-8	5.67e-8	5.67e-8	5.67e-8	5.67e-8	5.67e-8	5.67e-8	5.67e-8
t _p (in)	0.72	0.72	0.72	0.72	0.72	0.72	0.72	0.72
C _k	0.90	0.90	0.90	0.90	0.90	1.05	1.10	1.05
E (V)	6.51	6.51	6.51	5.97	5.97	6.03	6.46	6.01
I (A)	2.10	2.10	2.10	2.56	2.56	2.54	2.74	2.64
k _p (W/mK)	0.205	0.205	0.205	0.205	0.205	0.205	0.205	0.205
T _{SS} (K)	311.52	311.50	312.09	305.21	306.94	303.96	304.70	304.35
T _{UP} (K)	295.40	295.83	296.08	295.71	295.73	295.74	296.02	296.03
T _∞ (K)	294.30	294.30	294.30	294.30	294.30	294.30	294.30	294.30
T _{IR} (K)	300.47	302.05	303.05	301.61	301.49	297.63	297.58	297.89
h (W/m ² K)	66.04 ± 1.10	52.00 ± 2.41	44.98 ± 2.43	53.76 ± 2.00	52.41 ± 2.29	125.38 ± 8.70	149.52 ± 13.53	120.89 ± 8.09

Table A.13: 112912.06 Plastic

Parameter	0a	0b	0c	1a	1b	2	3	4
x (in)	3.10	4.48	5.85	9.23	10.98	18.23	25.48	32.73
A _t (in ²)	35.06	35.06	35.06	44.63	44.63	44.63	44.63	44.63
ε	0.95	0.95	0.95	0.95	0.95	0.95	0.95	0.95
σ (W/m ² K ⁴)	5.67e-8	5.67e-8	5.67e-8	5.67e-8	5.67e-8	5.67e-8	5.67e-8	5.67e-8
t _p (in)	0.72	0.72	0.72	0.72	0.72	0.72	0.72	0.72
C _k	0.90	0.90	0.90	0.90	0.90	1.05	1.10	1.05
E (V)	6.53	6.53	6.53	6.00	6.00	6.06	6.65	6.01
I (A)	2.07	2.07	2.07	2.54	2.54	2.53	2.67	2.64
k _p (W/mK)	0.205	0.205	0.205	0.205	0.205	0.205	0.205	0.205
T _{SS} (K)	312.81	313.29	313.92	313.16	315.55	313.51	312.63	314.29
T _{UP} (K)	296.20	296.67	296.97	297.23	297.21	297.76	298.00	298.25
T _∞ (K)	295.17	295.17	295.17	295.17	295.17	295.17	295.17	295.17
T _{IR} (K)	301.12	302.34	303.21	303.73	301.25	298.06	299.81	298.85
h (W/m ² K)	66.76 ± 0.13	54.41 ± 2.27	47.45 ± 2.43	37.30 ± 1.69	50.93 ± 3.99	113.90 ± 14.11	88.07 ± 8.36	92.8 ± 9.36

Table A.14: 112912.06 Aluminum

Parameter	0a	0b	0c	1a	1b	2	3	4
x (in)	3.10	4.48	5.85	9.23	10.98	18.23	25.48	32.73
A _t (in ²)	35.06	35.06	35.06	44.63	44.63	44.63	44.63	44.63
ε	0.95	0.95	0.95	0.95	0.95	0.95	0.95	0.95
σ (W/m ² K ⁴)	5.67e-8	5.67e-8	5.67e-8	5.67e-8	5.67e-8	5.67e-8	5.67e-8	5.67e-8
t _p (in)	0.72	0.72	0.72	0.72	0.72	0.72	0.72	0.72
C _k	0.90	0.90	0.90	0.90	0.90	1.05	1.10	1.05
E (V)	6.49	6.49	6.49	5.88	5.88	6.00	6.46	6.01
I (A)	2.10	2.10	2.10	2.57	2.57	2.56	2.75	2.64
k _p (W/mK)	0.205	0.205	0.205	0.205	0.205	0.205	0.205	0.205
T _{SS} (K)	311.23	311.55	312.36	303.50	304.15	302.89	305.15	304.44
T _{UP} (K)	294.99	295.54	295.85	295.41	295.24	295.40	295.92	295.99
T _∞ (K)	294.09	294.09	294.09	294.09	294.09	294.09	294.09	294.09
T _{IR} (K)	300.35	301.95	303.02	298.95	298.37	297.22	297.75	298.27
h (W/m ² K)	64.18 ± 1.32	50.21 ± 2.40	42.93 ± 2.40	85.61 ± 4.79	96.04 ± 6.61	136.55 ± 9.43	132.05 ± 11.22	102.51 ± 6.23

Table A.15: Ellipsoids Plastic

Parameter	0a	0b	0c	1a	1b	2	3	4
x (in)	3.10	4.48	5.85	9.23	10.98	18.23	25.48	32.73
A _t (in ²)	35.06	35.06	35.06	44.63	44.63	44.63	44.63	44.63
ϵ	0.95	0.95	0.95	0.95	0.95	0.95	0.95	0.95
σ (W/m ² K ⁴)	5.67e-8	5.67e-8	5.67e-8	5.67e-8	5.67e-8	5.67e-8	5.67e-8	5.67e-8
t _p (in)	0.72	0.72	0.72	0.72	0.72	0.72	0.72	0.72
C _k	0.90	0.90	0.90	0.90	0.90	1.05	1.10	1.05
E (V)	6.53	6.53	6.53	6.03	6.03	6.07	6.53	6.01
I (A)	2.10	2.10	2.10	2.55	2.55	2.51	2.67	2.64
k _p (W/mK)	0.205	0.205	0.205	0.205	0.205	0.205	0.205	0.205
T _{SS} (K)	310.77	310.68	311.78	309.35	312.56	310.78	309.58	309.22
T _{UP} (K)	294.74	295.10	295.39	295.51	295.67	295.94	296.20	296.30
T _∞ (K)	293.67	293.67	293.67	293.67	293.67	293.67	293.67	293.67
T _{IR} (K)	300.23	301.44	302.45	302.19	303.72	296.72	297.42	297.64
h (W/m ² K)	62.07 ± 1.86	52.08 ± 2.45	44.51 ± 2.43	40.49 ± 1.65	30.33 ± 1.15	110.98 ± 12.45	111.75 ± 12.11	95.21 ± 7.75

Table A.16: Ellipsoids Aluminum

Parameter	0a	0b	0c	1a	1b	2	3	4
x (in)	3.10	4.48	5.85	9.23	10.98	18.23	25.48	32.73
A_t (in ²)	35.06	35.06	35.06	44.63	44.63	44.63	44.63	44.63
ϵ	0.95	0.95	0.95	0.95	0.95	0.95	0.95	0.95
σ (W/m ² K ⁴)	5.67e-8	5.67e-8	5.67e-8	5.67e-8	5.67e-8	5.67e-8	5.67e-8	5.67e-8
t_p (in)	0.72	0.72	0.72	0.72	0.72	0.72	0.72	0.72
C_k	0.90	0.90	0.90	0.90	0.90	1.05	1.10	1.05
E (V)	6.45	6.45	6.45	5.89	5.89	6.05	6.46	6.01
I (A)	2.10	2.10	2.10	2.58	2.58	2.55	2.74	2.64
k_p (W/mK)	0.205	0.205	0.205	0.205	0.205	0.205	0.205	0.205
T_{SS} (K)	312.66	312.94	313.51	309.09	310.33	304.80	305.52	308.49
T_{UP} (K)	296.50	296.93	297.16	297.10	297.10	296.92	297.12	297.55
T_∞ (K)	295.52	295.52	295.52	295.52	295.52	295.52	295.52	295.52
T_{IR} (K)	301.58	303.03	304.01	302.76	302.57	298.70	298.99	299.23
h (W/m ² K)	66.17 ± 0.58	52.41 ± 2.32	45.27 ± 2.39	50.44 ± 2.33	50.16 ± 2.59	133.84 ± 9.36	141.37 ± 11.95	108.19 ± 8.26

Table A.17: Elliptical Cones Plastic

Parameter	0a	0b	0c	1a	1b	2	3	4
x (in)	3.10	4.48	5.85	9.23	10.98	18.23	25.48	32.73
A _t (in ²)	35.06	35.06	35.06	44.63	44.63	44.63	44.63	44.63
ε	0.95	0.95	0.95	0.95	0.95	0.95	0.95	0.95
σ (W/m ² K ⁴)	5.67e-8	5.67e-8	5.67e-8	5.67e-8	5.67e-8	5.67e-8	5.67e-8	5.67e-8
t _p (in)	0.72	0.72	0.72	0.72	0.72	0.72	0.72	0.72
C _k	0.90	0.90	0.90	0.90	0.90	1.05	1.10	1.05
E (V)	6.53	6.53	6.53	6.02	6.02	6.13	6.55	6.01
I (A)	2.08	2.08	2.08	2.53	2.53	2.57	2.68	2.64
k _p (W/mK)	0.205	0.205	0.205	0.205	0.205	0.205	0.205	0.205
T _{SS} (K)	312.70	312.47	313.30	311.43	314.79	310.70	312.50	311.96
T _{UP} (K)	296.69	297.05	297.26	296.07	297.68	297.92	298.39	298.30
T _∞ (K)	295.76	295.76	295.76	295.76	295.76	295.76	295.76	295.76
T _{IR} (K)	302.07	303.30	304.31	303.91	305.22	299.24	299.49	300.04
h (W/m ² K)	63.63 ± 1.62	53.10 ± 2.45	45.34 ± 2.47	40.05 ± 1.92	31.76 ± 1.36	104.47 ± 9.28	110.65 ± 12.40	85.6 ± 6.83

Table A.18: Elliptical Cones Aluminum

Parameter	0a	0b	0c	1a	1b	2	3	4
x (in)	3.10	4.48	5.85	9.23	10.98	18.23	25.48	32.73
A_t (in ²)	35.06	35.06	35.06	44.63	44.63	44.63	44.63	44.63
ϵ	0.95	0.95	0.95	0.95	0.95	0.95	0.95	0.95
σ (W/m ² K ⁴)	5.67E-08	5.67E-08	5.67E-08	5.67E-08	5.67E-08	5.67E-08	5.67E-08	5.67E-08
t_p (in)	0.72	0.72	0.72	0.72	0.72	0.72	0.72	0.72
C_k	0.90	0.90	0.90	0.90	0.90	1.05	1.10	1.05
E (V)	6.52	6.52	6.52	5.88	5.88	6.02	6.46	6.01
I (A)	2.08	2.08	2.08	2.57	2.57	2.53	2.73	2.64
k_p (W/mK)	0.205	0.205	0.205	0.205	0.205	0.205	0.205	0.205
T_{SS} (K)	312.17	312.01	311.94	305.61	307.25	306.06	306.13	305.86
T_{UP} (K)	295.34	295.70	295.85	295.45	295.65	295.91	296.11	296.14
T_∞ (K)	293.91	293.91	293.91	293.91	293.91	293.91	293.91	293.91
T_{IR} (K)	300.33	301.76	302.62	301.71	301.54	297.27	297.76	298.10
h (W/m ² K)	61.41 ± 1.55	49.84 ± 2.41	44.52 ± 2.45	48.31 ± 1.75	47.59 ± 1.99	116.09 ± 9.09	121.26 ± 10.41	98.81 ± 6.45

REFERENCES

- [1] Addy, H. E., 2000, "Ice Accretions and Icing Effects for Modern Airfoil," NASA/TP-2000-210031.
- [2] "14 CFR Part 25: Airworthiness Standards: Transport Category Airplanes – Appendix C, Part I: Atmospheric Icing Conditions," 2012, Code of Federal Regulations
- [3] "14 CFR Part 25: Airworthiness Standards: Transport Category Airplanes – Appendix O, Part I: Metrology," 2014, Code of Federal Regulations
- [4] Wright, W. B., and Bidwell, C. S., 2014, "How Roughness Research can Improve LEWICE," Invited Oral Presentation, 6th AIAA Atmospheric and Space Environments Conference, 16-20 June, Atlanta, GA.
- [5] Wright W.B., Rutkowski, A., 1999, "Validation Results for LEWICE 2.0," NASA, NASA/CR-1999-208690, Cleveland, OH.
- [6] Tecson, L., 2013, "Convective Heat Transfer from Realistic Ice Roughness Distributions," MS thesis, Department of Mechanical Engineering, Baylor University.
- [7] Walker, C.W., 2014, "Convection from Manufactured Ice Roughness with Varying Flux Boundary Conditions," MS thesis, Department of Mechanical Engineering, Baylor University.
- [8] Shannon, T.A., 2015, "Convection from Realistic Ice Roughness on a Simulated NACA 0012 Airfoil," MS thesis, Department of Mechanical Engineering, Baylor University.
- [9] Hughes, M.T., 2015, "Convective Enhancement on airfoil Due to Ice Roughness Elements in Stagnation Region Flows," MS thesis, Department of Mechanical Engineering, Baylor University.
- [10] Hawkins, D.M., 2016, "Convection from Laser-Scanned Real Ice Roughness on a Simulated NACA 0012 Airfoil," MS thesis, Department of Mechanical Engineering, Baylor University.
- [11] McCarrell, J., 2017, "Convection from Laser-Scanned Ice Roughness at Multiple Accretion Event Times," MS thesis, Department of Mechanical Engineering, Baylor University.

- [12] Clemenson, J.M., 2018, "A Method for Replicating Ice Accretion Roughness Using Multi-Scale Analog Distributions," MS thesis, Department of Mechanical Engineering, Baylor University.
- [13] Munson, B.R., Okiishi, T.H., Huebsch, W.W., and Rothmayer, A.P., 2013, *Fundamentals of Fluid Mechanics*, 7th ed., John Wiley & Sons, Inc., Hoboken, NJ, pp. 482.
- [14] Moran, M. J., and Shapiro, H. N., 2008, *Fundamentals of Engineering Thermodynamics*, 6th ed., John Wiley & Sons, Inc., Hoboken, NJ.
- [15] Incropera, F. P., Dewitt, D. P., Bergman, T. L., and Lavine, A. S., (2007), *Fundamentals of Heat and Mass Transfer*, Hoboken, NJ: John Wiley & Sons, Inc., 6th edition.
- [16] Smith, A.G., and Spaulding, D.B., 1958, "Heat Transfer in a Laminar Boundary Layer with Constant Fluid Properties and Constant Wall Temperature," *J. Roy. Aero. Soc.*, Vol. 62, pg 60-64.
- [17] Ambrok, G.S., 1957, "Approximate Solutions of the Equations for the Thermal Boundary Layer with Variations in the Boundary Layer Structure," *Soviet Phys.-Tech. Phys.*, Vol. 2, No. 9, pg 1979-1986.
- [18] Nikuradse, J., 1933, "Laws for Flows in Rough Pipes," *VDI-Forschungsheft*, **4**, pp. 361.
- [19] Schlichting, H., 1936, "Experimental Investigation of the Problem of Surface Roughness," TM-832, National Advisory Committee on Aeronautics.
- [20] Hama, F. R., 1954, "Boundary Layer Characteristics for Smooth and Rough Surfaces," *Naval Architects Marine Engineers*, Trans 62.
- [21] Clauser, F., 1956, "The Turbulent Boundary Layer," *Advances in Applied Mechanics*, Vol 4.
- [22] Rotta, J., 1950, "Über die Theorie der turbulenten Grenzschichten," *Mitteilungen MPI Stromungs Forschung*, Vol. 1.
- [23] Dvorak, F. A., 1969, "Calculation of Turbulent Boundary Layers on Rough Surfaces in Pressure Gradients," *AIAA Journal*, Vol. 7, pp. 1752-1759.
- [24] Betterman, D., 1969, "Contribution a l'Etude de la Convection Force Turbulente le Long de Plaques Plaques Rugueuses," *AIAA Journal*, Vol. 9, pp. 153 – 164
- [25] Simpson R. L., 1973, "A Generalized Correlation of Roughness Density Effects on the Turbulent Boundary Layer," *AIAA Journal*, Vol. 11, pp. 242-244

- [26] Dirling, R. B., 1973, "A Method for Computing Rough Wall Heat Transfer Rates on Reentry Nose Tips," AIAA Paper No. 73-763.
- [27] Coleman, H. W., Moffat, R. J., and Kays, W. M., 1981, "Heat Transfer in the Accelerated Fully Rough Turbulent Boundary Layer," *Journal of Heat Transfer*, Vol. 103, No. 1, pp. 153-158.
- [28] Sigal, A. and Danberg, J. E., (1990), "New Correlation of Roughness Density Effect on the Turbulent Boundary Layer," *AIAA Journal*, Vol. 28, No. 3, pp. 554-556.
- [29] McClain, S.T., Reed, D., Vargas, M., Kreeger, R.E., and Tsao, J.C., 2014, "Ice Roughness in Short Duration SLD Icing Events," 6th AIAA Atmospheric and Space Environments Conference, 16-20 June, Atlanta, GA, AIAA-2014-2330.
- [30] McClain, S.T., Vargas, M., Kreeger, R.E., and Tsao, J., 2015, "A Reevaluation of Appendix C Ice Roughness Using Laser Scanning," SAE Technical Paper 2015-01-2098, 2015, doi:10.4271/2015-01-2097.
- [31] McClain, S.T., and Kreeger, R.E., 2013, "Assessment of Ice Shape Roughness Using a Self-Organizing Map Approach," 5th AIAA Atmospheric and Space Environments Conference, 24-27 June, San Diego, CA, AIAA-2013-2546
- [32] Bons, J. P., McClain, S. T., Wang, Z. J., Chi, X., Shih, T. I., 2005, "A Comparison of approximate vs. Exact Geometrical Representations of Roughness for CFD Calculations of c_f and St ," ASME International Mechanical Engineering Congress and Exposition.
- [33] "Compliance of Transport Category Airplanes with Certification Requirements for Flight in Icing Conditions," 2014, AC No: 25-28.
- [34] "14 CFR Part 25: Airworthiness Standards: Transport Category Airplanes - Appendix O, Part I: Meteorology," 2014, *Code of Federal Regulations*.
- [35] Bragg, M.B., Hutchison, T., Merret, J., Oltman, R., Pokhariyal, D., 2000, "Effects of Ice Accretion on Aircraft Flight Dynamics," 38th AIAA Aerospace Sciences Meeting and Exhibit, 10-13 January, Reno, NV, AIAA-2000-0360.
- [36] Anderson, D.N., Hentschel, D.B., and Ruff, G.A., 1998, "Measurement and Correlation of Ice Accretion Roughness," NASA-CR-2003-211823.
- [37] Ruff, G.A., 1986, "Analysis and Verification of the Icing Scaling Equations," AEDC-TR-85-30.
- [38] Tsao, J.C., and Lee, S., 2012, "Evaluation of Icing Scaling on Swept NACA 0012 Airfoil Models." NASA CR-2012-217419.

- [39] Langmuir and Blodgett (1946) A Mathematical Investigation of Water Droplet Trajectories
- [40] McClain, S.T., Vargas, M., and Tsao, J.C., 2017, "Ice Roughness and Thickness Evolution on a Swept NACA 0012 Airfoil," 9th AIAA Atmospheric and Space Environments Conference, 5-9 June, Denver, CO, AIAA-2017-3585.
- [41] Olsen, W., Walker, E., 1986, "Experimental Evidence for Modifying the Current Physical Model for Ice Accretion on Aircraft Surfaces," NASA TM-87184.
- [42] Messinger, B.L., 1953, "Equilibrium Temperature of an Unheated Icing Surface as a Function of Air Speed," *Journal of Aeronautical Sciences*, pp. 29-42.
- [43] J. P. Bons and S. T. McClain, "The Effect of Real Turbine Roughness with Pressure Gradient on Heat Transfer," *Journal of Turbomachinery*, Vol. 126, No. 3, pg 385-394, 2004.
- [44] Bons, J. P., 2002, "St and Cf Augmentation for Real Turbine Roughness With Elevated Freestream Turbulence," *Journal of Turbomachinery*, 124, pp. 632-644.
- [45] Shin, J., 1994, "Characteristics of Surface Roughness Associated With Leading Edge Ice Accretion," NASA TM-106459.
- [46] Poinsette, P.E., Van Fossen, G.J., and DeWitt, K.J., 1990, "Convective Heat Transfer Measurements from a NACA 0012 Airfoil in Flight and in the NASA Lewis Icing Research Tunnel," NASA TM-102448.
- [47] Bragg, M. B., Cummings, M. J., Lee, S., Henze, C. M., 1996, "Boundary-Layer and Heat-Transfer Measurements on an Airfoil with Simulated Ice Roughness," AIAA Paper 96-0866.
- [48] Dukhan, N., Van Fossen, G. J., DeWitt, K. J., Masiulaniec, K. C., 2003, "Experimental Frossling Numbers for Ice-Roughened NACA 0012 Airfoils," *Journal of Aircraft* **40**(6), pp. 1161-1167.
- [49] Han, Y., and Palacios, J., 2014, "Transient Heat Transfer Measurements of Surface Roughness due to Ice Accretion," 6th AIAA Atmospheric and Space Environments Conference, 16-20 June, Atlanta, GA, AIAA-2014-2464.
- [50] Tecson, L. and McClain, S.T., (2013), "Convective Enhancement of Surfaces with Realistic Ice Roughness Distributions," 5th AIAA Atmospheric and Space Environments Conference, 24-27 June, San Diego, CA, AIAA-2013-3060.

- [51] Tecson, L. and McClain, S.T., (2013), "Modeling of Realistic Ice Roughness Element Distributions to Characterize Convective Heat Transfer," 5th AIAA Atmospheric and Space Environments Conference, 24-27 June, San Diego, CA, AIAA-2013-3059.
- [52] Walker, C.W., McClain, S.T., and Shannon, T.A., 2014, "Convection from Ice Roughness with Varying Flux Boundary Conditions," 6th AIAA Atmospheric and Space Environments Conference, 16-20 June, Atlanta, GA, AIAA-2014-2463.
- [53] Shannon, T. A., and McClain, S. T., 2016, "Convection from a Simulated NACA 0012 with Icing Roughness of Different Shape and Thermal Conductivity," 8th AIAA Atmospheric and Space Environments Conference, 13-17 June, Washington, DC, AIAA-2016-3588.
- [54] McClain, S. T., Tiño, P., and Kreeger, R. E., 2011, "Ice Shape Characterization Using Self-Organizing Maps," *Journal of Aircraft*, 48(2), pp. 724-729.
- [55] McClain, S.T., Vargas, M., and Tsao, J.C., 2016, "Characterization of Ice Roughness Variations in Scaled Glaze Icing Conditions," 8th AIAA Atmospheric and Space Environments Conference, 13-17 June, Washington, D.C., AIAA-2016-3592.
- [56] The International Association for the Properties of Water and Steam, 2007, "Revised Release on the IAPWS Industrial Formulation 1997 for the Thermodynamic Properties of Water and Steam," <http://www.iapws.org/>.
- [57] White, F. M., 2006, *Viscous Fluid Flow*, 3rd Ed, Boston, McGraw-Hill, Inc., New York, NY.
- [58] Wilke, C. R., 1950, "A Viscosity Equation for Gas Mixtures," *Journal of Chemical Physics*, 18(4), pp. 517-519.
- [59] Coleman, H. W., and Steele, W. G., 1999, *Experimentation and Uncertainty Analysis for Engineers*, 2nd ed., John Wiley and Sons, Inc., Hoboken, NJ.
- [60] Kline, S. J., and McClintock, F. A., 1953, "Describing Uncertainties in Single-Sample Experiments," *Mechanical Engineering*, 75, pp. 3-8.